6-29-2018

Broadband Measurement and Reduction of Quantum Radiation Pressure Noise in the Audio Band

Jonathan Daniel Cripe
Louisiana State University and Agricultural and Mechanical College

BROADBAND MEASUREMENT AND REDUCTION OF QUANTUM RADIATION PRESSURE NOISE IN THE AUDIO BAND

A Dissertation

Submitted to the Graduate Faculty of the
Louisiana State University and
Agricultural and Mechanical College
in partial fulfillment of the
requirements for the degree of
Doctor of Philosophy in Physics

in

Department of Physics and Astronomy

by
Jonathan Cripe
B.A., DePauw University, 2012
August 2018

Acknowledgments

First I would like to thank my advisor Thomas Corbitt for being a wonderful advisor. Thank you for sharing your knowledge of optomechanics and everything that goes in to designing and running an experiment with me. Thank you for patiently answering all of my questions and being a great mentor.

I would also like to thank the graduate students, postdocs, and LIGO scientists that I have worked with at LSU and LIGO, including Robi Singh, Marissa Walker, Thomas Abbott, Terra Hardwick, Corey Austin, Christopher Buchanan, Duncan Macleod, Marie Kasprzack, Arnaud Pele, Guillermo Valdes, Carl Blair, Shivaraj Kandhasamy, Adam Mullavey, Keiko Kokeyama, Matt Heintze, and Anamaria Effler. Thank you for sharing your knowledge of gravitational waves and LIGO with me. Thank you to everyone that proofread sections of my thesis and provided valuable comments and feedback. Just as importantly, thank you for being a wonderful group of friends that I could always count on. Thank you for all of the dinners together, parties at the pool house, and weekend adventures. I could not have asked for a better group of friends during my time in Baton Rouge. Thank you to all of my non-LIGO friends in Baton Rouge for making Louisiana a place to call home.

I would like to thank our collaborators at the Australian National University for their role in building the bright squeezed light source in our lab and their help with integrating it with our experiments. I would especially like to thank Min Jet Yap for coming to LSU to build the squeezer and for teaching me along the way. Thank you for all of the discussions we had together and for being such a fun person to work with and know. I would like to thank Garrett Cole and the staff of Crystalline Mirror Solutions for their help in the design and fabrication of the cantilever mirrors that are at the heart of all the experiments described in this thesis. Thank you for your guidance and advice during the design process and I would also like to thank the talented machinists of the LSU physics department machine shop, Vincent Vaughn, Brandon Amos, and Donnie Olano, for helping me to design and machine parts of my experiment. Much of this experiment would have been

impossible without the parts that you made.

Finally I would like to thank my family for their continual support, inspiration, and guidance. Thank you to my parents and sister for you constant love. A special thank you to my dad for proofreading this dissertation. Thank you to my grandparents for always supporting my education and encouraging me to never stop learning. Thank you Grandpa Sam for your final blessing and encouragement to “find a wave”.

Table of Contents

List of Tables

List of Figures

Abstract

One hundred years after Albert Einstein predicted the existence of gravitational waves in his general theory of relativity, the Laser Interferometer Gravitational-Wave Observatory (LIGO) made the first direct detection of gravitational waves. Since the first detection of gravitational waves from a binary black hole merger, LIGO has gone on to detect gravitational waves from multiple binary black hole mergers, and more recently from a binary neutron star merger in collaboration with telescopes around the world. The detection of gravitational waves has opened a new window to the universe and has launched the era of gravitational wave astronomy.

With the first detection of gravitational waves now two years behind us, work has already begun on improving the sensitivity of Advanced LIGO and planning for future generations of gravitational wave interferometers. One of the main limiting noise sources for current and future gravitational wave detectors is quantum noise, which includes quantum radiation pressure noise that originates from the quantum nature of the photons that reflect off of the test masses.

Chapter one provides an introduction to gravitational wave sources and detectors. It also describes the noise sources that limit the sensitivity of interferometeric gravitational wave detectors like Advanced LIGO and includes a detailed description of the origin of quantum noise and its effect in interferometers.

Chapter two introduces the concept and properties of optical springs. Much of the experimental work presented in the rest of this thesis utilizes an optical spring.

This thesis investigates quantum radiation pressure noise and techniques to reduce quantum noise in gravitational wave interferometers. The experimental research contained in this thesis uses an optomechanical Fabry-Pérot cavity in which one of the cavity mirrors is a microresonator consisting of a micro-mirror suspended by a cantilever structure. Chapter three outlines the design and construction of the optomechanical cavity that is housed in a vacuum chamber and sits on a suspended optical breadboard to provide isolation from

seismic motion. Chapter three also includes details on the design of the cantilever micromirror used in the optomechanical cavity. The experiments in this thesis can be divided into two main categories: the characterization of optical springs and the measurement of broadband quantum radiation pressure noise.

Chapter four of this thesis focuses on the characterization of optical springs. I present results from an experiment that uses radiation pressure to control an optomechanical cavity and investigates the feedback control needed to keep the system stable. In chapter five, I present results from an experiment in which we create an optical spring using a beamsplitter rather than the canonical example of an optical spring in a detuned Fabry-Pérot cavity.

Chapter six of the thesis describes the experiment and results of a broadband measurement of quantum radiation pressure noise. I present a measurement of a noise spectrum in which the effects of quantum radiation pressure noise are observed between 2 kHz and 90 kHz, including a frequency band between 10 kHz and 30 kHz where the quantum radiation pressure noise is visible above all other noise sources.

Chapter seven presents the results from two experiments in which we have successfully reduced the amount of quantum radiation pressure noise. The first experiment is done by detecting the light that is transmitted through the cavity by a photodetector. By detecting the light in transmission of the cavity rather than reflection, we are able to evade the presence of quantum radiation pressure noise in the measurement. The second experiment injects bright squeezed light into the optomechanical cavity in place of the coherent field used in the experiment in chapter six. The injection of squeezed light into the optomechanical cavity successfully reduces the amount of quantum radiation pressure noise.

Finally, having made a measurement of quantum radiation pressure noise and two measurements in which the quantum radiation pressure noise is reduced, I outline a future experiment to measure the ponderomotive squeezing that is produced by the optomechanical cavity and the plans for making a measurement below the Standard Quantum Limit.

Chapter 1
Gravitational Waves and Gravitational Wave Detectors

Just over 100 years ago, Albert Einstein published his General Theory of Relativity, which describes the interaction between matter, energy, space, and time and explains that the force of gravity is a result of the curvature of space and time [1]. Before Einstein's revolutionary paper, our understanding of the cosmos was based on Newton's law of gravity, which describes gravity as a force that acts instantaneously from a distance. Combined with his theory of special relativity, Einstein's General Theory of Relativity completely redefined how we understand the universe. In order to test his hypothesis against the status quo of Newton's gravity, Einstein made several predictions that would differentiate the two theories. Einstein's theory correctly predicted the perihelion precession of Mercury's orbit while Newton's theory was unable to do so. Einstein also predicted the bending of light around massive objects such as stars. His hypothesis was famously proven to be accurate in 1919 when Arthur Eddington and his collaborators observed shift in position of stars by the sun's gravitational field during the total solar eclipse on May 29, 1919 [2].

A year after publishing his General Theory of Relativity, Einstein added another prediction to his theory. In 1916, he published a paper predicting the existence of gravitational waves [3]. The theory of electromagnetism allows for the production of electromagnetic waves when a charge is accelerated. Likewise, Einstein's theory predicted the gravitational analog to electromagnetic waves, which are called gravitational waves. Gravitational waves are produced when a mass (instead of a charge in the electromagnetic case) is accelerated. The accelerating mass produces a change in the curvature of spacetime that travels outward at the speed of light. As the waves travel outward, they change the curvature of spacetime in the directions transverse to their propagation such that the space which they travel through is stretched and squeezed as they pass.

While Einstein's predictions of the perihelion precession of Mercury's orbit and the bending of light around the sun were quickly confirmed, his prediction of the existence of

gravitational waves took much longer to validate. The effects of gravitational waves were first indirectly detected in 1982 through the observation of the Hulse-Taylor pulsar [4]. Hulse and Taylor observed the orbital period of the binary pulsar PSR B1913+16 to decay over time. Their observations of the orbital decay through the emission of gravitational radiation was found to be in excellent agreement with Einstein's prediction 60 years earlier. The total power of the gravitational radiation emitted by the system is currently 7.35×10^{24} Watts, which is about 2% of the power radiated in electromagnetic waves by the sun.

Despite the large amount of power radiated by gravitational waves, they were not directly observed until 100 years after Einstein first published his General Theory of Relativity. Finally, on September 14, 2015 the Laser Interferometer Gravitational-Wave Observatory detected the gravitational wave signal from the merger of two black holes [5].

1.1 Gravitational waves

In his Special Theory of Relativity, Albert Einstein united the three spatial dimensions and one time dimension into the four-dimensional geometry of spacetime. The distance between two points in spacetime is defined as the spacetime interval [6]

$$ds^2 = -c^2dt^2 + dx^2 + dy^2 + dz^2 \quad = \quad -\eta_{\mu\nu}dx^\mu dy^\nu, \tag{1.1}$$

where x, y, and z are the three spatial dimensions, t is the time dimension, and c is the speed of light, which converts units of time into distance. $\eta_{\mu\nu}$ is the Minkowski metric for flat spacetime given by

$$\eta_{\mu\nu} = \begin{pmatrix} -1 & 0 & 0 & 0 \\ 0 & 1 & 0 & 0 \\ 0 & 0 & 1 & 0 \\ 0 & 0 & 0 & 1 \end{pmatrix}. \tag{1.2}$$

In this notation, the Greek subscripts run from 0 to 3 and represent t, x, y, and z.

In general relativity, mass and energy cause spacetime to curve. As a result, the Minkowski metric for flat spacetime in Equation 1.1 is replaced by the more general spacetime metric $g_{\mu\nu}$. The relationship between matter and spacetime is given by the Einstein field equations:

$$R_{\mu\nu} - \frac{1}{2}Rg_{\mu\nu} = \frac{8\pi G}{c^4}T_{\mu\nu}. \tag{1.3}$$

The left-hand side of the equation describes the geometrical nature of spacetime through the Ricci tensor, $R_{\mu\nu}$, the Ricci scalar, R, and $g_{\mu\nu}$. The right-hand side of the equation describes the mass and energy of the system with the stress-energy tensor $T_{\mu\nu}$. This set of ten nonlinear equations is very complex. As a result, we will introduce some approximations and assumptions to simplify the derivation of gravitational waves. Since we are interested in studying gravitational waves in the weak-field, away from any large mass, we can approximate $g_{\mu\nu}$ as the flat spacetime metric $\eta_{\mu\nu}$ plus a small perturbation $h_{\mu\nu}$. Doing so yields

$$g_{\mu\nu} = \eta_{\mu\nu} + h_{\mu\nu}. \tag{1.4}$$

The stress-energy tensor also goes to zero in the weak-field limit. By using the transverse traceless gauge, we can further simplify Equation 1.3 to:

$$\left(\nabla^2 - \frac{1}{c^2}\frac{\partial^2}{\partial t^2}\right) h_{\mu\nu} = 0. \tag{1.5}$$

Equation 1.5 has the form of a wave equation. For a wave traveling in the z-direction, the solutions of the wave equation are

$$h = Ae^{2\pi f t - \boldsymbol{k}\cdot\boldsymbol{x}}, \tag{1.6}$$

where A is the amplitude of the wave, f is the frequency, and $\boldsymbol{k}$ is the wave number. Since we have used the transverse traceless gauge, then

$$h_{\mu\nu} = \begin{pmatrix} 0 & 0 & 0 & 0 \\ 0 & h_+ & h_x & 0 \\ 0 & h_x & -h_+ & 0 \\ 0 & 0 & 0 & 0 \end{pmatrix}. \tag{1.7}$$

As seen in Equations 1.6 and 1.7, the wave is transverse (the strain is only in the x and y directions and zero in the z direction) and the tensor is traceless ($h_+ + -h_+ = 0$). h_+ and h_x represent two orthogonal polarizations for the wave traveling in the z-direction and are called "h plus" and "h cross", respectively. The axes of h_x are rotated 45° with respect to the axes of h_+. The opposite signs of h_{11} and h_{22} describe the effect of the strain lengthening one dimension (x) while contracting the other dimension (y). After half a period of the wave, the x-direction is shortened while the y-direction is lengthened. The effect of a passing gravitational wave on a set of test masses arranged in a circle is shown in Figure 1.1. The strength of the gravitational wave is the proportional change in length between the free test masses, namely

$$h = \frac{\Delta L}{L}. \tag{1.8}$$

1.2 Gravitational wave sources

Now that we understand the propagation of gravitational waves through spacetime and their effect on matter, we can ask the question of how the gravitational are waves produced. To comprehend the production of gravitational waves, it is helpful to recall the production of radiation in electrodynamics, where the multipole expansion is used to calculate radiation in the limit that the size of the source is smaller than the wavelength of radiation. In electrodynamics, the leading order terms for the production of radiation

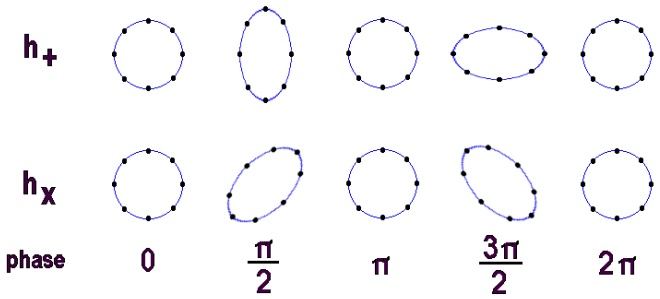

Figure 1.1: An illustration of the effect of the two gravitational wave polarizations on a set of test masses arranged in a circle. As the h_+ wave passes in a direction perpendicular to the page, the distance between the test masses in the vertical and horizontal directions is increased and decreased. The h_x polarization is similar but rotated by 45 degrees [7]

are the electric dipole moment, magnetic dipole moment, and electric quadrupole moment. There is no radiation from the electromagnetic monopole because of the conservation of electric charge.

The production of radiation in the gravitational analog has a few key differences from its electromagnetic counterpart. One important difference is that while electromagnetism has two charges (positive and negative), the gravitational analog of charge (mass) only has one sign. Like the conservation of charge in electrodynamics, the conservation of energy prohibits gravitational monopole radiation. Gravitational dipole radiation is prohibited by the conservation of momentum and angular momentum. The next possible term for gravitational radiation is the quadrupole moment, $\ddot{I}_{\mu\nu}$. The radiation produced by a time varying gravitational quadrupole moment is [6]:

$$h = \frac{2G}{Rc^4}\ddot{I}_{\mu\nu}, \tag{1.9}$$

where R is the distance from the source to the observer. Evaluating Equation 1.9 for a wave traveling in the z-direction gives the h_+ and h_x components of:

$$h_{xx} = -h_{yy} = \frac{32\pi^2 G}{Rc^4} M r_0^2 f_{orb}^2 \cos 2(2\pi f_{orb})t \tag{1.10}$$

$$h_{xy} = -h_{yx} = -\frac{32\pi^2 G}{Rc^4} M r_0^2 f_{orb}^2 \sin 2(2\pi f_{orb})t. \tag{1.11}$$

To get a better understanding about the amplitude of the strain, consider the following calculation for the strength of gravitational waves produced in a laboratory setting [6]. A dumbbell consists of two masses of one tonne each at either end of a rod two meters long. The dumbbell is spun about its axis at a frequency of $f_{\rm orb} = 1$ kHz. From Equations 1.10 and 1.11, the amplitude of the gravitational waves produced by the spinning dumbbell is $h_{\rm lab} = 2.6 \times 10^{-33}\text{m} \times \frac{1}{R}$. The emitted radiation is distinguishable from near-field effects only at distances comparable or greater than one wavelength. With $f_{\rm orb} = 1$ kHz, the wavelength of the emitted radiation is $\lambda = 300$ km. Plugging this distance in to the equation for $h_{\rm lab}$ yields a gravitational wave amplitude of $h_{\rm lab} = 9 \times 10^{-39}$. The amplitude of gravitational waves produced on earth is therefore negligible.

Having calculated the extremely small amplitude of gravitational waves originating from earth, the cosmos is the next logical place to look for a source of gravitational waves. Objects in outer space can have much larger mass than anything on earth, which in combination with higher energies and velocities, can produce larger amplitudes of gravitational waves. Astrophysical gravitational waves sources are divided into short-duration bursts and continuous sources. Possible sources for gravitational waves are compact binary systems of neutron stars or black holes. These systems emit gravitational waves as their orbital period decreases. The amplitude and frequency of the gravitational waves increase with time and reach their maximum in the final stages of the inspiral and merger of the two compact objects. The inspiral and merger can be modeled using post-Newtonian approximations and numerical relativity.

To get a sense of the scale of gravitational waves produced by astrophysical sources, consider the following example [6]. Two binary neutron stars each have a mass of 1.4 solar masses or 3×10^{30} kg. The neutron stars each have a radius of 10 km, so the closest that they can be to each other is 20 km. At this closest distance, the binary neutron starts will

orbit at a frequency of 400 Hz. Assuming the binary system is in the Virgo Cluster at a distance of 15 MPc or 4.5×10^{23} m, then the maximum gravitational wave amplitude at earth is $h = 10^{-21}$. While this amplitude is greater than the one produced by the dumbbell in the previous example, it is still extremely small and requires a very sensitive detector to measure the effect of the gravitational wave.

Gravitational waves are also predicted to be emitted in a short burst from core-collapse supernovae, but models of this source are not well constrained. As an order of magnitude estimate, a supernova located 10 kpc from earth that releases $10^{-7} M_{\odot} c^2$ in gravitational wave energy would produce a strain of $h = 10^{-21}$ [8]. A source of long-duration gravitational waves is a non-axisymmetric rapidly rotating neutron star. These neutron stars emit gravitational waves at twice their orbital frequency and can be modeled as a sinusoid with an approximately constant frequency and amplitude.

1.3 Gravitational wave detectors

Joseph Weber pioneered the first attempt to detect gravitational waves in the 1960s using resonant aluminum cylinders, also known as bar detectors [9]. Weber designed his bar detectors to respond to gravitational waves at the bar's resonance frequency. The passing gravitational wave would cause the bar to ring (like a metal tunning fork) and change in size. The bar's motion was detected by piezoelectric sensors placed on the sides of the bar. To increase the sensitivity of, the size of the bar was increased to 2 meters in length and 1 meter in diameter. Despite the increase in sensitivity from the size of the bar and from cooling the bars to cryogenic temperatures to reduce its Brownian motion, the bar detectors never successfully detected a gravitational wave.

To improve upon the sensitivity of the bar detectors, Rai Weiss proposed using a Michelson interferometer to construct an antenna for detecting gravitational waves [11]. Interferometric detectors use light from a laser to compare the length of two arms of the interferometer. The light from the laser is split in half by a beamsplitter. Each half of the light travels to a distant mirror, reflects off the mirror, and returns to the beamsplitter.

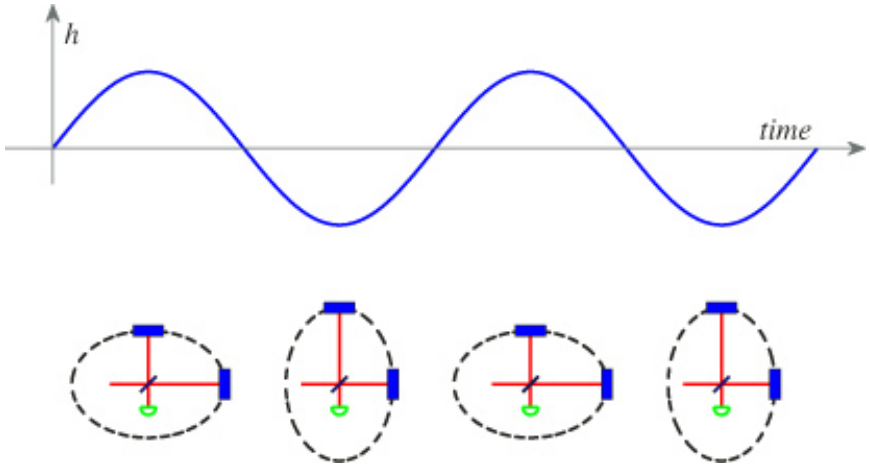

Figure 1.2: An illustration of the effect of a gravitational wave on the test masses of a Michelson interferometer [10]. As the gravitational wave passes the interferometer, traveling in the direction perpendicular to the page, the horizontal and vertical arms are stretched and squeezed alternately within one period of the passing wave. The strain of the wave, $h = {}^{\Delta L}/_{L}$, determines how much the length of the arms changes.

When the light from the two paths combines at the beamsplitter, it interferes constructively or destructively depending on the difference in phase between the two beams of light. The interference pattern is detected by a photodetector, which produces an electric signal proportional to the electric field of the light incident on it. Thus, the electrical signal at the output of the photodetector provides information on the difference in path length between the two arms of the interferometer. When a quadrupolar gravitational waves passes through the detector, it causes the length of one arm of the interferometer to increase while causing the length of the orthogonal arm to decrease. The change in each arm's length is proportional to the strain, h, induced by the gravitational wave $h = {}^{\Delta L}/_{L}$. This change in path length gives rise to a difference in phase between the beams of light that travel in each of the arms, and in turn changes the amount of light detected by the photodetector. An illustration of the effect of a gravitational wave and a Michelson interferometer is shown in Figure 1.2.

The construction of large-scale interferometric gravitational wave detectors began in the 1990s with the construction of the two Laser Interferometer Gravitational-wave Observatory (LIGO) detectors in the USA [12, 13], the VIRGO detector in Italy [14], and GEO 600 in

Germany [15]. The first generation of gravitational wave interferometers collected data for several years in the early 2000s, and while they did not detect any gravitational waves, they did produce upper limits on the rates and strength of gravitational waves (see for example [16]).

In 2010, the LIGO and VIRGO detectors stopped observing and began a series of upgrades toward an improved, second generation of gravitational wave detectors. A few of the upgrades from the initial detectors to the advanced detectors include increasing the laser power, increasing the mass of the test masses, adding additional optical cavities, and improving the suspension system used to isolate the test masses from seismic noise [17, 18]. The Advanced LIGO and VIRGO detectors will be a factor of 10 times more sensitive than the first generation of detectors when they reach their design sensitivity in the next couple of years.

In order to achieve a sensitivity required to detect gravitational waves, the LIGO interferometers build upon the basic Michelson interferometer. A diagram of the optical layout of LIGO is shown in Figure 1.3, and an aerial view of both detectors is shown in Figure 1.4. The laser beam passes through an Input Mode Cleaner, Faraday Isolator (FI), and power recycling mirrors before reaching the beamsplitter. The Input Mode Cleaner is used to clean the spatial mode of the laser beam and ensure that a Gaussian fundamental mode is sent to the interferometer. The FI prevents light reflected from the interferometer from reaching the laser and damaging it. The power recycling mirror (PRM) forms one side of the power recycling cavity. The PRM reflects the light that returns from the interferometer back into the interferometer to increase the amount of circulating power within the interferometer.

After passing through the beamsplitter, each beam transmits through an input test mass (ITM) and travels 4 km before reflecting off the end test mass (ETM). The ITM and ETM form a resonant Fabry-Perot cavity. The Fabry-Perot cavity causes the light to travel between the ITM and ETM approximately 300 times, thereby effectively lengthening the

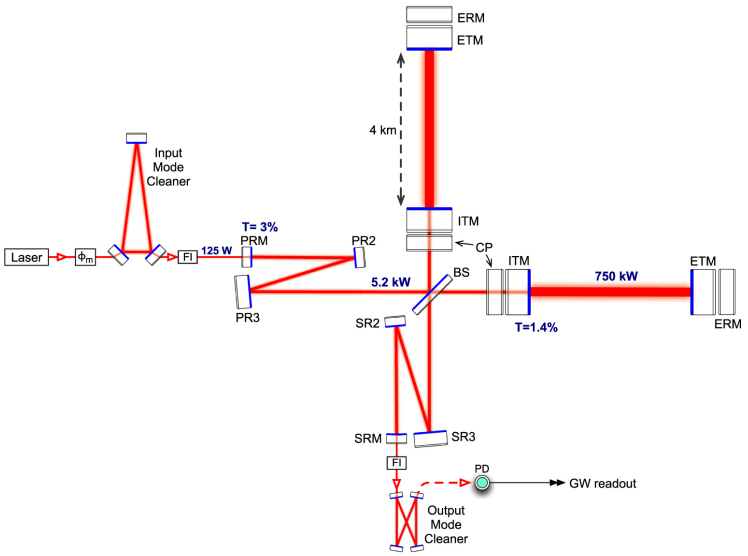

Figure 1.3: Advanced LIGO optical layout [17]. The laser is passed through an Input Mode Cleaner to spatially clean the optical mode sent into the interferometer. The interferometer contains 4 km long Fabry-Perot cavities in both arms to increase the circulating power and effectively lengthen the arm. The power recycling mirror (PRM) reflects the light that is sent back toward the laser and sends it back into the interferometer to further increase the circulating power. The signal recycling mirror (SRM) is used to tune the interferometer's response to a gravitational wave signal. The light transmitted through the SRM is passed through an Output Mode Cleaner to spatially clean the beam before it is detected on the photodetector (PD).

Figure 1.4: Aerial view of the LIGO detectors in Livingston, LA (left) and Handford, WA (right) [19]

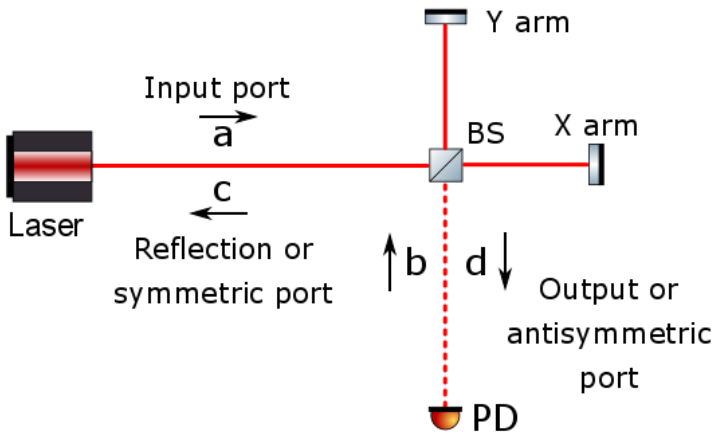

Figure 1.5: Schematic of a basic Michelson interferometer. The basic Michelson interferometer has inputs from the laser at a and the vacuum field at b with outputs at c and d. The vacuum field that enters at b superimposes with the light circulating in the interferometer, and the combined field is detected by the photodector (PD) at the output d.

arm. Since the gravitational wave strain induces a change in arm length proportional to the total length of the arm, the addition of the Fabry-Perot cavities increases the sensitivity of the interferometer by about a factor of 300.

After both beams recombine at the beamsplitter, the light returns to the input port of the interferometer, where it is reflected by the PRM, or enters the output port of the interferometer. The output port contains a signal recycling mirror (SRM), which forms a cavity with the rest of the interferometer. The signal recycling cavity is resonant for sidebands created by a passing gravitational wave and amplifies the gravitational wave signal in the interferometer. After the light passes through the SRM, it transmits through another FI before entering the Output Mode Cleaner, whose function is to clean the spatial mode of the beam before it is detected by the photodetector (PD).

1.3.1 Simple Michelson interferometer as a gravitational wave detector

To better understand how a Michelson interferometer can be used to detect gravitational waves, it is instructive to consider how a passing gravitational wave affects the light that is detected at the output of the interferometer. A simplified version of the LIGO detectors is shown in Figure 3.13. The light from the laser is injected into the interferometer

though the input port. The beamsplitter can be represented by the matrix [20, 21]

$$\mathbf{BS} = \begin{pmatrix} r & it \\ it & r \end{pmatrix} = \frac{1}{\sqrt{2}} \begin{pmatrix} 1 & i \\ i & 1 \end{pmatrix}, \tag{1.12}$$

with r and t the reflectivity and transmissivity of the beamsplitter and the rightmost side of the equation assuming a perfect 50-50 beamsplitter. The output of the beamsplitter is then given by [21, 22]

$$\mathbf{out}_{\mathrm{BS}} = (\mathbf{BS})\mathbf{in}. \tag{1.13}$$

After passing through the beamsplitter, the light travels down the x and y arms of the interferometer and experiences a phase shift of $\phi_x = \frac{2\omega L_x}{c}$ and $\phi_y = \frac{2\omega L_y}{c}$, where L_x and L_y are the lengths of the arms. A passing gravitational wave induces a phase shift of $\frac{h_+}{2}$ in the x arm and $-\frac{h_+}{2}$ in the y arm. The gravitational wave creates a differential change in the length of the arms. The arm lengths can then be written in terms of the common L_+ and differential L_- arm lengths. Likewise the phases can be broken into the common and differential parts by $\phi_x = \Phi + \phi$ and $\phi_y = \Phi - \phi$ with

$$\Phi = \frac{2\omega}{c}\left(L_+ + \frac{L_- h_+}{2}\right) \tag{1.14}$$

$$\phi = \frac{2\omega}{c}\left(L_- + \frac{L_- + h_+}{2}\right). \tag{1.15}$$

The phase accumulated by the light in the arms can then be represented by

$$\mathbf{A} = \begin{pmatrix} e^{(i\phi)} & 0 \\ 0 & e^{(-i\phi)} \end{pmatrix}. \tag{1.16}$$

The light from both arms recombines at the beamsplitter, and the output of the interferometer can be written in terms of the input of the interferometer by

$$\mathbf{out} = (\mathbf{BS})\mathbf{A}(\mathbf{BS})\mathbf{in}$$
$$\begin{pmatrix} c \\ d \end{pmatrix} = e^{i(\Phi+\pi/2)} \begin{pmatrix} \sin\phi & \cos\phi \\ \cos\phi & -\sin\phi \end{pmatrix} \begin{pmatrix} a \\ 0 \end{pmatrix}$$

The photodetector at the output of the interferometer measures the power of the light incident on it, which can be written as

$$P_{\text{out}} \propto |d|^2 = |a|^2 \cos^2\phi. \tag{1.17}$$

As seen in Equation 1.17, no light is sent to the output port of the interferometer when $\phi = \frac{\pi}{2}$. This condition is called the dark fringe and does not produce a linear signal for a passing gravitational wave. To gain a linear signal, a small DC offset Δ_{dc} is set so that the length of the two interferometer arms is slightly different so that $L_- = \frac{(\pi/2+\Delta_{dc})c}{2\omega}$. Using the small angle approximation, Equation 1.17 becomes [22]

$$P_{\text{out}} \propto |a|^2 \left(\Delta_{dc}^2 + \frac{2\Delta_{dc}\omega L_+}{c} h_+\right), \tag{1.18}$$

where the light measured at the output port is now linearly proportional to the gravitational wave strain.

1.4 Noise sources

Various sources of noise limit the strain sensitivity of gravitational wave detectors such as Advanced LIGO and ultimately limit the number of gravitational wave detections. The noise sources can create a differential change in the arms of the interferometer and produce a change in power at the output photodetector that can mimic or hide a gravitational wave signal. A calculated noise budget for Advanced LIGO at its design sensitivity is shown in

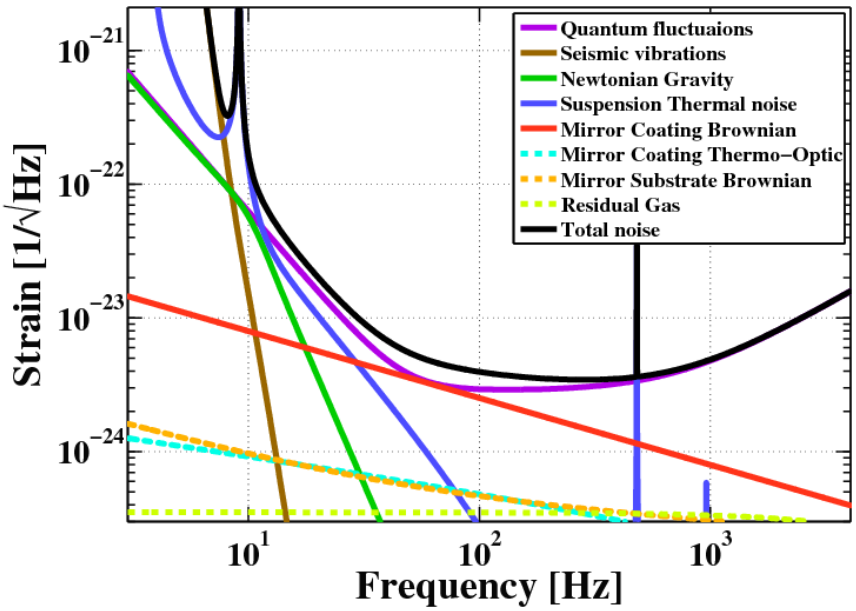

Figure 1.6: Advanced LIGO design sensitivity noise budget [24]. Quantum noise and thermal noise are the limiting noise sources above about 30 Hz. Each of the noise sources is added in quadrature to produce the total noise (black curve).

Figure 1.6. Each of the individual noise sources shown in Figure 1.6 add in quadrature to yield the total noise of the detector as a function of frequency.

For frequencies below 10 Hz, the largest noise sources are seismic vibrations and suspension thermal noise [6]. Seismic motion originates from disturbances such earthquakes and human activity, which cause the ground to shake. The seismic vibrations travel through the earth's surface and cause the distance between the test masses to change, thereby disturbing the measurement of their position. LIGO's optics are suspended from a multi-stage pendulums to isolate them from the seismic motion of the ground. The mechanical properties of the suspension system, however, introduce another source of noise called suspension thermal noise [23]. Suspension thermal noise originates from losses in the material of the wires and fibers that suspend the test masses and can be improved by using materials with lower mechanical loss.

The intermediate frequencies between 10 Hz and 100 Hz are limited by suspension thermal noise, mirror coating thermal noise, and quantum noise. Coating thermal noise

is produced by the reflective coatings on the surfaces of the test masses to make them highly reflective mirrors [25]. The Brownian motion of these reflective coatings causes a fluctuation in the position of the mirror's surface. The quantum noise at these frequencies is a result of the quantum nature of the light used to measure the position of the test masses. The uncertainty in the photons' momentum when they reflect off the surface of the optics imparts a noisy back-action force that disturbs the position of the test masses in future measurements. This disturbance is know as quantum radiation pressure noise and will be discussed in more detail in the following chapters.

Above 100 Hz, the sensitivity of Advanced LIGO is also limited by quantum noise. At these frequencies, the quantum nature of the photons causes an uncertainty when they are detected by a photodetector at the output of the interferometer. This counting uncertainty or shot noise will be discussed further in the next section.

1.5 Introduction to quantum noise and squeezed light

This section provides a brief introduction to quantum noise and how it limits interferometric gravitational wave detectors. It also introduces the concept of squeezed light and demonstrates how it can be used to improve the sensitivity of the detectors.

1.5.1 Quantization of the electric field and noise in the sideband picture

The quantized electric field can be written as [26]

$$E(t) = \varepsilon_0 \left(a(t) e^{-i\omega t} + a^\dagger(t) e^{i\omega t} \right), \tag{1.19}$$

where $a^\dagger$ is the creation operator, a is the annihilation operator, and $\varepsilon = \sqrt{\hbar\omega / \epsilon_0 V}$ is a normalization factor with ϵ_0 the permitivity of free space and V the volume of the mode. The time dependent creation and annihilation operators oscillate at the optical frequency ω. A mode is resonant in an optical cavity when the condition

$$\omega = \frac{2\pi c}{n\lambda} \tag{1.20}$$

is met, with n being an integer.

It is often useful to consider the sidebands or noise quadratures of the field for understanding quantum noise. For a field with frequency ω, the carrier frequency is ω, and the sideband fields are at frequencies $\omega \pm \Omega$. An electric field composed of an average value $\bar{E}$ and fluctuations $\delta E(t)$ can be written as

$$E(t) = \left(\bar{E} + \delta E(t)\right) e^{i\omega t} + h.c. \tag{1.21}$$

Amplitude modulations and phase modulations are two types of modulations, or variations in the properties of the electromagnetic wave. Adding an amplitude modulation to the electric field in Equation 1.21 yields [22]

$$(1 + \Gamma \cos \Omega t) E e^{i\omega t} + h.c. = E e^{i\omega t} + \frac{\Gamma E}{2} e^{i(\omega+\Omega)t} + \frac{\Gamma E}{2} e^{i(\omega-\Omega)t} + h.c., \tag{1.22}$$

where Γ is the modulation index. Similarly, adding a phase modulation results in [22]

$$E e^{i\omega t + \Gamma \Omega t} + h.c. = E e^{i\omega t} + \frac{i\Gamma E}{2} e^{i(\omega+\Omega)t} + \frac{i\Gamma E}{2} e^{i(\omega-\Omega)t} + h.c. \tag{1.23}$$

Both amplitude and phase noise can be described by the real and imaginary parts of ${}^{\delta E}/_{\bar{E}}$, respectively.

An arbitrary noisy field can be described by the sum of sidebands at different frequencies as

$$a(t) = \int_{-\infty}^{\infty} \frac{d\Omega}{\sqrt{2\pi}} \tilde{a}(\Omega) e^{i\omega t}. \tag{1.24}$$

Equation 1.19 becomes

$$E(t) = \frac{\varepsilon_0}{\sqrt{2\pi}} = \int_{-\infty}^{\infty} d\Omega \left[\tilde{a}(\Omega) e^{-i(\omega+\Omega)t} + \tilde{a}^{\dagger}(\Omega) e^{i(\omega+\Omega)t}\right], \tag{1.25}$$

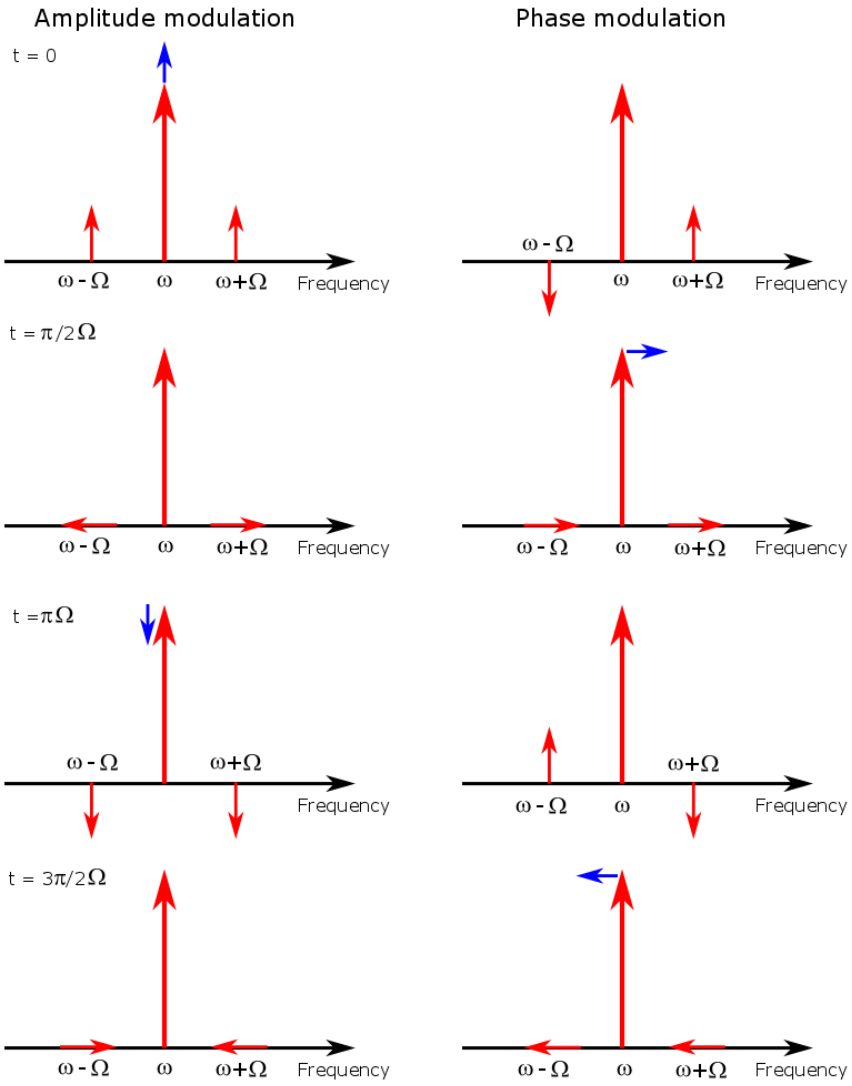

Figure 1.7: Diagram of a carrier field at frequency ω with sidebands at frequencies $\omega \pm \Omega$ creating amplitude and phase modulations. In a reference frame that rotates at the carrier frequency ω, the lower sidebands at $\omega - \Omega$ rotate counterclockwise and the upper sidebands at $\omega + \Omega$ rotate clockwise.

with the convention $a^\dagger(t) = [a(t)]^\dagger$ and $[a(\Omega)]^\dagger = a^\dagger(-\Omega)$. The sidebands at frequencies greater than and less than the carrier frequency ω are given by the operators $\tilde{a}(\Omega)$ and $\tilde{a}^\dagger(-\Omega)$ in Equation 1.25. A pictorial representation of the carrier with single sidebands at $\omega \pm \Omega$ that produce amplitude and phase modulations is shown in Figure 1.7.

1.5.2 Quadratures and uncertainty relation

As an alternative to the sideband picture, the electric field can also be quantized in terms of two quadratures X_1 and X_2. X_1 is known as the amplitude quadrature, and X_2 is called the phase quadrature. The quantized electric field can then be written as [21]

$$E(t) = \varepsilon \left(X_1(t) \cos \omega t + t(X_2(t) \sin \omega t) \right). \tag{1.26}$$

Similar to the electric field in Equation 1.21, the two quadratures can be broken down into an average value, which describes the carrier field, and a fluctuation term, which describes the modulation or noise. An arbitrary quadrature X_θ can be formed by using the two quadratures X_1 and X_2 with the equation [21]

$$X_\theta = X_1(t) \cos \theta + X_2(t) \sin \theta. \tag{1.27}$$

To better visualize X_θ, it is helpful to plot it in polar coordinates with the axes as X_1 and X_2, as shown in Figure 1.8.

The Heisenberg Uncertainty Principle places a limit on the precision of a measurement of two non-commuting variables. The canonical example for such a measurement is the simultaneous measurement of the position and momentum of a particle. The Heisenberg Uncertainty Principle states that there is a limit to the minimum of the product of the uncertainty in position and the uncertainty in momentum, namely $\Delta x \Delta p \geq \frac{\hbar}{2}$. A similar relation can be written for any two non-commuting observables.

The uncertainty relation for the creation and annihilation operators is $\Delta a \Delta a^\dagger \geq 1$, where we have normalized to 1 for convenience. Likewise, the uncertainty relation for the

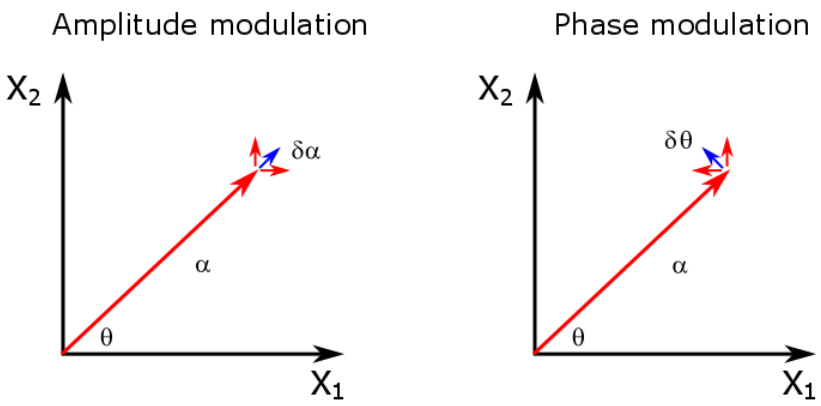

Figure 1.8: Diagram of amplitude and phase modulations in the quadrature picture with axes X_1 and X_2. The state has an amplitude of α, represented by the length of the vector, and a phase of θ, represented by polar angle. The sidebands at frequencies $\omega \pm \Omega$ rotate around the carrier at a frequency of Ω and produce modulations (blue) on the carrier.

two quadrature operators is [21]

$$\Delta X_1 \Delta X_2 \geq 1. \tag{1.28}$$

The uncertainty in X_1 and X_2 must be taken into account in the phasor picture described above. To do so, an area of uncertainty is added to the tip of the phasor, as described below and shown in Figure 1.9. For experimental measurements of the power spectral density, the uncertainty relation is written in terms of the variance [21, 22]

$$V(\theta, \Omega) V(\theta + \pi/2, \Omega) \geq 1, \tag{1.29}$$

for two orthogonal quadratures θ and $\theta + \pi/2$ at a sideband frequency Ω.

Next, we will apply the uncertainty relations to two quantum mechanical states of light that are of interest, namely the vacuum or ground state of the electromagnetic field and the coherent state. The coherent states are the eigenstates of the annihilation operator, a, such that α is a complex number related to the amplitude of the fields and is related to the

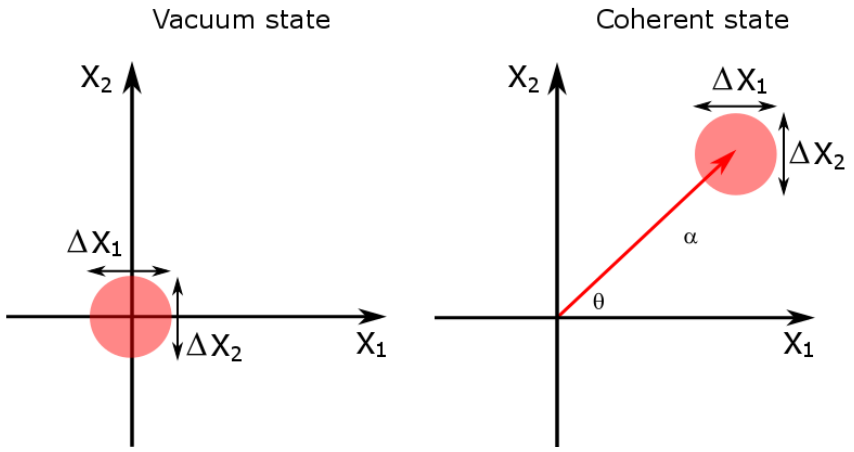

Figure 1.9: Phase-space representation of the uncertainty in quadratures X_1 and X_2 for the vacuum and coherent state, which is governed by the uncertainty relation $\Delta X_1 \Delta X_2 \geq 1$. The vacuum and coherent states have equal uncertainty in each quadrature, $\Delta X_1 = \Delta X_2 = 1$. Note that as the amplitude, α, of the coherent state increases, the uncertainty in phase, θ, decreases.

average photon number by $|\alpha|^2 = \bar{n}$. The fractional fluctuations in the photon number are

$$\frac{\Delta n}{\bar{n}} = \frac{1}{\sqrt{\bar{n}}}, \tag{1.30}$$

which decreases with increasing $\bar{n}$. The coherent state is the quantum state that is the best approximation for the classical light produced by a laser. The vacuum state is the ground state of the electric field with the eigenvalue $\alpha = 0$.

The vacuum state and the coherent state both contain equal uncertainty in each quadrature. In the sideband picture, the uncertainty in the vacuum state and coherent state can be described as the sum of uncorrelated sidebands over frequencies Ω. In the phase-space representation, the uncertainty is represented by an area of uncertainty as shown in Figure 1.9. The uncertainty area is a circle with an area of 1, which is centered at the origin for the vacuum state and at the tip of the vector for the coherent state. The vacuum state is centered at the origin because it has zero amplitude.

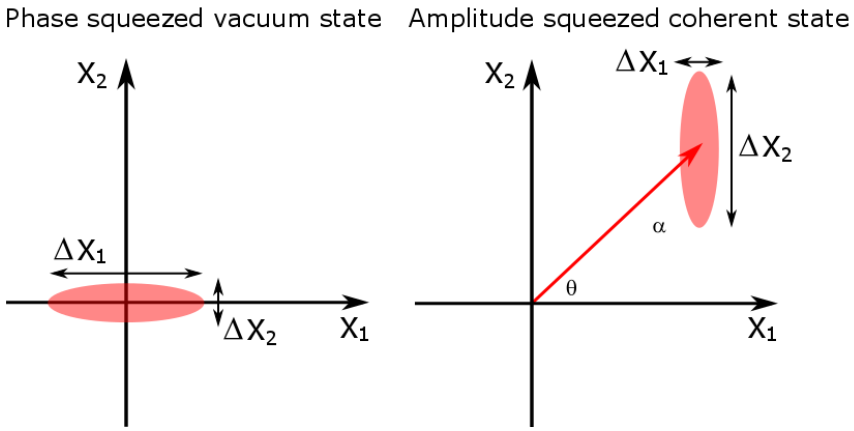

Figure 1.10: Phase-space representation of a phase squeezed vacuum state and an amplitude squeezed coherent state. The phase squeezed vacuum has a smaller uncertainty in the phase quadrature, ΔX_2, than the unsqueezed vacuum state. This comes at the expense of a larger uncertainty in the amplitude quadrature, ΔX_1, so as to satisfy $\Delta X_1 \Delta X_2 \geq 1$. The amplitude squeezed coherent state has less uncertainty in ΔX_1 and more uncertainty in ΔX_2 than the unsqueezed coherent state.

1.5.3 Squeezed light

The uncertainty relation in Equation 1.28 places a limit on the product of ΔX_1 and ΔX_2, but it does not place a constraint on ΔX_1 or ΔX_2 individually. As we saw previously, the vacuum and coherent states both have $\Delta X_1 = \Delta X_2 = 1$, but Equation 1.28 allows for either ΔX_1 or ΔX_2 to have an uncertainty less than one so long as the orthogonal quadrature has a large enough uncertainty to keep the product of uncertainties greater than one. For example, a state with $\Delta X_1 = 1/2$ and $\Delta X_2 = 2$ satisfies Equation 1.28. This is the foundation for quadrature squeezed states. An amplitude squeezed state has $\Delta X_1 < 1$, and a phase squeezed state has $\Delta X_2 < 1$. The phasor representation of a phase squeezed vacuum state and an amplitude squeezed coherent state is show in Figure 1.10.

1.5.4 Quantum noise and squeezing in gravitational wave detectors

The quantum fluctuations described in the previous sections place a limit on the sensitivity of interferometric gravitational wave detectors [27, 28]. Fluctuations in the amplitude quadrature, X_1, give rise to quantum radiation pressure noise, while fluctuations in the phase quadrature, X_2, produce shot noise.

Shot noise originates from the measurement of the optical power at the photodetector

at the output of the interferometer and arises as a result of vacuum fluctuations entering the antisymmetric port of the interferometer and superimposing on the light from the laser, as shown in Figure 1.11[27]. A measurement of optical power is equivalent to counting the number of photons that arrive at the photodetector during a given time interval [6]. A set of discrete independent events is characterized by a Poissonian probability distribution

$$p(n) = \frac{\bar{n}^n e^{-\bar{n}}}{n!}, \tag{1.31}$$

with an average of $\bar{n}$ per time interval. When $n \gg 1$, then the distribution in Equation 1.31 can be approximated with a Gaussian distribution with a standard deviation equal to $\sqrt{\bar{n}}$, with a fractional uncertainty of

$$\frac{\sqrt{\bar{n}}}{\bar{n}} = \frac{1}{\sqrt{\bar{n}}}. \tag{1.32}$$

This uncertainty is referred to as shot noise (SN), and in terms of the laser power P, the fractional uncertainty is

$$\sigma_{SN} \propto \frac{1}{\sqrt{P}}. \tag{1.33}$$

Quantum radiation pressure noise originates from the same vacuum fluctuations that enter through the antisymmetric port of the interferometer [28]. Classical fluctuations in the power from the laser are correlated in the two arms of the interferometer and do not create any differential arm length changes when the photons reflect off the suspended mirrors. The quantum fluctuations of the vacuum that enters through the output port, however, are uncorrelated, and therefore produce a differential force on each of the test masses. This differential force creates a differential arm length change, which disturbs the measurement of potential gravitational waves. The quantum radiation pressure noise

(QRPN) in the interferometer scales as

$$QRPN \propto \sqrt{P}. \tag{1.34}$$

Comparing Equations 1.33 and 1.34 demonstrates that while increasing the laser power decreases the shot noise, it comes at the expense of increasing the radiation pressure noise.

Squeezed states were first proposed as a technique to reduce the quantum noise in gravitational wave detectors by Carlton Caves [27]. Not long after Caves' theoretical work was published, Slusher et al. [29] and Wu et al. [30] achieved the first experimental measurements of squeezed light. Over the past three decades, the amount of quantum noise reduction from using squeezed states has reached 15 dB [31].

To better comprehend how shot noise and radiation pressure noise originate from the vacuum entering through the antisymmetric port and how squeezed states can be used to reduce the quantum noise in gravitational wave detectors, consider the simple Michelson interferometer shown in Figure 1.11. Light from the laser enters the interferometer from the left side of the beamsplitter as field a. At first glance, there appears to be no input from the bottom of the beamsplitter through field b. This is not true, however, when we include the vacuum state as an input field at b. We ignored the input vacuum fluctuations in section 1.3.1 but will include them below. Including the vacuum as an input at the anti-symmetric port gives rise to both shot noise and quantum radiation pressure noise as mentioned above [27].

After passing through the beamsplitter, the fields in the arms of the interferometer are

$$\begin{pmatrix} f \\ g \end{pmatrix} = \frac{1}{\sqrt{2}} \begin{pmatrix} 1 & i \\ i & 1 \end{pmatrix} \begin{pmatrix} a \\ b \end{pmatrix}. \tag{1.35}$$

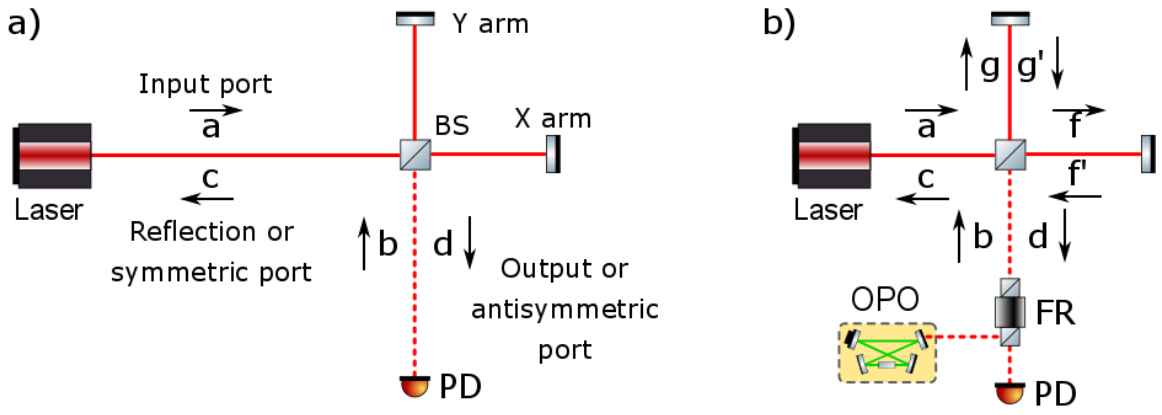

Figure 1.11: Modification of the Michelson interferometer output port to include squeezed light injection. a) The basic Michelson interferometer has inputs from the laser at a and the vacuum field at b with outputs at c and d. The vacuum field that enters at b superimposes with the light circulating in the interferometer, and the combined field is detected by the photodector (PD) at the output d. b) The interferometer is modified to include an optical parametric oscillator (OPO), which squeezed the vacuum field that enters the interferometer at b. The scqueezed vacuum field is injected into the interferometer using a Faraday rotator (FR) and is superimposed with the light that is inside the interferometer. The fields f and f' represent the outgoing and returning fields in the x arm and g and g' represent the outgoing and returning fields in the y arm. The output d of the interferometer, including the squeezed vacuum, is detected by the PD.

The difference in power in the two arms of the interferometer is then

$$P_{-} = g'^{\dagger} g - f'^{\dagger} f \propto i(b^{\dagger} a - a^{\dagger} b). \tag{1.36}$$

For an interferometer with a laser input at a, which can be assumed as a coherent state with a large amplitude α, then the differential power in the two arms becomes

$$P_{-} \propto |\alpha| X_b \left(\frac{\pi}{2} - \theta_a \right), \tag{1.37}$$

where $X_b(\theta)$ is the arbitrary quadrature for the vacuum fluctuations that enter through the anti-symmetric port b. Therefore, the variance of P_{-} is proportional to the variance of the quantum fluctuations entering through the anti-symmetric port and is scaled by the amount of input laser power. This uncertainty leads to quantum radiation pressure noise when the quantum back-action of the photons imparts a noisy force on the suspended mirrors at

the ends of the interferometer's arms. The quantum back-action is a white force with an amplitude spectral density of $\sqrt{\frac{2\pi\hbar P}{c\lambda}}$ [6], but it gains a $1/f^2$ frequency dependence above the mechanical resonance of the suspended mirrors due to the mechanical susceptibility of the suspended mirrors. The amplitude spectral density of the motion induced by quantum radiation pressure noise is then [6]

$$x_{\mathrm{QRPN}}(\omega) = \frac{1}{m\omega^2}\sqrt{\frac{2\pi\hbar P}{c\lambda}}, \tag{1.38}$$

where ω is angular frequency, m is the mass of the mirror, P is the input laser power, and λ is the laser wavelength.

For calculating shot noise, we are interested in the light that is incident on the photodetector, shown as d in Figure 1.11. If we include both the laser input at a and the vacuum fluctuations at b as inputs, then the output fields can be calculated using [22]

$$\begin{pmatrix} c \\ d \end{pmatrix} = e^{i(\Phi+\pi/2)} \begin{pmatrix} \sin\phi & \cos\phi \\ \cos\phi & -\sin\phi \end{pmatrix} \begin{pmatrix} a \\ b \end{pmatrix}. \tag{1.39}$$

The light incident on the photodetector is [22]

$$d^\dagger d = (\Delta_{dc}|\alpha|)^2 + \frac{2\omega L h_+}{c}\Delta_{dc}|\alpha|^2 - \Delta_{dc}|\alpha|X_b(-\theta_a), \tag{1.40}$$

where we have used the DC offset operating point as in Section 1.3.1, set α as the amplitude of the coherent field from the laser, and kept only the large terms. The amplitude spectral density of the shot noise is [6]

$$x_{\mathrm{SN}} = \sqrt{\frac{\hbar c\lambda}{2\pi P}}. \tag{1.41}$$

Comparing Equation 1.40 to Equation 1.37 shows that the fluctuations that cause shot noise are in the orthogonal quadrature to those that produce radiation pressure noise. In

addition, by combining Equations 1.40 and 1.37, we derive the standard quantum limit (SQL) for the position measurement of a free mass of mass m as [6, 32]

$$x_{\mathrm{SQL}} = \sqrt{\frac{4\hbar}{m\omega^2}}. \tag{1.42}$$

In order to reduce the quantum noise in gravitational wave interferometers, the anti-symmetric port of the interferometer is modified to gain the ability to change vacuum state that enters the interferometer. When the field that enters at b is phase squeezed vacuum, the uncertainty in the phase quadrature of the light detected at the PD is reduced, and thereby reduces shot noise at the expense of increasing the radiation pressure noise. On the other hand, when the vacuum is amplitude squeezed, the radiation pressure noise is reduced, and the shot noise is increased. Multiple experiments have shown the enhancement of interferometric gravitational wave detectors by injecting a squeezed vacuum into the dark port and reducing the level of shot noise [33, 34, 35]. A squeezed vacuum source is currently being installed in the Advanced LIGO and Advanced Virgo detectors with the goal of using the squeezing to reduce the shot noise during the third observational run, which is scheduled to start later this year. To date, interferometers have not been limited at low frequencies by quantum radiation pressure noise, so there has not been a demonstration of improving the low frequency sensitivity by injecting amplitude squeezed vacuum.

1.6 Gravitational wave detections

After the upgrade to Advanced LIGO was completed, the two Advanced LIGO gravitational wave detectors came online in September 2015. Much to everyone's surprise, Advanced LIGO did not have to wait long before making the first detection. On September 14, 2015, the two Advanced LIGO detectors made the first direct observation of gravitational waves [5]. The gravitational waves detected by Advanced LIGO were produced by the inspiral and collision of two black holes that were 29 and 36 times the mass of our sun.

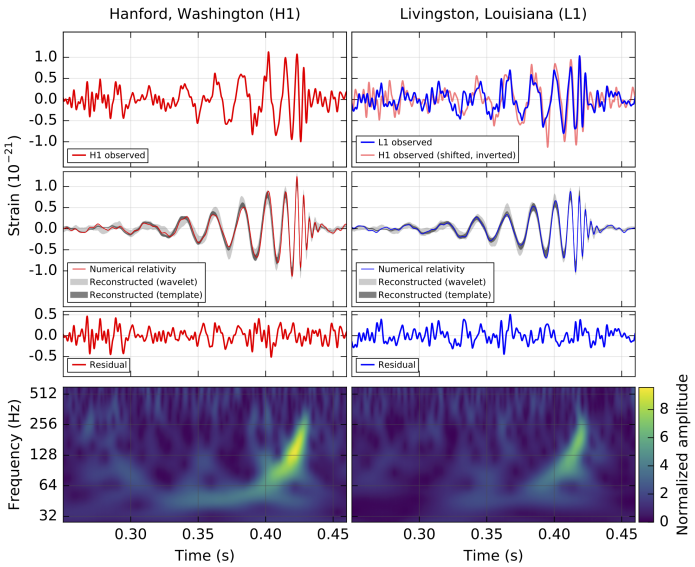

Figure 1.12: The gravitational-wave GW150914 detected by LIGO Hanford (H1, left column) and LIGO Livingston (L1, right column) [5]. The times axis is relative to September 14, 2015 at 09:50:45 UTC. The top section of the figure shows the strain detected by each detector and filtered through a 35-350 Hz bandpass filter. The top right plot shows the H1 data shifted by 6.9 ms and inverted to take the light travel time between the two detectors and the difference in orientation into account. The solid line in the second row is the numerical relativity waveform for a system with parameters consistent with the detected gravitational wave event. The shaded area is the 90% confidence region for the models. The third row of the figure shows the residuals after subtracting the filtered numerical relativity waveform from the filtered detector time series. The bottom row is a tome-frequency illustration of the strain data. The characteristic chirp signal with and increase in frequency and amplitude can be seen in both detectors.

The gravitational wave's signal, shown in Figure 1.12, swept upwards in frequency from 35 to 250 Hz and produced a peak gravitational wave strain of 1.0×10^{-21}. The signal was simultaneously observed by both the LIGO detectors in Livingston and Hanford and matched the waveform predicted by general relativity for the inspiral and merger of a pair of black holes 410^{+160}_{-180} Mpc away. The detection event had a false alarm rate of less than 1 event per 203,000 years, which is equivalent to a significance of greater than 5.1σ. The detection not only provided the first direct observation of gravitational waves, but it also proved the existence of binary stellar-mass black hole systems.

Advanced LIGO's first observing run continued until January 19, 2016. Near the end of the observing run, the two Advanced LIGO detectors made the second observation of

gravitational waves. On December 26, 2015, LIGO detected a signal from a pair of merging black holes with masses of 14 and 8 times the mass of our sun at a distance of 440^{+180}_{-190} Mpc away [36]. Despite having smaller masses than the black holes in GW150914 and only reaching a peak gravitational strain of 3.4×10^{-22}, the GW151226 detection still had a significance of greater than 5σ because it spent a longer time in the detection band. The GW151226 gravitational wave signal was observed for about 55 cycles between 35 and 450 Hz and is shown in 1.13.

After 10 months of upgrading the detectors, Advanced LIGO began its second observing run in November 2016. Two months after the start of the run, the Advanced LIGO detectors made their third observation of gravitational waves on January 4, 2017 [37]. Like the first two detections, the third observation was of a binary black hole merger. The merging black holes had masses of 31 and 19 times the mass of the sun and were 880^{+450}_{-390} Mpc with a false alarm rate of less than 1 in 70,000 years. The gravitational waveform is shown in Figure 1.13.

Seven month after the third detection, LIGO made its fourth observation of a binary black hole merger on August 14, 2017, this time with the addition of the Italian VIRGO detector [38]. The addition of VIRGO to the two LIGO detectors forms a three-detector network, which is able to decrease the uncertainty in the source localization in the sky. The masses of the binary black holes were 30 and 25 solar masses and were detected at a luminosity distance of 540^{+130}_{-210} Mpc with false alarm rate of less than 1 in 27,000 years. The three-detector network allowed the sky localization of the source to be reduced from 1160 deg^2 using only the two LIGO detectors to 60 deg^2 using all three detectors. The improved sky localization is vital to the effort to detect an electromagnetic counterpart along with the gravitational wave signal. The gravitational wave signals from the binary black hole mergers are shown in Figure 1.13, and the masses are shown in Figure 1.14.

The dawn of gravitational wave astronomy began on August 17, 2017 when the LIGO and VIRGO detectors made the first observation of gravitational waves from a binary neu-

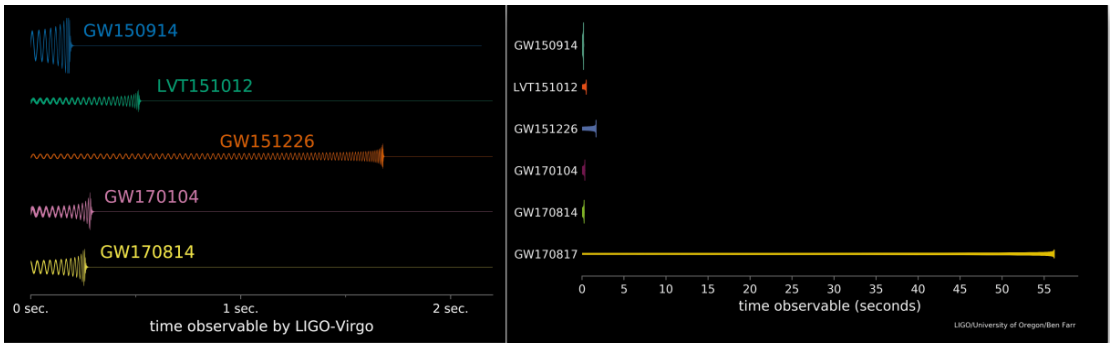

Figure 1.13: Gravitational waves detected by LIGO [39, 40]. The signals from each of the binary black hole mergers lasted less than two seconds, while the signal from the binary neutron star merger (GW170817) lasted almost one minute.

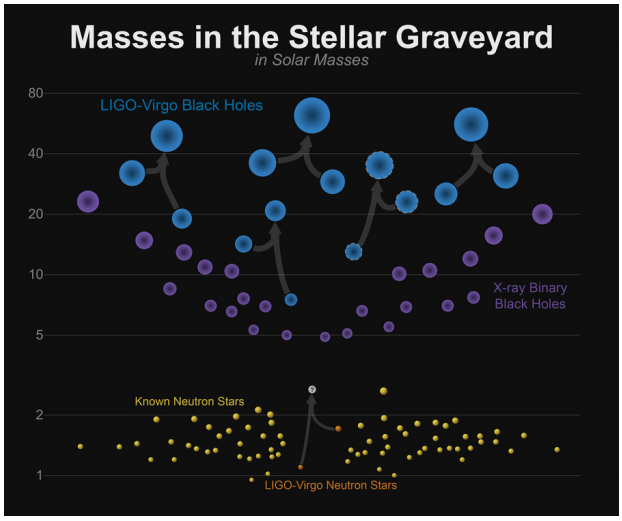

Figure 1.14: Masses of the binary black hole (blue) and binary neutron star (orange) mergers detected by LIGO. Electromagnetic observations of black holes (purple) and neutron stars (yellow) [41].

tron star inspiral [42]. The gravitational wave detection triggered an alert that was sent to electromagnetic follow-up partners who turned their telescopes toward the region of the sky in which the gravitational wave originated in hopes of observing the light that was produced in the binary neutron star merger. A burst of gamma rays was observed two seconds after the gravitational wave signal followed by the first optical counterpart less than 11 hours after the merger [43]. Follow-up observations continued for weeks as light was detected across the entire electromagnetic spectrum, shown in Figure 1.15. The gravitational wave signal from the GW100817 event is shown in Figure 1.13. The component masses of the neutron star binary are shown in Figure 1.14 in comparison to the other known stellar mass black holes and neutron stars.

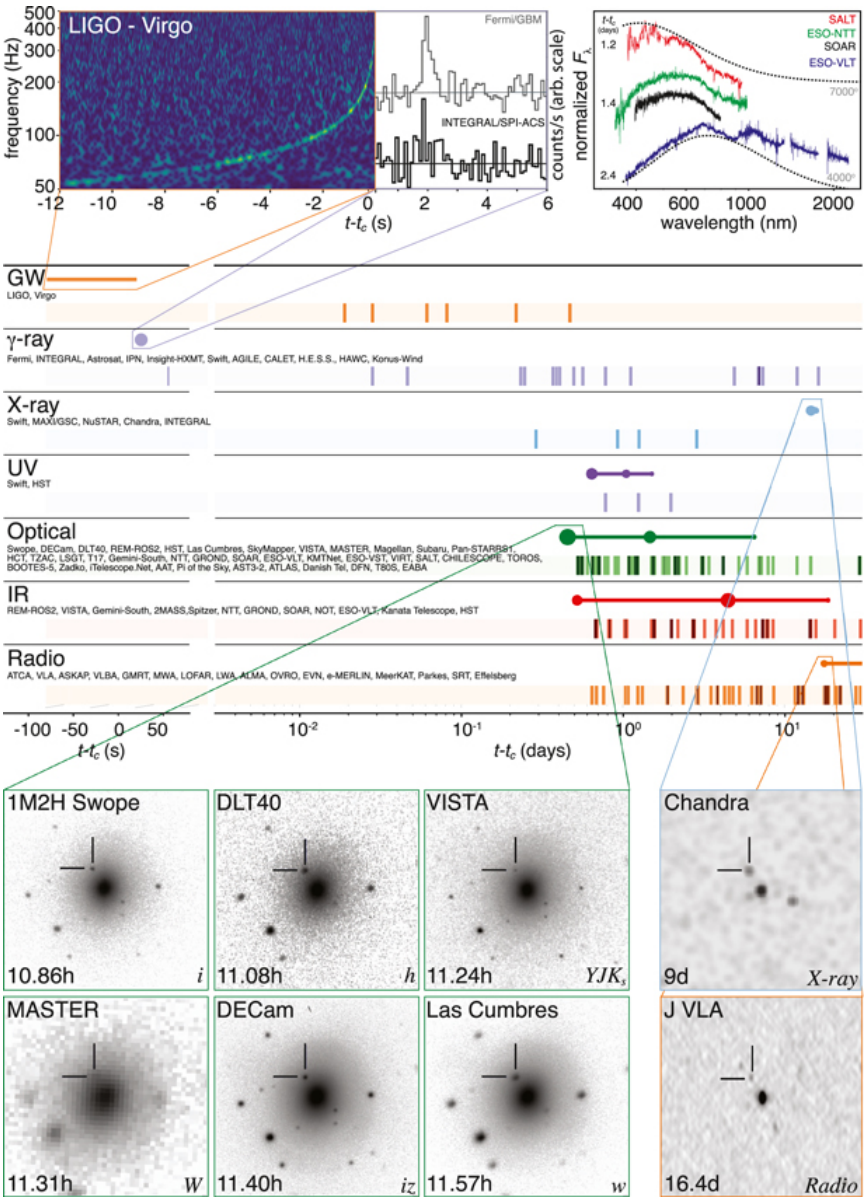

Figure 1.15: Timeline for the detection of gravitational waves and electromagnetic waves detected for GW170817 [43]. The detection of gravitational waves from the binary neutron star merger prompted a worldwide electromagnetic follow-up campaign. The first electromagnetic counterpart was detected in gamma rays only two seconds after the merger. Successive detections in optical, infrared, ultraviolet, x-ray, and radio wavelength continued for the next 16 days and beyond.

Chapter 2
Optical Springs

This chapter investigates the optomechanical interaction between laser light and a mechanical oscillator via the radiation pressure force. This optomechanical coupling can create a position dependent force on the mechanical oscillator and can be interpreted as an optical spring. Similar to a mechanical spring, the optical spring can modify the dynamics of the optomechanical system. As a result, the optical spring can be a useful tool in optomechanical experiments and plays a vital role in the experiments described throughout the rest of this thesis.

2.1 Optical spring

To understand how an optical spring is created, consider the canonical example of an optical spring in detuned Fabry-Perot cavity. An example of such a cavity is shown in Figure 2.1, with one fixed position mirror and one mirror that is free to move. Light from a laser of angular frequency ω_0 enters the cavity from the left. The equations relating the light at each point of the cavity, as seen in Figure 2.1, are [44]

$$d = \tau a - \rho h \tag{2.1}$$

$$f = e^{i\theta} d \tag{2.2}$$

$$g = -f \tag{2.3}$$

$$h = e^{i\theta} g \tag{2.4}$$

$$b = \rho a + \tau h \tag{2.5}$$

$$\theta = \tfrac{\omega_0 L}{c} \bmod(2\pi), \tag{2.6}$$

with L the length of the cavity, θ the amount of phase accumulated by the light, and ρ and τ the amplitude reflectivity and transmissivity with the condition $\rho^2 + \tau^2 = 1$ for a lossless mirror. Solving this set of equations for the light that is incident on the movable mirror

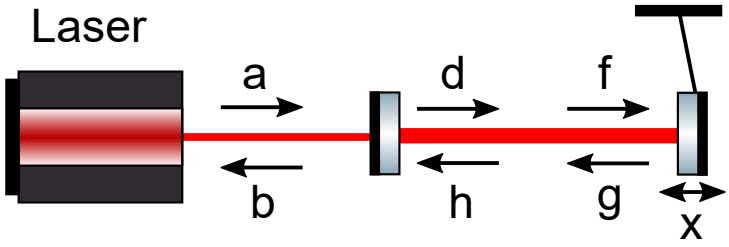

Figure 2.1: An optomechanical cavity is pumped from the left side with a laser of frequency ω_0 and power P. The input mirror has a fixed position and a power transmissivity of $T = 1 - R$, where R is is the power reflectivity. The right mirror has a mass m and is free to move and perfectly reflective.

yields

$$f = \frac{\tau e^{i\theta}}{1 - \rho e^{2i\theta}} a. \tag{2.7}$$

The amount of power incident on the movable mirror is [44]

$$P_{\text{cav}} = \frac{4}{T} \frac{1}{1 + \delta_\gamma^2} P_0, \tag{2.8}$$

where P_{cav} is the power inside the cavity, P_0 is the laser power incident on the cavity, $T = \tau^2$, $\gamma = \frac{Tc}{4L}$ is the cavity linewidth[1], and $\delta_\gamma = \frac{\theta c}{L\gamma}$ is the detuning of the cavity in units of the cavity linewidth.

The cavity is considered to be on resonance if the light that enters the cavity is in phase with the light that has already completed one or more round trips inside the cavity. This means that the length of the cavity is equal to a half integer times the wavelength of the light ($L = {}^{n\lambda}/_{2}$). When this resonance condition is met, the light circulating inside the cavity is resonantly enhanced. If the cavity is detuned from resonance by moving the position of the end mirror, the resonance condition is no longer met, and the amount of power inside the cavity decreases. Figure 2.2 shows the amount of power circulating inside the cavity as a function of detuning, where the circulating power inside the cavity

[1] γ is the half-width half maximum of the cavity Lorentzian in units of angular frequency to match the units of ω_0.

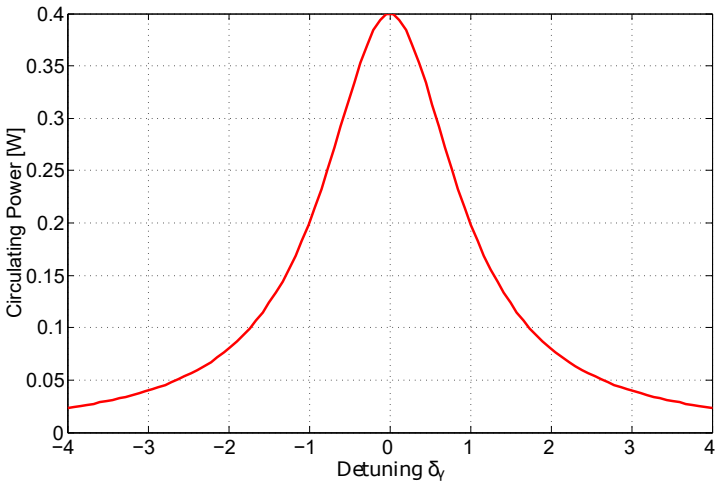

Figure 2.2: The circulating power inside the cavity as a function of the detuning from resonance. The parameters of the plot are an input power of 100 μW and a transmissivity of $T = 0.001$ of the input mirror. The sharpness of the peak depends on the the value of T.

is approximately linear for small change in the position of one of the cavity mirrors. The radiation pressure force on the movable mirror is given by

$$F_{\mathrm{RP}} = \frac{2P}{c} \tag{2.9}$$

where P is the amount of power incident on the movable mirror, and c is the speed of light. Since the radiation pressure force is directly related to the amount of power inside the cavity, then it is also proportional to the movable mirror's position. If the change in the radiation pressure force is slow compared to the response time of the cavity, which is given by the inverse of the cavity linewidth γ, then

$$\delta F = \frac{2}{c}\frac{dP}{dL}\delta L. \tag{2.10}$$

This linear relationship is analogous to Hooke's law for a mechanical spring ($F = -kx$) and is the reason why such a system is called an optical spring. Continuing with the analogy, just as a mechanical spring can connect two objects, the optical spring connects the two

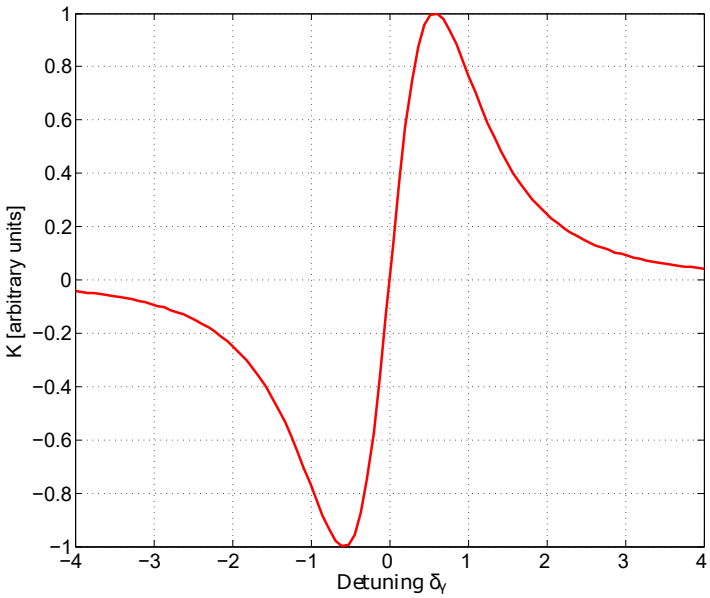

Figure 2.3: The optical spring constant as a function of the detuning from resonance. The maximum amplitude of the optical spring occurs at a detuning of $\delta_\gamma = {}^{\pm 1}/_{\sqrt{3}}$

mirrors of the cavity and has a spring constant of [44]

$$K = -\frac{2}{c}\frac{dP}{dL} = -\frac{64P_0}{T^2 c\lambda_0}\frac{\delta_\gamma}{(1+\delta_\gamma^2)^2}, \tag{2.11}$$

which is plotted in Figure 2.3.

As evident in Equation 2.11 and Figure 2.3, the optical spring constant can be either positive or negative depending on the sign of the detuning. Figure 2.4 illustrates the magnitude and direction of the optical spring force for both a positive (blue) and negative (red) detuning. For a red detuned cavity in which the cavity length is shorter than the resonance length of the cavity, the detuning is negative, which means that the direction of the antirestoring force from the optical spring is in the same direction as the mirror's displacement from equilibrium. This leads to a static instability as the mirror is driven away from equilibrium. On the other hand, the blue detuning cavity has a cavity length that is longer than the resonant length of the cavity. This positive detuning provides a restoring force from the optical spring that is in the opposite direction of the mirror's displacement from equilibrium. The restoring force moves the mirror back toward equilibrium and yields

a statically stable system.

2.2 Full optical spring

The derivation written above assumes that the motion of the movable mirror is slow and that the light inside the cavity responds instantaneously to the change in the mirror's position. This assumption breaks down, however, when the frequency of the movable mirror's motion is comparable to the rate at which the cavity responds to a change in the position of the mirror, which is given by γ^{-1}.

Taking the cavity's response time into account and allowing for the movable mirror to have a nonzero transmissivity, the optical spring is given by [44, 45, 46]

$$K_{\mathrm{OS}} = K_0 \frac{1}{\delta_\gamma^2 + (1 + i\Omega_\gamma)^2}, \tag{2.12}$$

with

$$K_0 = \frac{16\pi P_{\mathrm{in}} T_1 \sqrt{R_1 R_2^3}}{c\lambda_0 (1 - \sqrt{R_1 R_2})^3} \frac{\delta_\gamma}{(1 + \delta_\gamma^2)} \tag{2.13}$$

where P_{in} is the input laser power, T_i and R_i are the power transmissivity and reflectivity of the input mirror ($i = 1$) and end mirror ($i = 2$), λ_0 is the laser wavelength, $\delta_\gamma = {}^{\delta}/_{\gamma}$ is the laser's detuning, $\delta = \omega_{\mathrm{laser}} - \omega_{\mathrm{cavity}}$, in terms of the cavity linewidth, γ, $\Omega_\gamma = {}^{\Omega}/_{\gamma}$, Ω is angular frequency, and c is the speed of light. In the limit that the frequency of a movable mirror's motion is small compared to the cavity linewidth ($\Omega \ll \gamma$) Equations 2.12 and 2.13 reduce to

$$K_{\mathrm{OS}} = K_0 \left[1 - \frac{2i\Omega}{\gamma(1 + \delta_\gamma^2)} \right], \tag{2.14}$$

with

$$K_0 = \frac{16\pi P_{\mathrm{in}} T_1 \sqrt{R_1 R_2^3}}{c\lambda_0 (1 - \sqrt{R_1 R_2})^3} \frac{\delta_\gamma}{(1 + \delta_\gamma^2)^2}. \tag{2.15}$$

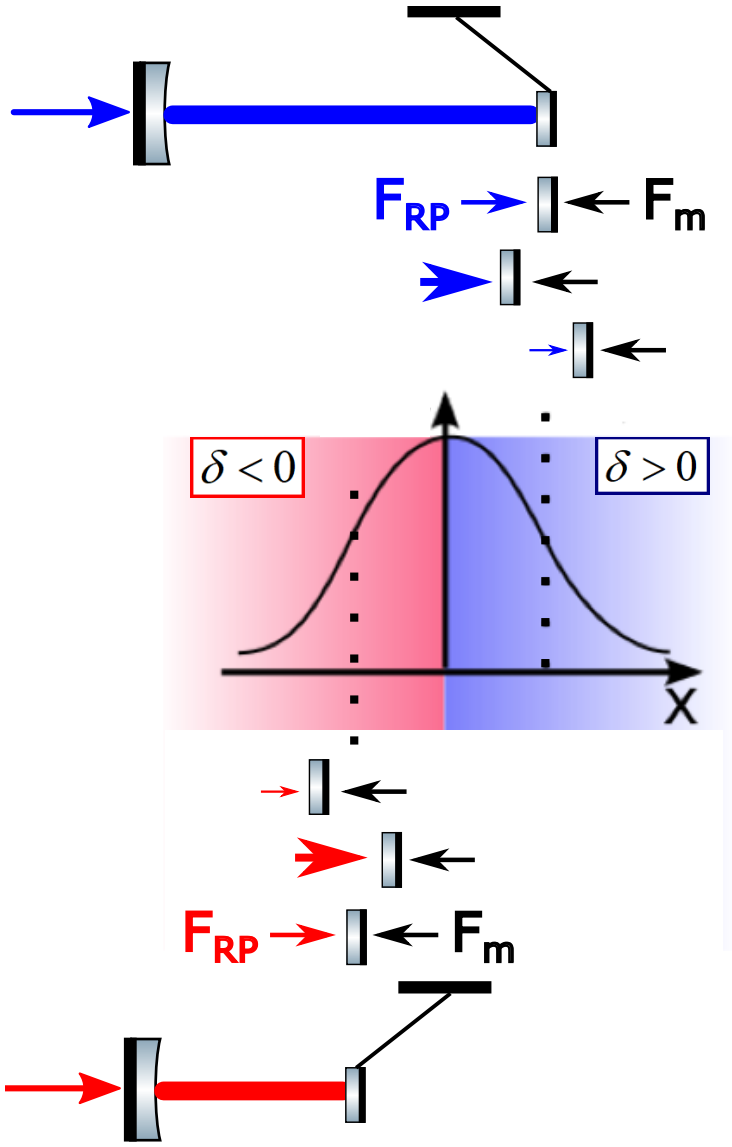

Figure 2.4: Illustration of the cavity circulating power and forces on the movable mirror as a function of the position of the movable mirror. The cavity resonance is in the center of the plot where the power inside the cavity is maximized. A blue detuned cavity ($\delta > 0$) corresponds to when the cavity length is longer than the resonant length, and a red detuned cavity ($\delta < 0$) corresponds to when the cavity length is shorter than the resonant length. The dotted lines on each side of resonance mark the equilibrium point at which the force from the optical spring, $F_{\rm OS}$, is equal to the mechanical restoring force, $F_{\rm m}$, from the mirror's suspension. The size of the arrows represent the magnitude of the force.

Equation 2.15 contains the same $\frac{\delta_\gamma}{(1+\delta_\gamma^2)^2}$ dependence as Equation 2.11.

2.3 Damping

Equation 2.14 contains a real and imaginary part, with the real part of giving rise to a frictionless spring constant K_0 that provides a restoring force, and the imaginary part representing the viscous damping of a damped harmonic oscillator. The damping coefficient Γ_{OS} is

$$\Gamma_{\mathrm{OS}} = \frac{-2K_0}{M\gamma(1+\delta_\gamma^2)}, \tag{2.16}$$

with M the reduced mass of the two mirrors. In the limit of the mass of the movable mirror being much smaller than the mass of the input mirror, M simply reduces to the mass of the movable mirror, m. Figure 2.5 displays how the delayed response of the cavity to the mirror's motion gives rise to the damping force.

It can be seen from Equations 2.12 and 2.13 that the optical spring constant can be either positive or negative depending on the sign of the detuning. The sign of K_0 also determines whether the damping coefficient Γ_{OS} is positive or negative. Equation 2.16 shows that the sign of the damping coefficient is always opposite to the sign of the spring constant. This gives rise to an unstable optical spring as a stable spring requires both a positive spring constant and a positive damping coefficient. The instability arises because a system with a positive (restoring) spring is made unstable by an antidamping force, while a system with a positive damping force experiences an antirestoring force from the negative spring.

A system with a positive spring and antidamping can be made stable by introducing a feedback loop that adds damping to the system and makes the total damping of the system positive. This can be accomplished using electronic feedback [46, 47], photothermal feedback [45, 48], or even the addition of a second optical spring with a larger, positive damping [44, 46]. The optical spring can be thought of as an optical feedback system,

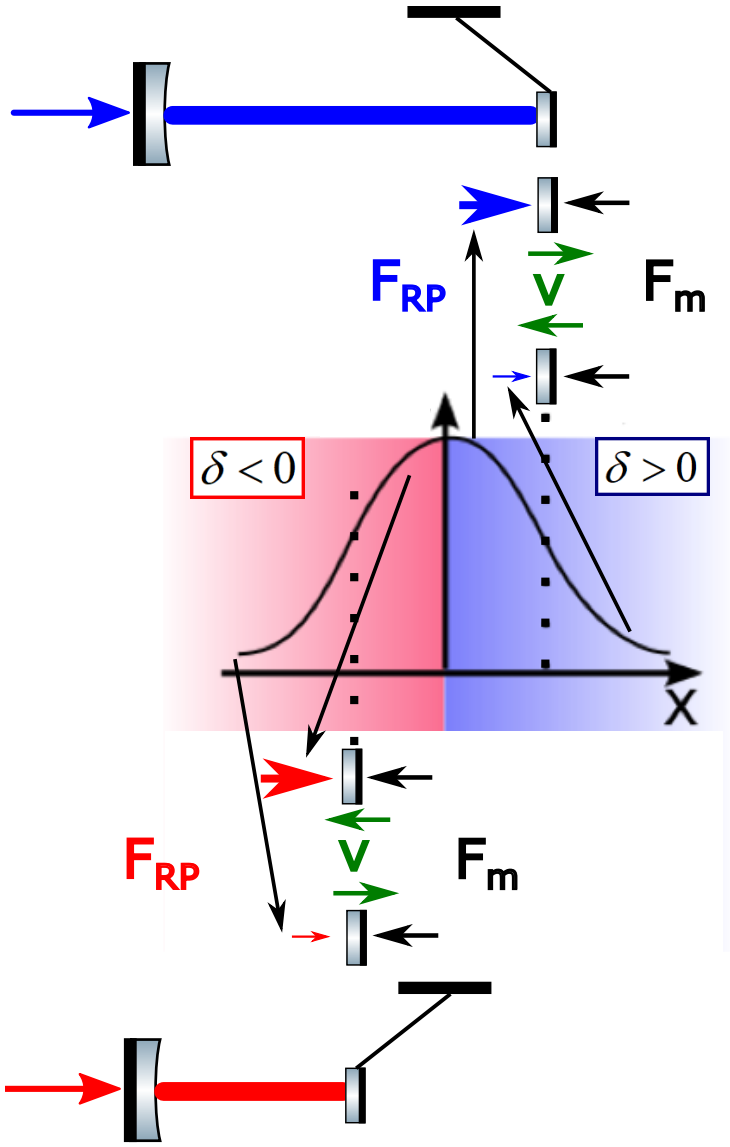

Figure 2.5: Illustration of the cavity circulating power and forces on the movable mirror when the frequency of the mirror's motion is comparable to the response time of the cavity. The green arrows indicate the direction of the mirror's movement. The cavity's response time γ^{-1} causes the force from the radiation pressure to be delayed. This delay gives rise to a damping force in the red detuned case and an antidamping force in the blue detuned case. The size of the arrows represents the magnitude of the force.

which is able to modify the dynamics of both the movable mirror and the optical field. Chapter 4 explores the stability of an optical spring from the control theory point of view.

2.4 Equations of motion and modified dynamics

It is instructive to consider the effects of the optical spring on the equations of motion for the mechanical oscillator and how the optical spring modifies the bare mechanical system. Starting from Newton's second law of motion, the differential equation for a damped harmonic oscillator is

$$m\ddot{x} = -K_{\mathrm{m}}x + m\Gamma_{\mathrm{m}}\dot{x}, \tag{2.17}$$

where K_{m} is the mechanical spring constant of the oscillator and Γ_{m} is the mechanical damping. Setting $\Omega_{\mathrm{m,bare}} = \sqrt{\frac{K_{\mathrm{m}}}{m}}$ shows that the oscillator has a resonance frequency of $\Omega_{\mathrm{m,bare}}$. Adding in the optical spring constant K_{OS} gives

$$m\ddot{x} = -(K_{\mathrm{m}} + K_{\mathrm{OS}})x + m\Gamma_{\mathrm{m}}\dot{x}. \tag{2.18}$$

The mechanical and optical spring constants combine to make the resonance frequency equal to $\Omega_{\mathrm{m,OS}} = \sqrt{\frac{K_{\mathrm{m}}+K_{\mathrm{OS}}}{m}}$.

To see how this change in resonance frequency affects the motion of the optomechanical system, consider the mechanical susceptibility or the response of the system to a force F. For the bare system with a single resonance, the susceptibility is

$$\chi_{\mathrm{m}} = \frac{x}{F_{\mathrm{ext}}} = \frac{1}{m\left(\Omega_{\mathrm{m}}^2 - \Omega^2 + i\Omega\Gamma_{\mathrm{m}}\right)}. \tag{2.19}$$

With the addition of the optical spring, the susceptibility becomes

$$\chi_{\mathrm{m,OS}} = \frac{x}{F_{\mathrm{ext}}} \approx \frac{1}{m\left(\Omega_{\mathrm{OS}}^2 - \Omega^2 - i\Gamma_{\mathrm{OS}}\Omega\right)}, \tag{2.20}$$

with the approximation valid when $\Omega_{\mathrm{OS}} \gg \Omega$ and $\Gamma_{\mathrm{OS}} \gg \Gamma_{\mathrm{m}}$. In the limit of a large optical spring, the addition of the optical spring suppresses motion below the resonance frequency by approximately

$$\left|\frac{\chi_{\mathrm{m}}}{\chi_{\mathrm{OS}}}\right| \approx \left|\frac{\Omega_{\mathrm{OS}}^2}{\Omega_{\mathrm{m}}^2}\right|, \tag{2.21}$$

with the approximation assuming $\Omega_{\mathrm{os}} \gg \Omega$. This factor of suppression may be made very large if $\Omega_{\mathrm{os}} \gg \Omega_{\mathrm{m}}$. This topic is explored in more depth in Chapter 4.

Chapter 3
Cantilever Micro-Mirror and Optomechanical Cavity Design

3.1 Introduction

In 1980, Carlton Caves predicted that quantum-mechanical vacuum fluctuations would place a limit on the sensitivity of interferometric gravitational wave detectors [28]. Over the past three decades, theoretical physicists have proposed schemes to reduce the effect of quantum back-action [49, 50, 51, 52, 53]. At the same time experimentalists have sought to verify Caves's prediction with increasingly sensitive experiments. Studying quantum mechanical motion is challenging, however, due to the fact that classical noise sources such as environmental vibrations and thermally-driven fluctuations [54] usually dominate over quantum effects. Given the imperative for more sensitive GW detectors, it is important to study the effects of quantum radiation pressure noise (QRPN) in a system similar to Advanced LIGO, which will be limited by QRPN across a wide range of frequencies far from the mechanical resonance frequency of the test mass suspension. Previous observations of QRPN have observed such subtle quantum effects, even at room temperature, but these experiments have thus far been limited to high frequencies (MHz-GHz) and in a narrow band around a mechanical resonance [55, 56, 57, 58].

The goal of this thesis was to design and construct an experiment sensitive enough to study off resonance QRPN across a broad band of audio band frequencies. This chapter outlines the theoretical calculations and modeling that influenced the experimental design and the construction of the experiment.

3.2 Thermal noise calculations

Thermal noise, which is governed by the fluctuation dissipation theorem, sets a limit on the precision of mechanical experiments [59]. Thermal fluctuations are driven by the thermal energy $k_{\mathrm{B}}T$ that is present in every degree of freedom. The power spectrum for thermal fluctuations of an oscillator with a temperature T and resonant frequencies ω_k with

effective masses m_k and losses ϕ_k is given by [60]

$$\hat{X_{\rm th}}^2(\omega) = \sum_{k=0}^{n} \frac{4k_{\rm B}T\omega_k^2\phi_k(\omega)}{m_k\omega[(\omega_k^2-\omega^2)^2+\omega_k^4\phi_k^2(\omega)]}, \tag{3.1}$$

where $k_{\rm B}$ is the Boltzmann constant and ω is angular frequency. Equation 3.1 includes a frequency dependent loss parameter [54]

$$\phi_k(\omega) = \frac{\omega}{\omega_k Q_k} \tag{3.2}$$

where the index k represents the kth mode. At the resonance of the mode, the loss parameter is related to the quality factor of the resonance by [54, 60]

$$\phi_k = \frac{1}{Q_k}. \tag{3.3}$$

The sum in Equation 3.1 adds the contribution of all the individual modes to form the total power spectrum of the oscillator.

Thermal noise models are loosely divided into viscous or velocity-dependent models and internal friction or structural damping models, depending on the source of dissipation. The amplitude spectral density of displacement for the velocity-dependent viscous thermal noise is [54]

$$x(\omega) = \sqrt{\frac{4{\rm k_B}T\omega}{Q_k m[(\omega_{\rm m}^2-\omega^2)^2+\frac{\omega^2\omega_{\rm m}^2}{Q_k^2}]}} \tag{3.4}$$

The amplitude spectral density of the viscous thermal noise model falls off proportional to ω^2 above the mechanical resonant frequency.

Structural damping models contain a frequency independent loss angle, and for a har-

monic oscillator have a displacement amplitude spectral density of [54]

$$x(\omega) = \sqrt{\frac{4\mathrm{k_B}T\omega_\mathrm{m}^2}{\omega m Q_k[(\omega_\mathrm{m}^2 - \omega^2)^2 + \frac{\omega_\mathrm{m}^4}{Q_k^2}]}}. \tag{3.5}$$

For structural damping, the thermal noise falls off as $1/\omega^{5/2}$ above the mechanical resonance frequency.

Another classification of thermal dissipation is thermoelastic loss. Thermoelastic damping is caused by coupling of the strain and temperature fields of an object that provides a energy dissipation path that allows the object to relax to equilibrium [61]. Thermoelastic dissipation exists as long as the object's thermal-expansion coefficient is nonzero. Thermoelastic dissipation is frequency dependent like the viscous models mentioned above and depends on the thermal properties of the constituent materials and the geometry of the oscillator. The thermoelastic loss angle of the kth mode is given by [60]

$$\phi_{\mathrm{te},k} = \Delta \frac{\omega\tau_k}{1 + (\omega\tau_k)^2}, \tag{3.6}$$

where

$$\Delta = \frac{\alpha^2 E_y T}{\rho C_\nu} \tag{3.7}$$

is the strength, and

$$\tau_k = \frac{\rho C_\nu l_k^2}{\kappa\pi^2} \tag{3.8}$$

is the characteristic time of the mode. In equations 3.7 and 3.8, α, E_y, ρ, C_ν, T, and κ represent the linear thermal expansion coefficient, Young's modulus, density, specific heat, temperature, and thermal conductivity of the oscillator. The variable l_k is the path length along which heat flows as the oscillator experiences stress and strain. The characteristic

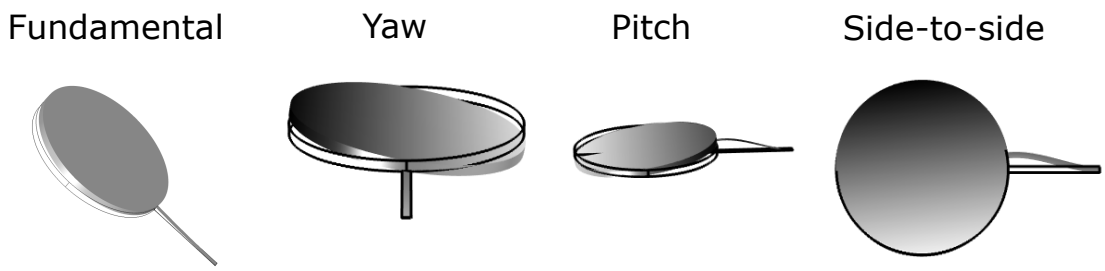

Figure 3.1: Mechanical modes of the microresonator.

time τ_k is the time it takes heat to be transfered across the distance l_k and causes a peak in the frequency response of the oscillator at $\omega = 1/\tau_k$. As a result, a resonator with a larger value for l_k will have the peak at a lower frequency ω. The peak at $\omega = 1/\tau_k$ exists because if $\omega < 1/\tau_k$, then the system remains at equilibrium and experiences very little dissipation [61]. If $\omega \gg 1/\tau_k$, then the system has very little time to relax and again experiences very little dissipation. It is only when $\omega \approx 1/\tau_k$ that dissipation occurs.

We model the thermal noise using a finite element model of the microresonator, described below in Section 3.4, in COMSOL. The finite element model of the cantilever uses the cantilever and mirror geometry as well as the mechanical properties of the GaAs cantilever and GaAs/AlGaAs mirror pad to compute the modal resonant frequencies. The mechanical modes that are most relevant for the work presented here are the fundamental mode, yaw mode, pitch mode, and side-to-side mode, all of which are shown in Figure 3.1. The model also calculates the strength of the optomechanical coupling between the laser beam and mechanical modes of the oscillator as a function of the location of the beam on the mirror pad. The mode frequencies and masses are exported from the finite element model into a Matlab script, which uses equations 3.4 and 6.1 to separately calculate the viscous and structural thermal noise spectra in the frequency domain by summing the contribution from the k modes for each model. The details of the thermal noise code are included in Appendix A.

The finite element model is later constrained by measurements to improve the model's accuracy. We directly measure the frequencies and quality factors of the fundamental mode

and the next three higher-order modes, described in 3.5 and infer the modal mass from the thermal noise measurement presented in 6. The contribution from thermoelastic damping is added by hand by adjusting the value of the Q for the drumhead mode so that the model including the structural and thermoelastic added together matches the measured thermal noise. The Q of the drumhead mode is added by hand because we are not able to directly measure the Q of the drumhead mode since it is at a very high frequency ($\sim$ MHz).

3.3 Quantum noise calculations

The quantum noise is modeled in Matlab using input-output relations, which consist of a set of equations that relate the output fields to the input fields [62, 63]. The model is performed in the frequency domain, which makes it easy to use transfer functions in the frequency domain and produce noise spectra at the output of the model. Since we are interested in a model that includes a movable mirror and strong radiation pressure effects, we must include the sideband fields that are generated by the mirror motion in addition to the carrier field. In this model, the radiation pressure forces push on the mirror at a frequency Ω, which in turn drives the motion of the mirror. The mirror motion at the frequency Ω then contributes back to the sideband fields at frequencies $\omega_0 \pm \Omega$ around the carrier frequency ω_0.

Figure 3.2 illustrates the input fields a and h to the cavity and the output fields b and g. The inputs to the quantum noise model are the laser frequency, the length of the cavity, the amount of laser power that is injected into the optomechanical cavity, the transmission and reflectivity of the cavity mirrors, the intracavity losses, and the detuning, δ_γ, of the optomechanical cavity from resonance. Cavity losses serve as an input for vacuum fluctuations to enter the cavity and are also included in the model by setting $R_i + T_i + L_i = 1$, where R_i is the mirror reflectivity, T_i is the mirror transmissivity, and L_i is the amount of losses with $i = 1, 2$. We combine the total intracavity losses of both cavity mirrors into a single loss term added to one of the cavity mirrors. The dynamics of the microresonator are added based on the same finite element model that is used for the

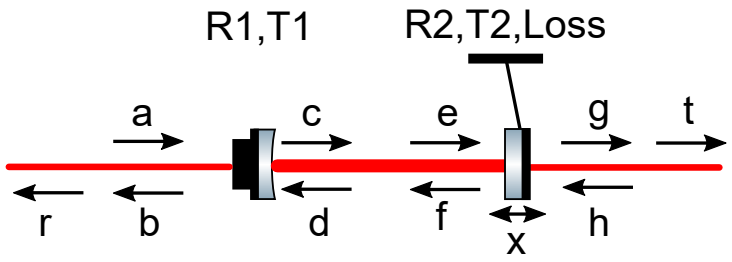

Figure 3.2: Diagram of the cavity fields. a and h are the input fields, and b and g are the output fields. The field r is the field b with an extra propagation length so that r has zero phase. The field t is g at zero phase. The output fields b and g are rotated by an extra phase factor through free space so that the amplitude and phase quadrature of the light can be referenced by the orthogonal quadratures r_1 and r_2 and t_1 and t_2. $R1$ and $T1$ are the power reflectivity and transmissivity of $M1$, and $R2$ and $T2$ are the power reflectivity and transmissivity of $M2$. The loss term represents the total intracavity loss from both $M1$ and $M2$.

thermal noise model described in section 3.2 and measurements of the Q, frequency, and modal mass of each mechanical mode. This data is used to calculate the mechanical susceptibility of the microresonator.

The input-output relations are first used to calculate the DC carrier fields $a - h$. The propagation of the carrier field can be calculated independently from the sideband propagation because the carrier is not affected by the sidebands. This is done by populating a matrix, $M0$, that relates the fields to each other. Fields a through h are assigned a number one through eight that refer to their position in the matrix. The set of input-output relations for the carrier fields are

$$\begin{bmatrix} M0_{1,1} & M0_{1,2} & \cdots & M0_{1,8} \\ M0_{2,1} & M0_{2,2} & \cdots & M0_{2,8} \\ \vdots & \vdots & \ddots & \vdots \\ M0_{8,1} & M0_{8,2} & \cdots & M0_{8,8} \end{bmatrix} \begin{bmatrix} a' \\ b' \\ \vdots \\ h' \end{bmatrix} = \begin{bmatrix} a \\ b \\ \vdots \\ h \end{bmatrix}, \tag{3.9}$$

where the unprimed elements are the inputs and the primed elements are the outputs. By looking at Figure 3.2, the field c, which is assigned the number three, is equal to the transmission of a through $M1$ and the reflection of d off $M1$. The matrix elements that

describes this are $M0(3,1) = \sqrt{(T1)}$ and $M0(3,4) = -\sqrt{(R1)}$. The rest of the elements in $M0$ are populated in a similar manner. More details on each of the matrix elements are included in Appendix A. Inverting the matrix $M0$ gives the propagating fields in terms of the input fields. By inverting the matrix, we now have access to information about the amplitude and the phase of the fields at every location inside and outside the cavity. This can be used, for example, to calculate the static radiation pressure force on the movable mirror. This is done using the intracavity field e and squaring it to convert into the units of power. Solving for the output carrier also can be used to calculate the amount of light that is transmitted and reflected by the cavity by looking at the absolute value squared of the fields t and r.

The second part of the quantum noise calculation is the population of the matrix M that contains information about the sideband fields at frequencies $\omega_0 \pm \Omega$. The propagation of the sideband fields depends on the propagation of the carrier, so they are calculated after the input-output relations for the carrier fields. The two-photon formalism developed by Schumaker and Caves [64, 65] treats the two sideband fields, $\omega_0 \pm \Omega$, as two quadrature fields $a_{1,2}(\Omega)$. We define the two quadratures as a vector

$$\mathbf{a} = \begin{pmatrix} a_1 \\ a_2 \end{pmatrix} \tag{3.10}$$

with the frequency dependence suppressed for simplicity of notation. Each field a through h now contains two quadratures, namely the amplitude quadrature and phase quadrature. For instance, the amplitude quadrature of the field a is designated by a_1, and the phase quadrature is designated by a_2.

The input-output relations for each sideband frequency Ω are described by the following

set of linear equations

$$\begin{bmatrix} M_{1,1} & M_{1,2} & \cdots & M_{1,n} \\ M_{2,1} & M_{2,2} & \cdots & M_{2,n} \\ \vdots & \vdots & \ddots & \vdots \\ M_{n,1} & M_{n,2} & \cdots & M_{n,n} \end{bmatrix} \begin{bmatrix} \mathbf{a}^{(1)} \\ \mathbf{a}^{(2)} \\ \vdots \\ \mathbf{a}^{(n)} \end{bmatrix} = \begin{bmatrix} \mathbf{u}^{(1)} \\ \mathbf{u}^{(2)} \\ \vdots \\ \mathbf{u}^{(n)} \end{bmatrix}, \tag{3.11}$$

where $\mathbf{a}^{(i)}$ with $i = 1, 2, ..., n$ are the n quadrature fields in the optomechanical system and $\mathbf{u}^{(i)}$ with $i = 1, 2, ..., n$ are the n input quadrature fields made up of the laser input $\mathbf{l}^{(i)}$ and vacuum fluctuations $\mathbf{v}^{(i)}$ that enter through lossy ports or mirrors. Each element of $\mathbf{a}$ and $\mathbf{u}$ is a two-dimensional vector that includes the amplitude and phase quadrature as represented in Equation 3.10. The fact that sidebands with different frequencies propagate independently from each other allows us to use the input-output relations described by this set of equations for each frequency Ω. The matrix $M_{i,j}$ with $i, j = 1, 2, ..., n$ contains the information about the elements in the optical system, such as the reflectivities and transmissivities of the mirrors. The matrix $M_{i,j}$ also contains information about small displacements of the movable mirror and forces on the movable mirror. The 22 by 22 matrix $M_{i,j}$ relates all of the sideband fields and mirror dynamics to each other. Inverting the matrix $M_{i,j}$ yields $\mathbf{a}^{(i)}$ in terms of the inputs $\mathbf{u}^{(i)}$, which provides the frequency dependent transfer functions used to study the system.

The elements of iM contain many useful transfer functions for calculating the quantum noise and dynamics of the optomechanical cavity. More details about the individual matrix elements are in Appendix A. One example of what can be calculated with iM uses the matrix element $1/iM(t_1, X)$,which calculates the shot noise level for the light that is detected at the cavity output t_1. The effect of the optical spring introduced in Chapter 2 can also be calculated within the code by studying the relationship between fluctuations in the amplitude quadrature of the input and the amplitude quadrature of the field transmitted through the cavity. The optical spring suppresses amplitude fluctuations below the optical

spring frequency as shown in Equation 2.21. This response is calculated using the element $iM(t_1, a_1)$ for a laser with an input at a or $iM(r_1, h_1)$ for a laser with an input at h. In the code included in Appendix A, the input output relations can be done either as a function of frequency as described here or as a function of the readout angle.

Effects from quantum radiation pressure is also included in the code. Quantum radiation pressure noise is created by fluctuations in the amplitude quadrature of input sideband fields. The amplitude quadrature fluctuations modulate the amount of power incident in the movable mirror and cause it to move. This motion, in turn, creates phase modulations in the carrier field, which creates additional sidebands. We are interested in calculating the quantum radiation pressure effects that are observable by a single photodetector, which is only sensitive to the amplitude quadrature of the light. Taking this into consideration, the QRPN in the field t_1 is calculated by adding the contributions from each of the input fields in quadrature. The input fields of interest are a_1, a_2, h_1, and h_2 for a lossless cavity. Adding losses to $M1$ means that fields b_1, b_2, c_1, and c_2 become inputs for vacuum fluctuations. Their contribution to the total quadrature sum scales with a factor of $\frac{L}{1-L}$ so that in the limit of no losses ($L = 0$) these terms do not contribute. The QRPN is calculated using these input-output relations and is shown in the figures in section 3.4.

3.4 Cantilever mirror design

One of the key elements of the optomechanical cavity described in this chapter is the microresonator that forms one of the Fabry Perot cavity mirrors. The microresonator is fabricated in collaboration with Garrett Cole from Crystalline Mirror Solutions. The cantilever microresonators are fabricated from a molecular-beam-epitaxy-grown $GaAs/Al_xGa_{1-x}As/In_yGa_{1-y}P$ structure using a double etch stop technique. Alternating layers of GaAs and $Al_{0.92}Ga_{0.08}As$ form a distributed Bragg reflector. The GaAs is a high index material, and the $Al_{0.92}Ga_{0.08}As$ is a low index material. At room temperature, the mirror's center wavelength for reflection is 1078 nm so that the center frequency will shift to 1064 nm when the structure is cooled to cryogenic He^4 temperatures in future experi-

Table 3.1: Mechanical and thermal properties of GaAs and $Al_{0.92}Ga_{0.08}As$ [74]. [a] Value from the Ioffe Institute [75]. [b] Value from the Ioffe Institute [76]. [c] Computed as $(5320 - 1560 \times 0.92)$ from the Ioffe Institute [77]. [d] Value from the Ioffe Institute [78]. [e] Approximate isotropic Young's modulus from Cole et al. [74]. This is an approximation because the GaAs is anisotropic.

Property	GaAs	$Al_{0.92}Ga_{0.08}As$
Density ρ $(\frac{\text{kg}}{\text{m}^3})$	5320 [a]	3890 [c]
Poisson's ratio σ	0.31 [a]	0.32 [c]
Specific heat C_ν $(\frac{\text{J}}{\text{kgK}})$	330 [b]	440 [d]
Thermal conductivity κ $(\frac{\text{W}}{\text{mK}})$	55 [b]	70 [d]
Linear expansion coefficient α (K^{-1})	5.73×10^{-6} [b]	5.2×10^{-6} [d]
Young's modulus E_y (GPa)	100 [e]	100 [e]

ments. This shift compensates for the thermorefractive effects when the structure is cooled [66]. More details of the fabrication process are found in [66, 67, 68, 69, 70, 71, 72, 73] and the supplemental material of [46]. The mechanical and thermal properties of GaAs and $Al_{0.92}Ga_{0.08}As$ are listed in Table 3.1.

Previous generations of the cantilever microresonators were not optimized for measuring radiation pressure noise. To improve the performance for the new generation of mirrors, we studied the effects of changing the geometry of the cantilever and mirror pad. During the study, we wanted to reduce the modeled thermal noise to be below the modeled quantum noise. One of the chief ways to reduce the signal-to-noise ratio (SNR) of QRPN to thermal noise (TN) is to reduce the mass of the oscillator. Using Equations 3.5 and 1.38 the SNR of QRPN to TN is

$$SNR \propto \frac{1/m}{1/\sqrt{m}} = \frac{1}{\sqrt{m}}, \tag{3.12}$$

where m is the mass of the microresonator. While reducing the mass increases the SNR, it also increases the fundamental frequency of the microresonator. This factors in to the constraint of wanting the fundamental resonance frequency between 100 Hz and 1 kHz. The reason for having a low frequency microresonator is seen by comparing Equations 3.5 and 1.38, which show that the structural thermal noise has an additional factor of $\omega^{1/2}$ in

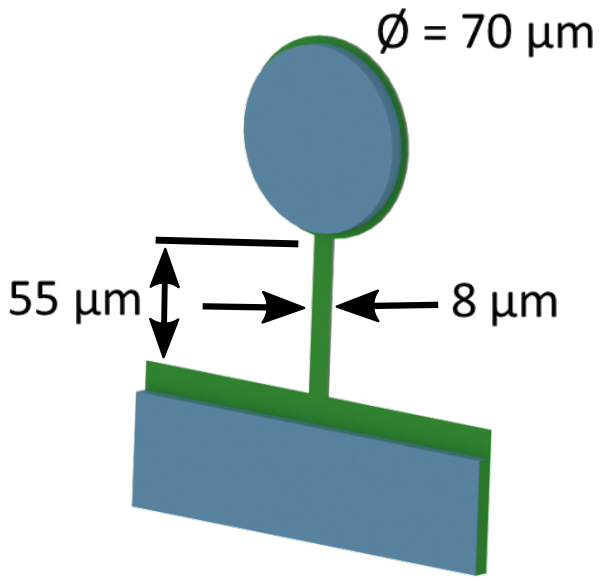

Figure 3.3: Three dimensional CAD model of a cantilever mirror. The cantilever has a length of 55 μm and width of 8 μm, and the mirror pad has a diameter of 70 μm. The green layer corresponds to GaAs, and the blue layer signifies alternating layers of AlGaAs and GaAs.

the denominator as compared to QRPN. This difference in frequency dependence allows the SNR of QRPN to structural thermal noise to grow as $\omega^{1/2}$. A further constraint was to avoid having higher order modes between 10 kHz and 200 kHz to allow for a cleaner measurement band. In the figures shown below, the cantilever and mirror dimensions are listed as: cantilever width, cantilever length (from the point at which the cantilever is attached to the chip edge to the edge of the mirror pad), and mirror radius. An example of a cantilever mirror is shown in Figure 3.3.

Thickness: Figure 3.4 shows the effect of varying the thickness of the cantilever. Thinner cantilevers have less mass and therefore increase the SNR of QRPN to TN as described by Equation 3.12. In addition, thinner cantilevers also have fewer higher order modes between 10 kHz and 300 kHz than thick cantilevers do.

Transmissivity: The transmissivity of the mirror can be altered by changing the number of GaAs/AlGaAs layer pairs. Decreasing the transmissivity of the mirror will increase the

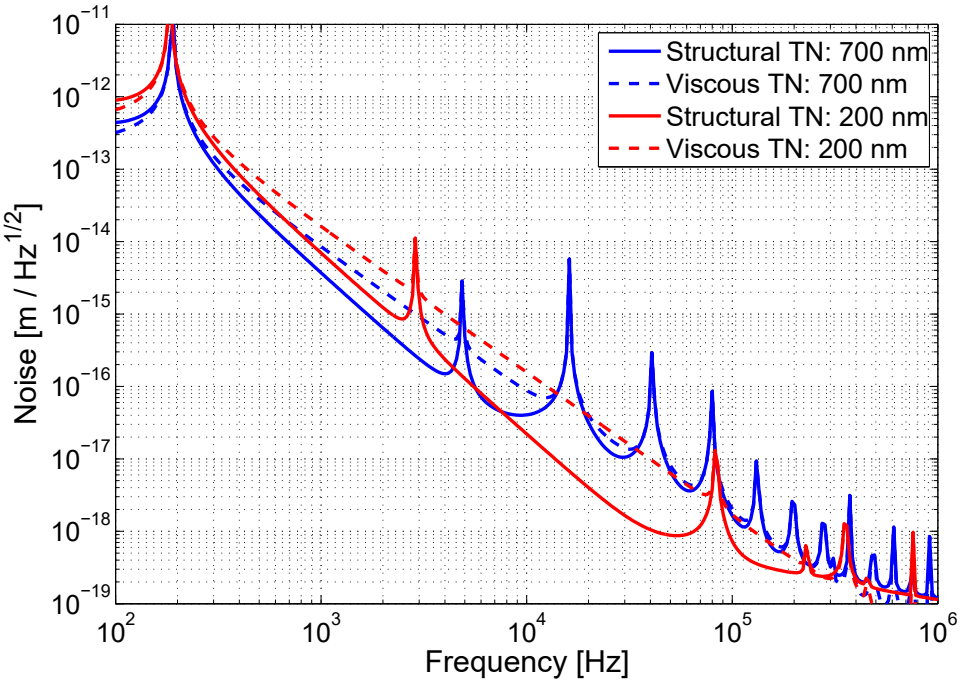

Figure 3.4: Comparison of thermal noise for cantilever mirrors with a cantilever thickness of 200 nm and 700 nm. Model parameters are 250 mW circulating power for a 50 ppm transmission macroscopic mirror and a 350 ppm transmission cantilever mirror.

finesse[1] of the cavity and allow for more power to circulate inside the cavity. This will in turn create a larger QRPN signal. A decrease in transmissivity, however, comes at the expense of increasing the thickness and therefore mass of the cantilever mirror. As seen in Equation 3.12, this reduces the ratio of QRPN to TN. An additional consideration for the transmissivity of the cantilever mirror is the plan for injecting squeezed light into the cavity to reduce QRPN. While taking the low transmissivity of the macroscopic cavity mirror (50 ppm or parts per million), a cantilever with a very low transmissivity will cause inefficient coupling of squeezed light into the cavity and degrade the squeezed light's effect.

Length: Figure 3.5 shows the effect of varying the length of the cantilever. The benefit of using a long cantilever is having a lower fundamental mode resonance frequency. A low frequency fundamental mode allows the structural thermal noise model to start falling off as $f^{-1/2}$ with respect to the QRPN at a lower frequency. On the other hand, longer

[1]The finesse of a Fabry-Perot cavity is given by $\mathcal{F} = \frac{\pi(R_1R_2)^{1/4}}{1-\sqrt{R_1R_2}}$ for mirrors with reflectivity R_1 and R_2.

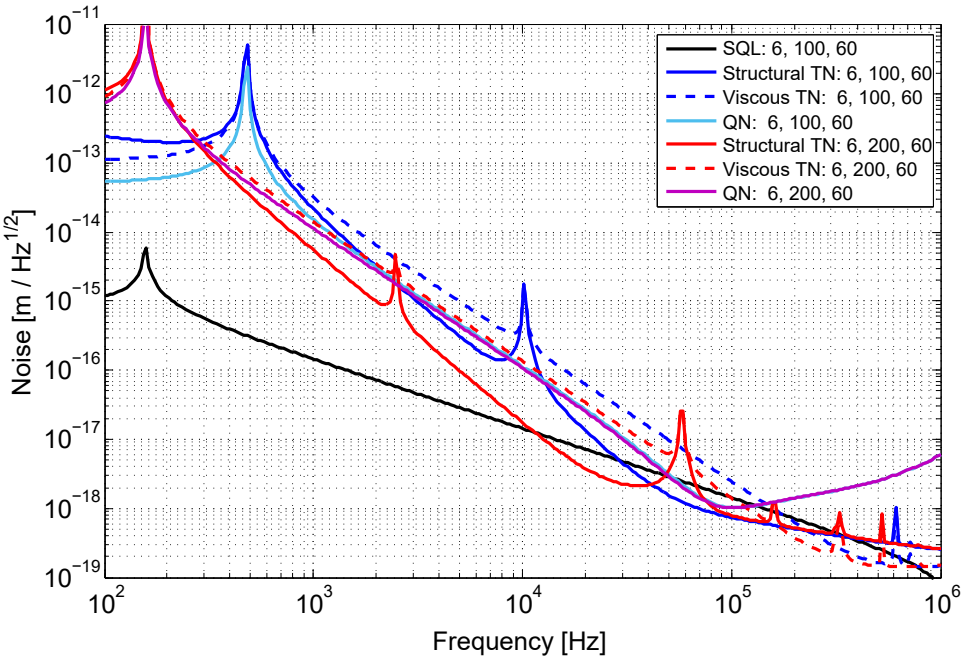

Figure 3.5: Comparison of thermal and quantum noise models for two cantilevers of different lengths. The model was done with a circulating power of 250 mW at a detuning of 0.5 linewidths and a temperature of 9 K.

cantilevers have more higher order modes below 200 kHz.

Width: Figure 3.6 shows the effect of varying the width of the cantilever. Decreasing the width of cantilevers lowers the frequency of the fundamental mode at the expense of having lower frequency higher order modes. The shift of the higher order modes to lower frequencies is not as significant as the shift caused by changing the length of the cantilever. Cantilevers with a smaller width have slightly better noise performance but are also more fragile and likely to break during shipment and installation. For this reason, we have included some optimistic designs with thin cantilevers but have also included some wider cantilevers for safety.

Mirror size: Figure 3.7 shows the effect of varying the radius of the mirror pad. Decreasing the radius of the mirror pad reduces the mass of the mirror, and therefore increases the signal-to-noise ratio of the QRPN to TN as shown in 3.12. This benefit comes at the expense of smaller mirrors having more higher order modes in the 100 kHz - 500 kHz region. Having higher order modes between 100 kHz and 500 kHz does not strongly affect

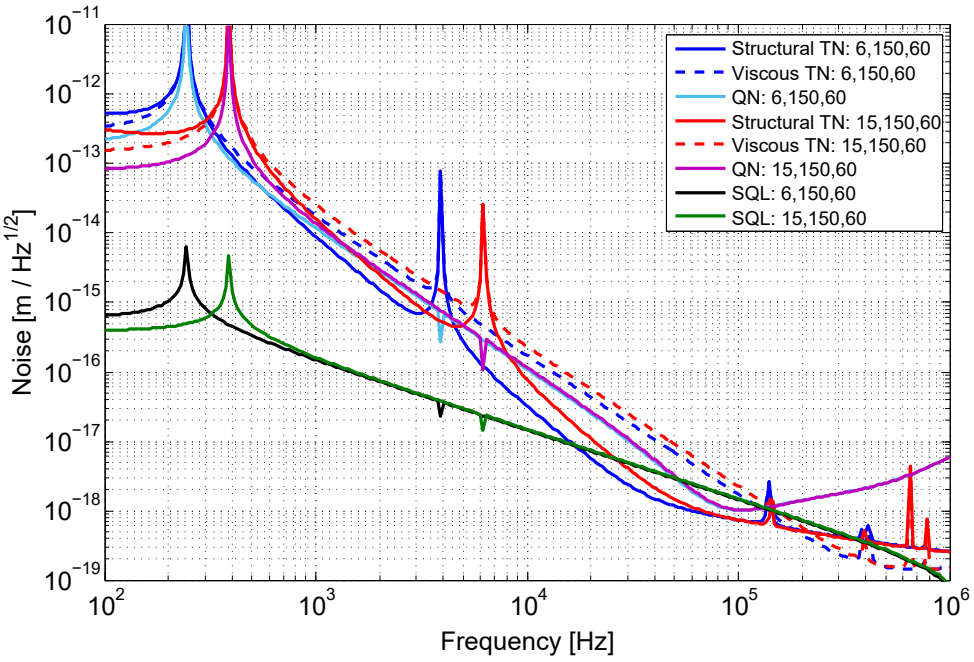

Figure 3.6: Comparison of thermal and quantum noise models for two cantilevers of different width.

the mirror's performance for measuring QRPN below 100 kHz but does impact future experiments aiming for sub-SQL sensitivity between 100 kHz and 200 kHz. Results from previous experiments have shown that the thermoelastic damping of the drumhead mode of the mirror pad might have an effect on the thermal noise spectrum at frequencies well below the drumhead mode's resonance frequency ($\sim 1 - 10$ MHz). The effect of the thermoelastic damping of the drumhead mode can be reduced by decreasing the mirror size so that l_{drumhead}, which is the radius of the mirror, is reduced and ω_{drumhead} is increased. In order to further investigate the thermoelastic damping of the drumhead mode, we intentionally included several mirrors with large radii (up to 200 μm) to decrease ω_{drumhead} and make it more accessible for study.

Nontraditional designs: Figure 3.8 shows a noise budget for a mirror that is suspended by two cantilevers on opposite sides of the mirror. Adding a second cantilever can reduce the probability of the cantilever mirror breaking during shipment and installation, but this design has too many higher order modes between 10 and 200 kHz to be useful.

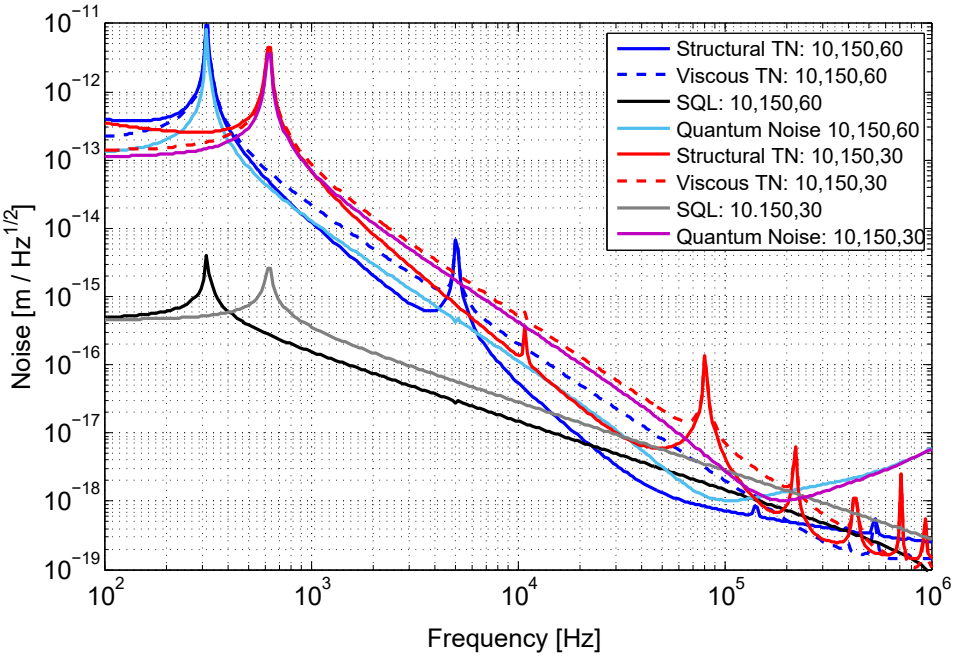

Figure 3.7: Comparison of thermal and quantum noise models for two cantilevers mirrors with different mirror radius.

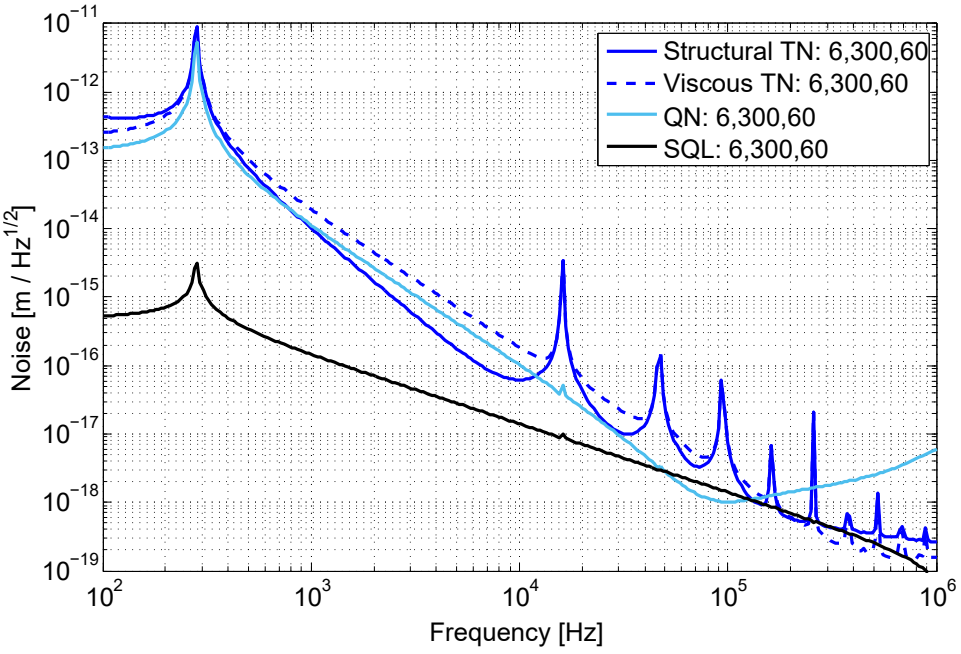

Figure 3.8: Thermal and quantum noise models for a mirror that has a cantilever structure attached to opposite sides.

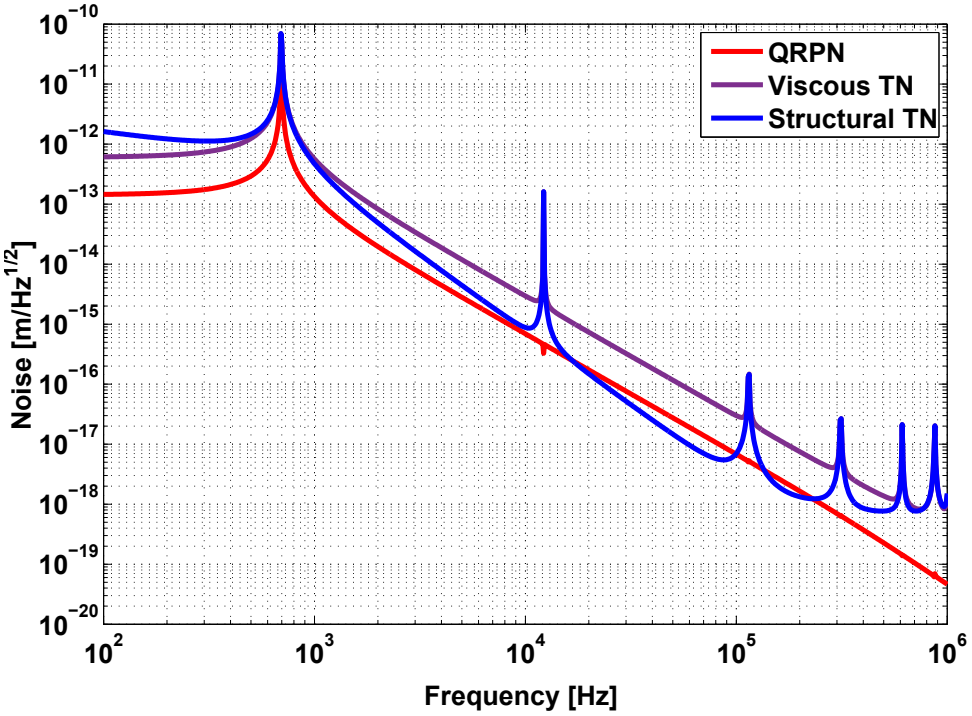

Figure 3.9: Thermal and quantum noise for a 100 μm long and 5 μm wide cantilever with a mirror of radius 25 μm. This is an example of a cantilever whose modeled structural thermal noise lies below the modeled QRPN.

Examples of good cantilevers: Figure 3.9 shows an example of one of the best designs. This design meets the requirements of having a low frequency fundamental resonance, few higher order modes between 10 kHz and 100 kHz, and a modeled structural thermal noise that lies below the modeled QRPN.

Figure 3.10 shows a CAD model of the final chip design, and Figure 3.11 is a photograph of the chip that is used in Chapters 6 and 7. For scale, the chip is a 7 mm by 7 mm square and contains six rows and two columns full of cantilever mirrors. The geometries of the individual cantilevers vary. The radius of the mirror pad is on the order of 20-60 μm with a few having a radius of up to 200 μm. The width and length of the cantilever structure that supports the mirror pad is generally in the range of 5-20 μm and 20-250 μm. The exact dimensions of the cantilever and mirror pad determine the resonant frequency of the fundamental mechanical mode and higher order mechanical modes. Table 3.2 show a representative sample of the cantilever geometries and resonances. The rest of the chip is

Table 3.2: New cantilever mirrors. This table shows a representative sample of the new cantilever mirrors.

Length (μm)	Width (μm)	Mirror Radius (μm)	Mass (ng)	Fundamental Freq. (Hz)
20	60	10	200	998
40	60	6	200	476
50	60	9	200	495
200	60	12	200	150
250	60	15	200	131
60	40	6	100	671
80	40	10	100	656
170	40	6	100	219
170	40	9	100	268
200	40	9	100	220
250	40	9	100	166
250	40	9	100	157
250	30	6	60	189
250	30	10	60	246
80	25	5	40	904
100	25	5	40	696
130	25	6	40	553
250	25	6	40	117

filled with cantilevers that have slightly varied dimensions to add redundancy for the possibility of some of the cantilevers breaking during shipment and operation. The dimensions are varied to avoid cross talk between cantilevers with identical mode structures.

Compared to the previous generations of cantilever mirrors, the newly designed cantilever mirrors have a thinner cantilever (222 μm vs 358 μm). The new design also has a thinner mirror pad (4.5 μm vs 6 μm) as a result of having fewer AlGaAs/GaAs paired layers (23 vs 36) for a larger transmission (250 ppm vs 10 ppm). The thinner cantilever and thinner mirror pad result in the newly designed cantilever mirrors having a smaller mass than the previous generation ($\sim$ 10 ng vs $\sim$ 100 ng). This reduction in mass significantly increases the SNR of QRPN to TN.

The layer structure of the newly designed cantilever is shown in Figure 3.12. The cantilever structure is made soley from the bottom 221.7 nm GaAs layer while the mirror contains the 221.7 nm GaAs layer and all of the layers above it. The multilayer structure

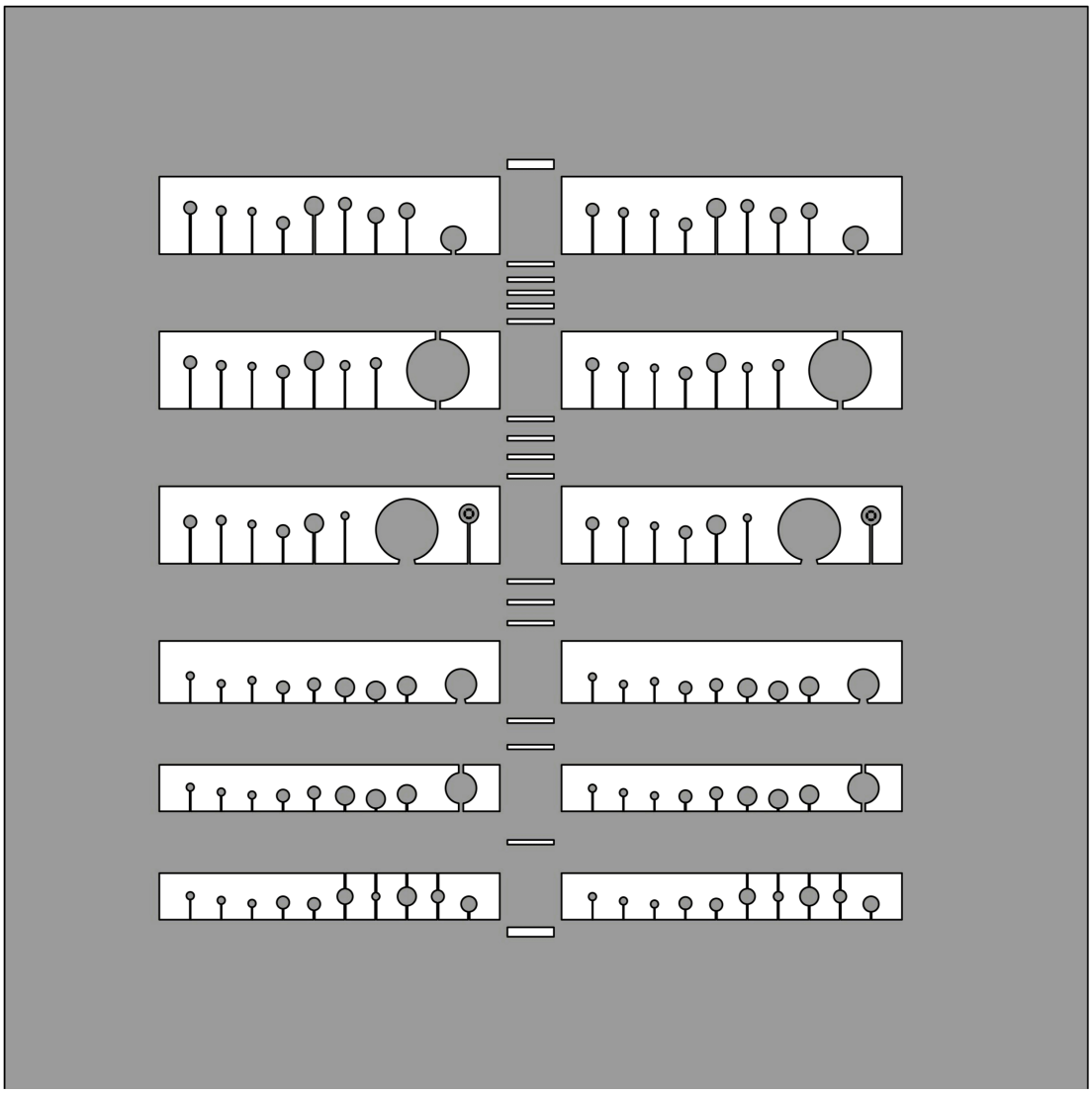

Figure 3.10: CAD model of the new chip created in Autodesk Inventor [79]. The chip includes variations on cantilever and mirror geometries.

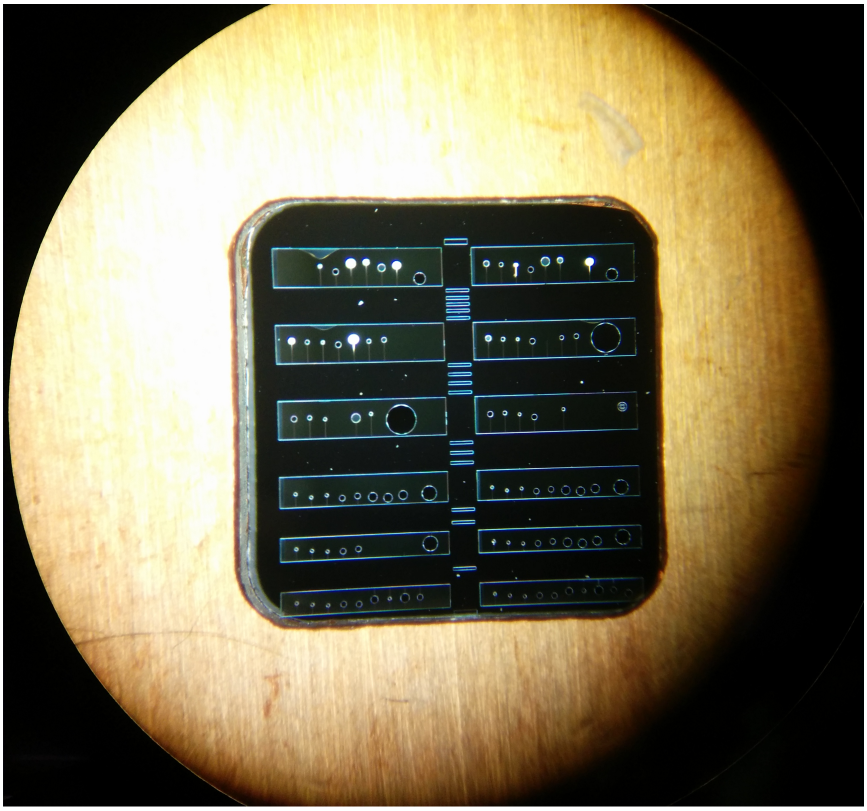

Figure 3.11: Photograph of a microfabricated single-crystal cantilever array manufactured by P. Heu, D. Follman, and G. D. Cole of Crystalline Mirror Solutions LLC, Santa Barbara, CA. The chip in the photograph has the same orientation of the model in Figure 3.10. The cantilever mirrors that are missing in the photograph were broken during fabrication, shipment, or installation.

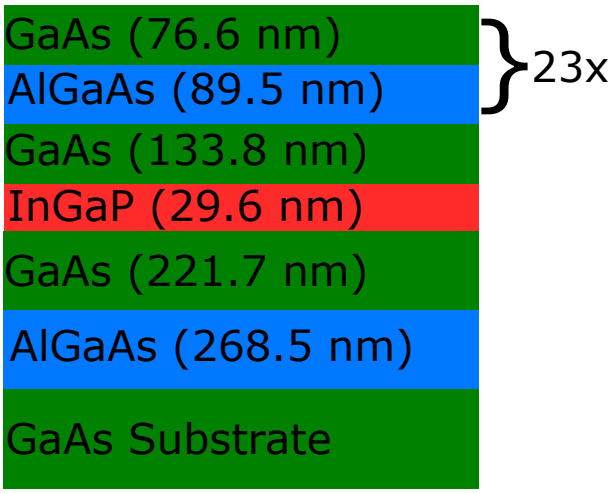

Figure 3.12: Cross sectional schematic of the epitaxial multilayer. The multilayer structure is composed of (from bottom up) a semi-insulating GaAs substrate, a $Al_{0.92}Ga_{0.08}As$ backside etch stop layer, a GaAs structural support layer, a lattice matched InGaP etch stop layer, a GaAs layer, and a 23-period 1064 GaAs/$Al_{0.92}Ga_{0.08}As$ Bragg mirror.

is designed to have a transmission of 250 ppm for a laser wavelength of 1064 nm.

3.5 Cantilever mirror measurements

Based on the experience with previous generations of cantilever mirrors, we believed that the Q should scale roughly with the thickness of the cantilever. Thus, we expected the newly designed cantilever mirrors to have a slightly lower Q than the previous design because of their reduced thickness. We wanted to test this theory, however, because the thermal and quantum noise calculations described in the next sections require an accurate measurement of the Q.

We had previously measured the Q of the previous generation of cantilevers using an optical lever. To measure the Q, we would excite the cantilever mirror by simply tapping on the vacuum chamber that housed it. The optical lever beam reflected off of the cantilever mirror and was detected on a quadrant photodetector (QPD). This technique, however, only allowed us to measure the Q of the fundamental mode because the amplitude of the fundamental mode is much larger than the higher order mechanical modes.

We built a Michelson interferometer to test the Q of the newly designed cantilever mirrors. A schematic of the Michelson interferometer is shown in Figure 3.13. The Michel-

son interferometer was built in the summer of 2017 as part of a summer project for an undergraduate student. The cantilever chip is housed in a vacuum tank and serves as one of the end mirrors of the Michelson interferometer. The vacuum tank is on an x, y, z translation stage so that a single cantilever mirror can be aligned to the incoming laser beam. A piezoelectric transducer (PZT) is attached to the back of the cantilever chip and is used to selectively excite the mechanical modes of the cantilever mirror by changing the voltage on the PZT. This allows us to measure the Qs of the fundamental, yaw, pitch, and other higher order modes individually. A portion of the results is shown below in the Table 3.3. The results shown in Table 3.3 are for the cantilever chip that would eventually be used in the quantum radiation pressure experiment described in Chapter 6 and the experiments in Chapter 7. The frequency and Q for some of the modes were difficult to determine because there were multiple resonance peaks in the frequency band in which the mode was predicted to be. We were able to find three frequencies (5358 Hz, 12690 Hz, and 13980 Hz) that were common across multiple measurements and are most likely resonances of the piezo or structure that holds the chip. In order to perform the measurements, the interferometer is locked by detecting the light at the output port of the interferometer and feeding back to a PZT that is mounted to the other end mirror. The camera and photodetector in transmission of the cantilever chip are used for alignment purposes. The vacuum chamber that houses the cantilever chip is compatible with a cryostat. In the future, we plan to measure the Qs as a function of temperature.

3.6 Cryogenic design

As described in the previous sections, thermal noise usually masks the effect of the quantum radiation pressure noise at room temperature. One way to reduce the thermal noise and bring it below the radiation pressure noise is to cool the cantilever mirrors to cryogenic temperatures. Since the thermal noise scales with temperature as $\sqrt{T}$, as seen in Equations 3.4 and 3.5, lowering the temperature from room temperature to 4 K, the temperature of liquid He^4, would reduce the thermal noise by a factor of approximately 10.

Table 3.3: Measured frequencies and quality factors (Q) of the fundamental modes using the Michelson interferometer. The rows are numbered 1-6 starting from the bottom row in model in Figure 3.10. The column refers to left (L) and right (R) side of the central strip. The number is which number cantilever in the row staring from the left side of the chip for the left column and the middle of the chip for the right column. The fundamental mode (F), yaw mode (Y), or pitch mode (P) were all attempted to be measured. Some measurements contained more than one peak and are denoted by * for two peaks, @ for three peaks, and ˆfor four peaks. The blank spaces were either not measured, or the frequency and Q were not able to be determined from the measurement.

Row	**Column**	**Number**	**F (Hz)**	**F Q**	**Y (Hz)**	**Y Q**	**P(Hz)**	**P Q**
1	L	1	482	2000	4374	2000		
1	L	2	667	5000				
1	L	3	875	8000			16363	4000
1	L	8	1113	4000				
1	R	1	516	500	4518	3000		
1	R	2	708	6000	5062	5000	13900	6000
1	R	4	636	5000	2820	12000		
1	R	5	994	5000				
2	L	1	622	8000	5778	4000	13200 *	7000
2	L	2	772	4000			15275	10000
2	L	4	831	6000	1114	1000	12650	1000
2	L	5	623	4000				
2	R	2	787	10000				
2	R	4	876	11000	3694	1000	15230	8000
3	L	2	865	11000	3481	4000	17145	5000
3	L	5	704	4000	3481 @	6000	11730	5000
3	R	2	516		5292	8000		
3	R	3	657	500	5493	4000	12222 ˆ	13000
3	R	5	746	14000	3584	5000		
5	R	7			2746	1500		
6	L	1			2005	9000	4705	13000
6	R	4			2255	3000	5868	6000

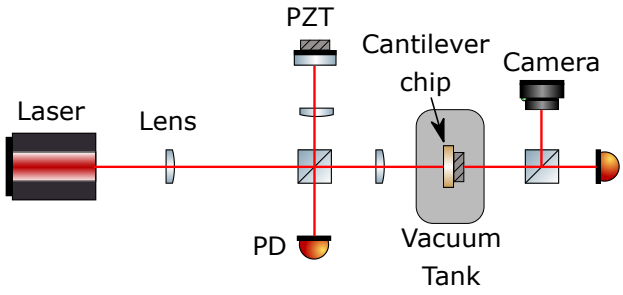

Figure 3.13: Schematic of the Michelson interferometer used to measure the quality factors of the new generation of cantilever mirrors. The cantilever mirror serves as one of the end mirrors of the Michelson. A piezoelectric transducer (PZT) is attached to the back of the cantilever chip and is used to selectively excite mechanical modes of the cantilever mirror.

In order to use liquid helium to cryogenically cool the cantilever mirrors, a cryogenic connection must be designed in order to connect the cantilever mirror to the liquid helium and extract heat from the cantilever mirror. The requirements for the cryogenic design are:

1. The cantilever mirrors must be in thermal contact with the cryostat.
2. The material connecting the cantilever mirrors to the cryostat must have a high thermal conductivity.
3. The cantilever mirrors must maintain optical access for the laser beam path.
4. The cryogenic connection between the cantilever mirrors and the cryostat must be flexible to allow for cavity alignment.
5. The cantilever mirrors must be housed in a radiation shield to reduce the heat load and prevent any particles in the vacuum chamber from freezing to the cantilever mirrors.

A chip mount was fabricated out of oxygen-free high thermal conductivity (OFHC) copper to house the fragile chip that contains the cantilever mirrors. A schematic of the chip mount is shown in Figure 3.14. OFHC copper is a high conductivity copper alloy that has been electrolytically refined to reduce the level of oxygen to .001% or below. One of the beneficial properties of OFHC copper is its high thermal conductivity of 390 $^{\mathrm{W}}/(\mathrm{m} \times \mathrm{K})$ [80]. OFHC copper is used instead of the elemental copper because of its high purity and low volatility under high vacuum. Elemental copper contains a larger amount of oxygen

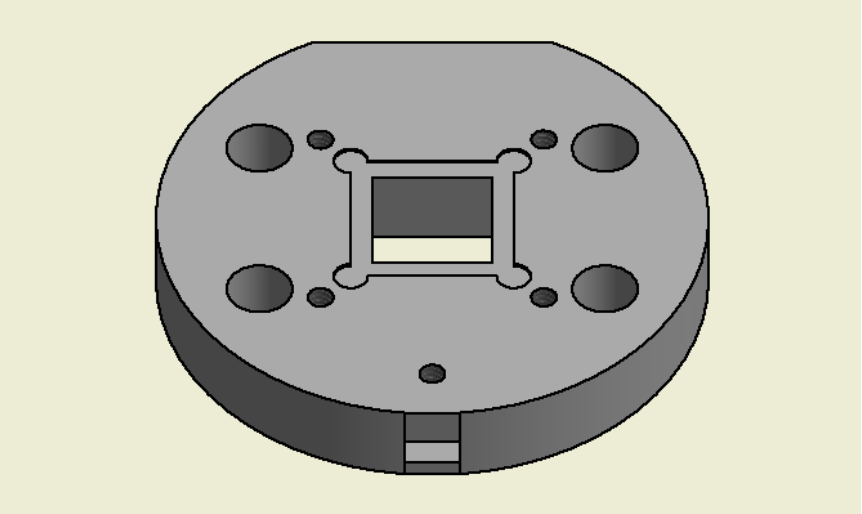

Figure 3.14: 3D CAD rendering of the chip mount made out of OFHC copper. The chip sits in the large central window and is clamped in place by a second piece of OFHC copper (not shown here). The two copper pieces are screwed together to maintain sufficient pressure to hold the chip in place. The large central window allows for optical access from both sides of the chip. The four large through holes are used to integrate the chip holder with the rest of the cryogenic setup, which is described below. The chip holder also contains a slot (shown at the bottom center of the image) to mount a temperature sensor to monitor the temperature of the chip mount and chip when it is cooled.

than OFHC copper and is known to outgas, or release a trapped gas, at high vacuum.

The chip mount is in thermal contact with the cryostat via flexible heat links. The heat links are made out of thin OFHC copper strips to have a large thermal conductivity and coated in gold to prevent oxidization.

The chip mount and chip are housed in a radiation shield to prevent blackbody radiation from the surrounding vacuum tank from being absorbed by the chip mount and increasing its temperature. The radiation shield is made out of OFHC copper and wrapped in aluminized mylar. Aluminized mylar has a very low emissivity of 0.044 [81], which makes it a good reflector of blackbody radiation. The aluminized mylar layer on the radiation shield reduces the amount of blackbody radiation from the surrounding vacuum tank that the radiation shield absorbs and therefore keeps the radiation shield at a lower temperature. The radiation shield is connected to an intermediate stage of the cryostat via a separate set of flexible OFHC copper heat links.

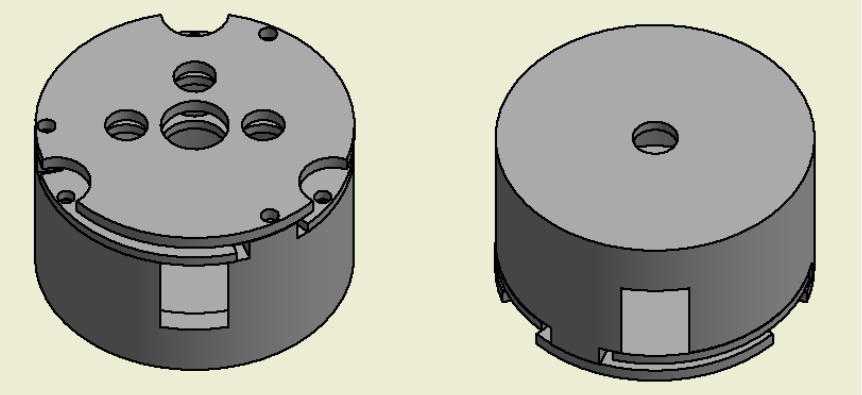

Figure 3.15: 3D CAD rendering of the radiation shield made out of OFHC copper. The radiation shield surrounds the chip mount and chip to prevent blackbody radiation from heating the chip. The laser beam is able to pass through the central hole on both sides of the radiation shield. The flexible heat links that connect the chip mount to the cryostat pass through the slit shown on the bottom of the image on the left.

To cool the cantilever mirror chip to cryogenic temperatures, we designed a cryogenic setup that would be compatible with the optical setup of our optomechanical Fabry-Perot cavity. As stated in the list of requirements above, one constraint that our optical setup imposes is the need to align the cantilever mirror chip to form a resonant cavity with one of the mirrors. In addition, we need to be able to move the chip to use other mirrors on the chip. We use Agilis translational and rotational stages from Newport Corporation to control the position of the chip [82, 83]. The Agilis mounts must operate at room temperature, so we had to design a chip mount that would allow the chip to be at a cryogenic temperature while the Agilis mounts were at room temperature. To achieve this requirement, we needed a material with very low thermal conductivity to prevent heat from the room temperature Agilis mount flowing to the cold chip.

The first design used hollow Kapton rods to connect the cold chip to the room temperature Agilis mount. After building a test setup, we found that the Kapton rods were not strong enough to support the weight of the copper mount that holds the chip. The next material we tried was G-10, which is an epoxy resin. G-10 has a very low thermal conductivity of 0.6 $^{\mathrm{W}}/_{(\mathrm{m}\times\mathrm{K})}$ at room temperature and about 0.1 $^{\mathrm{W}}/_{(\mathrm{m}\times\mathrm{K})}$ at 4 K, making it an ideal thermal insulator [84]. In addition, G-10 is more rigid than Kapton, so it can

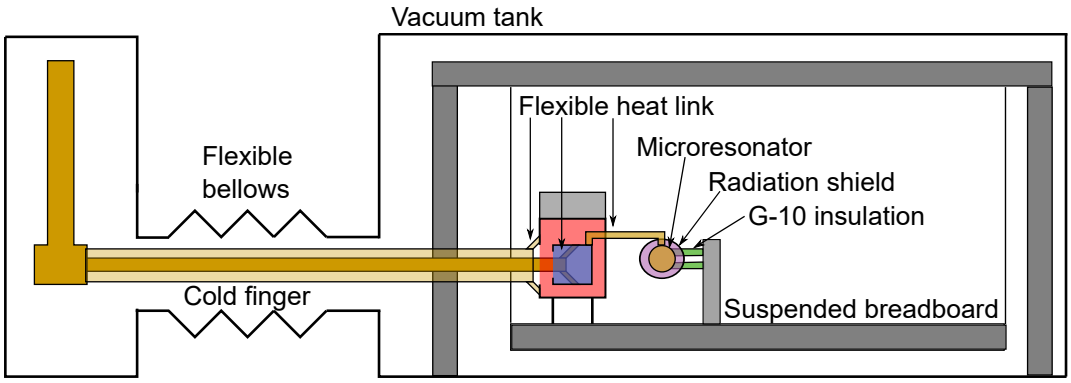

Figure 3.16: Schematic of the cryogenic setup. The cryostat's cold finger enters the vacuum tank through a flexible bellows that shield the vacuum tank from vibrations from the cryostat. The in-vacuum optical breadboard is suspended from steel wires to further reduce vibrations. The cold finger is attached to stage one (red) and stage two (blue) of the nested structure via flexible copper heat links. Stage two of the nested structure is attached to the cantilever chip by another set of flexible heat links. Stage one is attached to the radiation shield (purple) via flexible copper braids. The cantilever chip and radiation shield are thermally isolated from the room temperature Agilis mirror mount by three hollow G-10 rods.

support the weight of the chip mount without bending. To further reduce the heat flow between the cryogenic chip mount and the room temperature Agilis stages, we used hollow G-10 rods to minimize the amount of material that could transport heat from the cold chip to the room temperature mount. The G-10 rods fit in the four large through holes in the chip mount, shown in Figure 3.14, and in a similar set of holes in an aluminum piece that is secured in the Agilis mount.

A schematic of the cryogenic setup is shown in Figure 3.16. The cryostat is a custom Montana Instruments cryostation. The cryostation features a cryogen-free, closed-cycle system that uses a variable flow helium compressor to recycle the consumed helium. The cryo-cooler is a Gifford-McMahon style, and the cryostation has a base temperature of about 4 K and a temperature stability of less than 20 mK. The cryostation includes flexible bellows and flexible heat links to provide vibration isolation for the cold sample. The isolation reduces the vibrations to less than 10 nm during operation.

After designing the cryogenic setup, we placed the chip holder inside of the radiation shield and turned the cryostat on to test its performance. Figure 3.17 shows a long-term

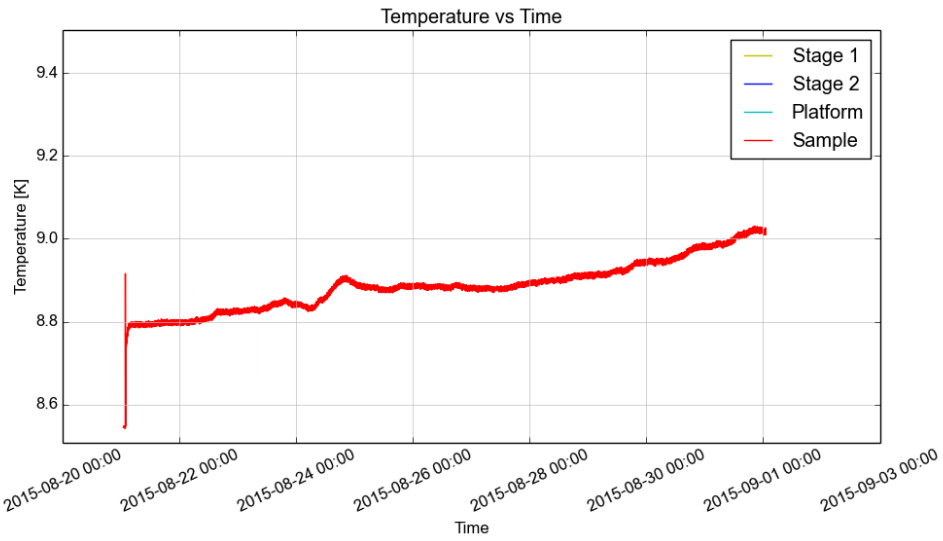

Figure 3.17: Cryogenic cooldown test. Only the sample temperature, which is the temperature of the copper piece that holds the cantilever chip, is plotted. During the test, the sample temperature rose by 0.2 K over the course of 11 days or 0.018 K per day.

test of the cryogenic performance. The sample was cooled down to 8.8 K and monitored for 11 days. During that time, the sample temperature rose by 0.2 K or 0.018 K per day. By reducing the temperature of the cantilever mirrors from room temperature to 9 K, the thermal noise of the cantilevers would be reduced by a factor of almost six. This test proved both the performance and long-term stability of the cryogenic setup.

3.7 Seismic vibration isolation

The optical breadboard inside the vacuum tank is suspended to isolate the optomechanical cavity from external seismic vibrations. The power spectrum of the earth's vibrations is a steeply falling function of frequency $x(f) = 10^{-9}\ {}^{\mathrm{m}}/_{\mathrm{Hz}^{1/2}}({}^{10\mathrm{Hz}}/_{\mathrm{f}})^2$ at a relatively quiet location [85]. Theses seismic vibrations are caused by things ranging from human activity to ocean waves hitting the shoreline. An additional source of vibrations in our experiment is the closed-cycle cryostat. Despite having multiple stages of vibration isolation between the cryostat and the optomechanical cavity, the cavity was unable to maintain lock when the cryostat was turned on.

Both active and passive strategies can be employed to isolate an experiment from the seismic activity. One form of passive isolation is the use of a suspension system. A passive

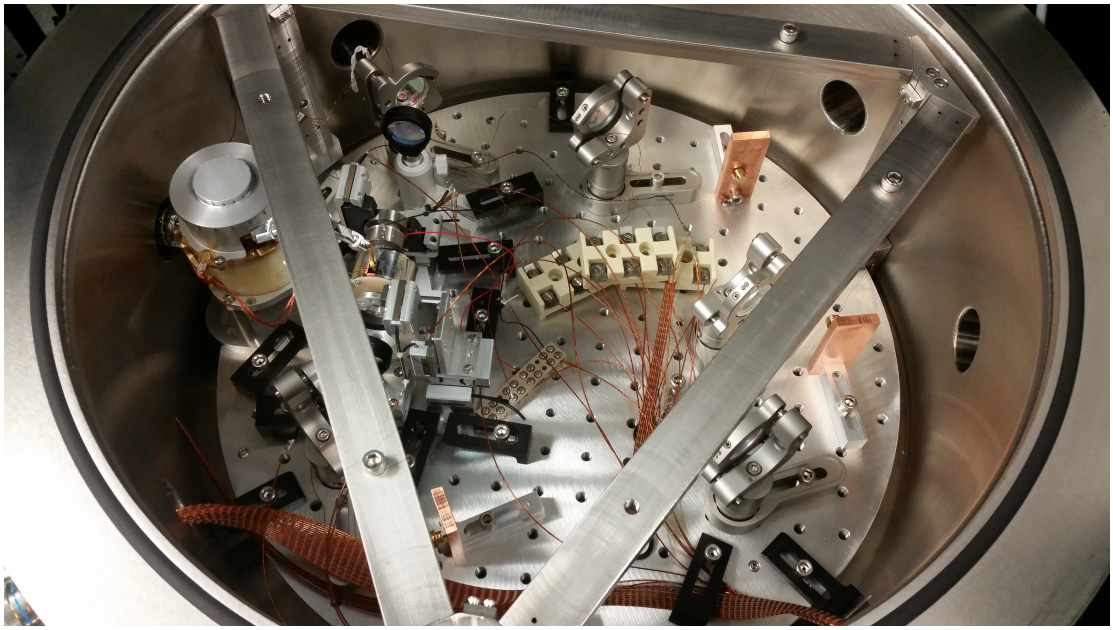

Figure 3.18: Suspended optical breadboard inside the vacuum tank. The optical breadboard is suspended by three wires to isolate the optomechanical cavity from outside vibrations. The entire setup is placed inside a vacuum tank to reduce acoustic coupling and residual gas noise.

suspension with a resonant frequency of f_0 provides an isolation of $(f_0/f)^2$ at frequencies, f, that are large compared to f_0. For the purposes of this thesis, I wanted to design a suspension that would isolate the optomechanical cavity housed in the vacuum tank above roughly 1 kHz. Ideally the design would use a long suspension to decrease the suspension's resonance frequency, but the height of the suspension was constrained to fit within the vacuum tank. As a result, the height of the suspension was limited to about 15 cm. The suspension has several resonance frequencies between 1 Hz and 30 Hz. As a result, seismic vibrations are reduced by a factor of roughly 1,000 at 1 kHz. The suspension was constructed out of vacuum compatible stainless steel and is shown in Figure 3.18.

We installed eddy current dampers to reduce the quality factor, Q, of the mechanical resonances of the suspension and isolate the optomechanical cavity from external vibrations. Eddy current dampers are based on the creation of a motional emf when a conductor moves relative to a magnetic field. The induced emf creates an eddy current in the conductor, as described by Faraday's law of induction. The induced current moves in a direction that

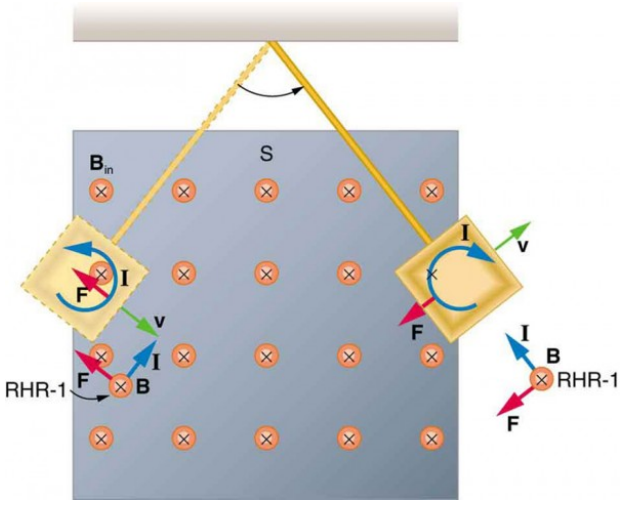

Figure 3.19: Illustration of the induced currents and forces for an eddy current damper [86]. The magnetic flux through the conducting plate changes as the conductor enters and exits the magnetic field. This change in flux produces an eddy current, which in turn, produces a magnetic field that opposes the change in flux. This induced magnetic field produces a force that is in the opposite direction as the motion of the conductor and thus reduces the conductor's velocity.

produces a magnetic field that opposes the change in magnetic flux as described by Lenz's law. An illustration of the induced current and forces produced in the description above is shown in Figure 3.19.

The eddy current dampers are installed in the vacuum tank, as shown in Figure 3.20, with an OFHC copper flag serving as the conductor and a stack of Neodymium magnets providing the magnetic field. The Neodymium magnets are suspended with a wire to provide isolation from seismic vibrations and to avoid feeding seismic vibrations onto the suspended optical breadboard. As shown in Figure 3.21, the magnets were originally not suspended and attached rigidly to the suspended breadboard with the leg of the suspension acting as the conductor.

The results from installing the eddy current dampers with the cryostat off is shown in Figure 3.22 and with the cryostat on in Figure 3.23. Both Figure 3.22 and Figure 3.23 were taken with accelerometers attached to the breadboard and show that the reduction in the amplitude of the vibrations across a wide range of frequencies. Comparing Figure 3.22 and Figure 3.23 shows that the cryostat adds approximately 20 dB of noise at 100

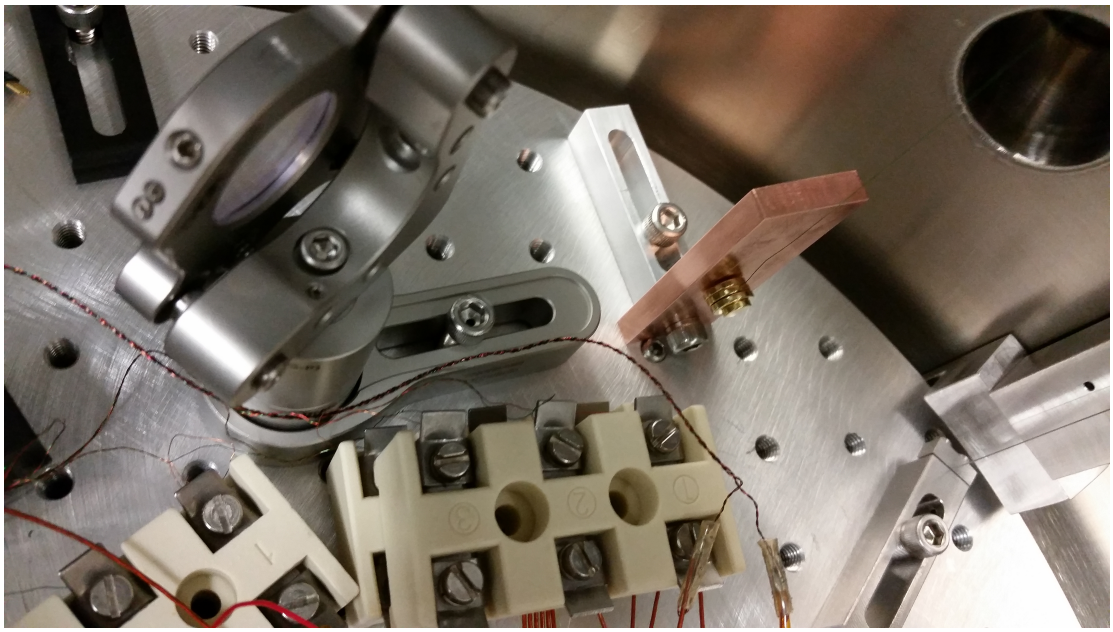

Figure 3.20: Eddy current dampers used to damp suspension resonances. The eddy current dampers consist of a conductor (copper flag) and strong magnet (gold plated discs in front of copper flag). The magnet is also suspended so that it serves as a quiet reference and does not introduce excess vibrations.

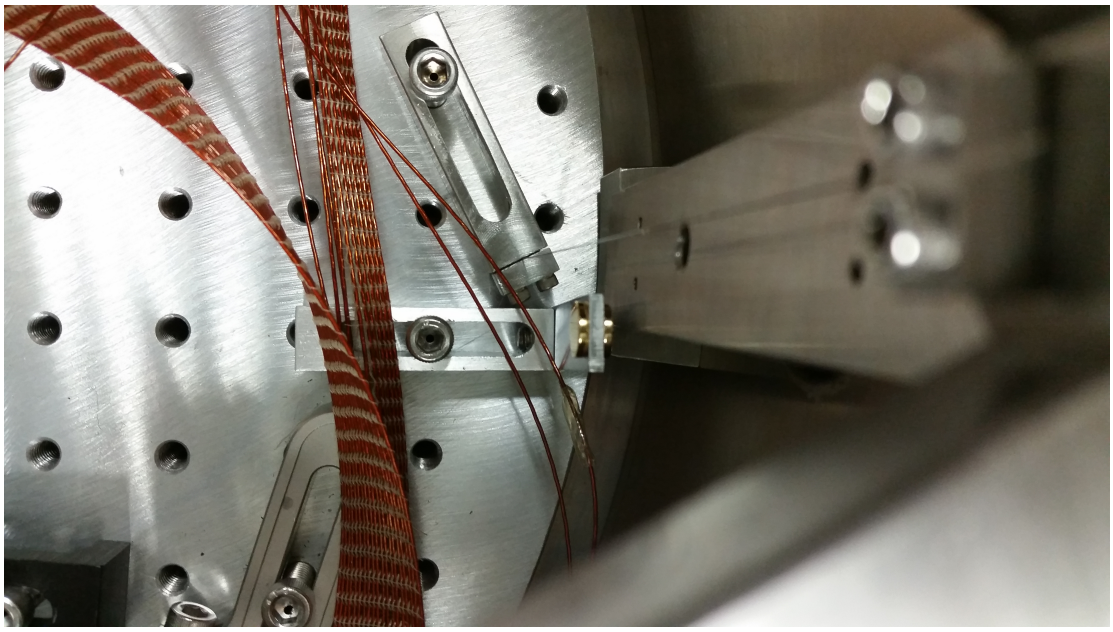

Figure 3.21: Initial eddy current damper setup with a fixed magnet. The eddy current dampers consist of a conductor (the leg of the suspension) and strong magnet. The fixed magnet adds noise to the suspended platform as seen in Figure 3.22.

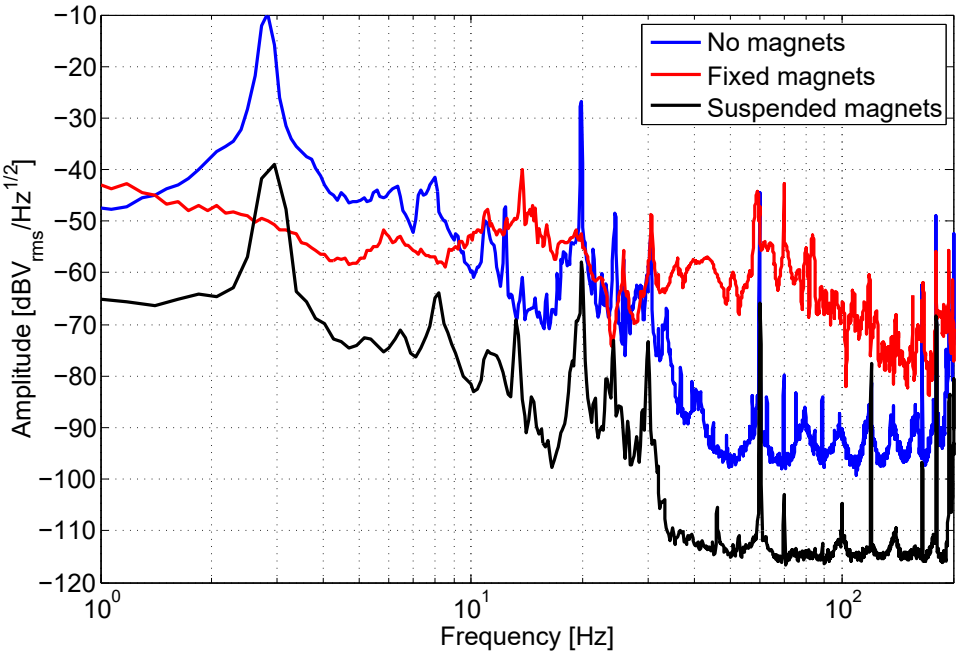

Figure 3.22: Results from adding the eddy current dampers with the cryostat turned off. The eddy current dampers with suspended magnets provide a roughly 50 dB decrease in noise at 100 Hz.

Hz. The cryostat also creates a large forest of peaks between 1 Hz and 10 Hz, which are not present with the cryostat off. Figure 3.22 also demonstrates that using magnets that are rigidly attached to the suspension system and the leg of the suspension system as the conductor creates a short circuit. The motion of the suspension leg, which is not vibration isolated by the suspension system, feeds motion onto the magnet, which is attached to the suspended breadboard. This short circuit allows vibrations to bypass the isolation added by the suspension system.

3.8 Final design

After designing all the components necessary to construct the optomechanical cavity, the cavity was built inside the vacuum tank on the suspended optical breadboard. A picture of the optomechanical cavity is shown in Figure 3.24. The laser light is coupled into the cavity through the cantilever mirror (left of center in the picture) and detected both in reflection and transmission of the cavity. The transmissivity of the cantilever mirrors is 250 ppm to balance the requirements of constructing a high finesse optical cavity with a

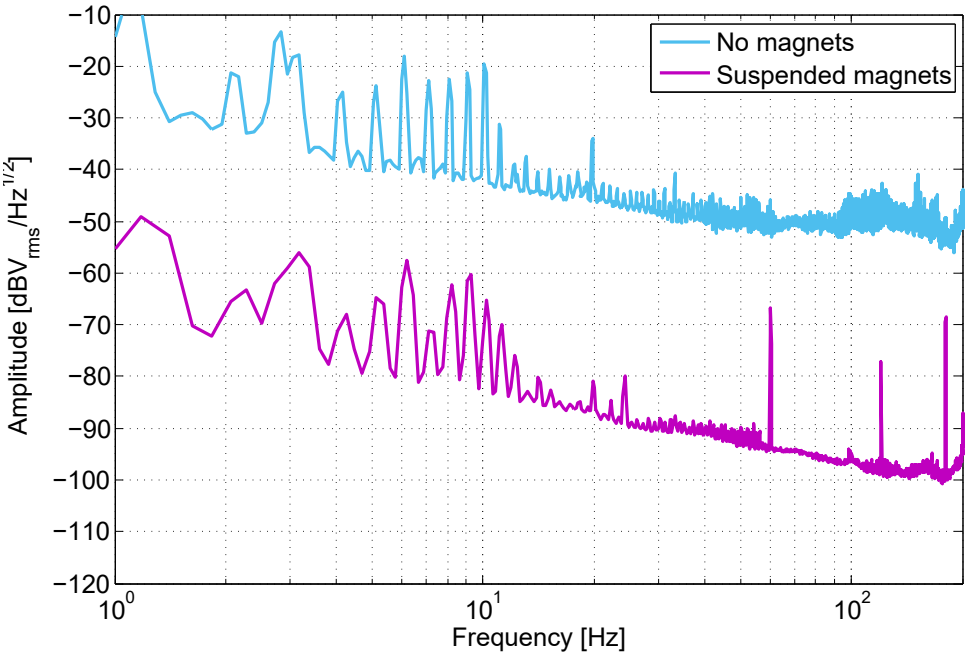

Figure 3.23: Results from adding the eddy current dampers with the cryostat turned on. The broadband noise is increased with the cryostat on relative to when the cryostat is off in Figure 3.22.

low mass cantilever mirror. The 250 ppm transmission also allows for squeezed light to be coupled into the cavity through the cantilever mirror.

After performing the initial alignment of the cavity, we were able to successfully operate the cavity with the cryostation turned on. After the quick test, however, we decided to proceed with continuing the cavity alignment at room temperature to avoid the possibility the cavity becoming misaligned as the cantilever chip and the structure holding it cooled. In the future, we plan to operate with the cryostat on and the mirrors cryogenically cooled, as discussed later in Chapter 8.

The Q of the fundamental, yaw, and pitch modes was remeasured after the chip was installed in the experiment to confirm that the mirrors had not been damaged during the installation. The measurements, shown in Figures 3.25, 3.26, and 3.27 were performed using an optical lever reflected off the cantilever mirror and detected on a QPD.

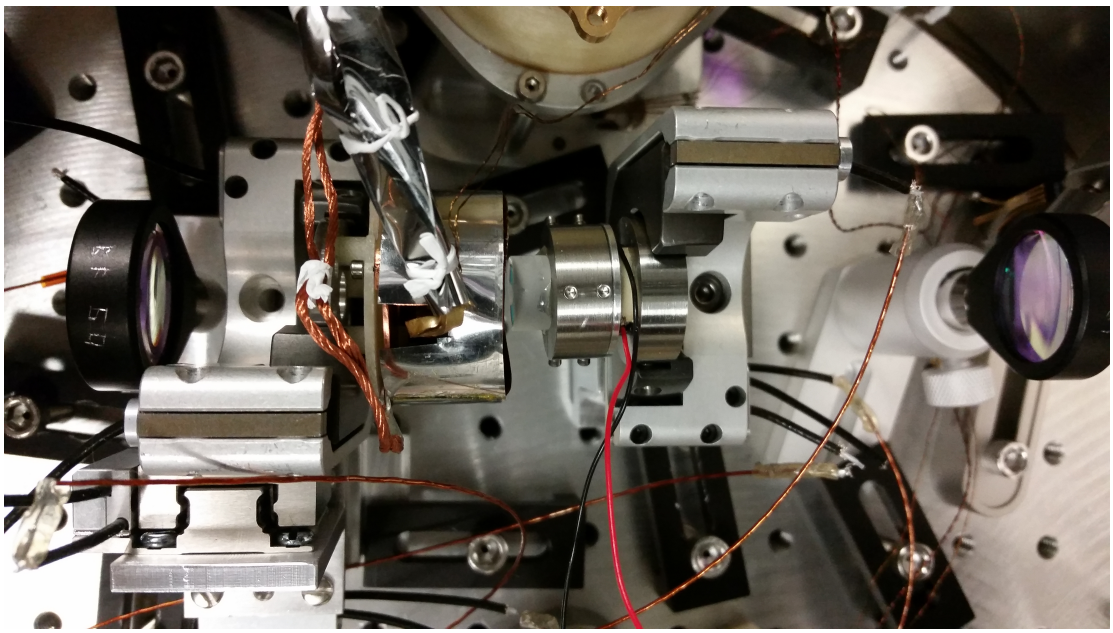

Figure 3.24: The optomechanical cavity consists of a 1-inch radius of curvature output coupler mirror (right) and one of the cantilever mirrors on the chip (left wrapped under aluminized mylar). Lenses on either side of the cavity are used for mode matching the optical beam to match the cavity mode. Both the output coupler and cantilever chip are mounted on motorized Agilis translation stages and mirror mounts, which are used to position the mirrors. The cantilever chip is connected to the cryostat (top) via flexible copper ribbons wrapped in aluminized mylar. A radiation shield wrapped in aluminized mylar surrounds the cantilever chip to block any blackbody radiation from the surrounding vacuum tank and prevents any particles from hitting and sticking to the cantilever chip when it is cold.

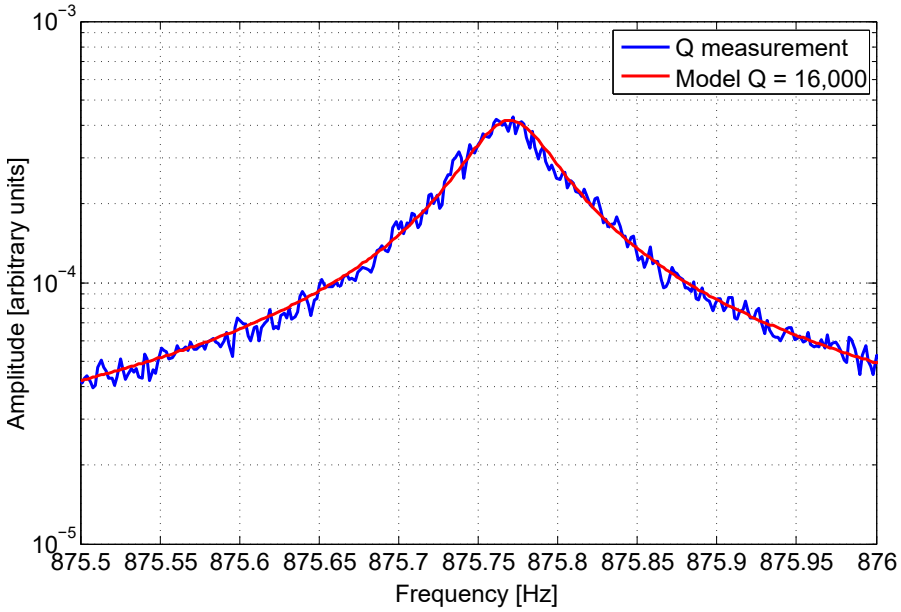

Figure 3.25: Measurement of the Q for the fundamental mode after the chip was installed and after the laser beam was aligned onto the cantilever of interest. The blue trace is the measured trace and the red curve is a model with a Q of 16,000.

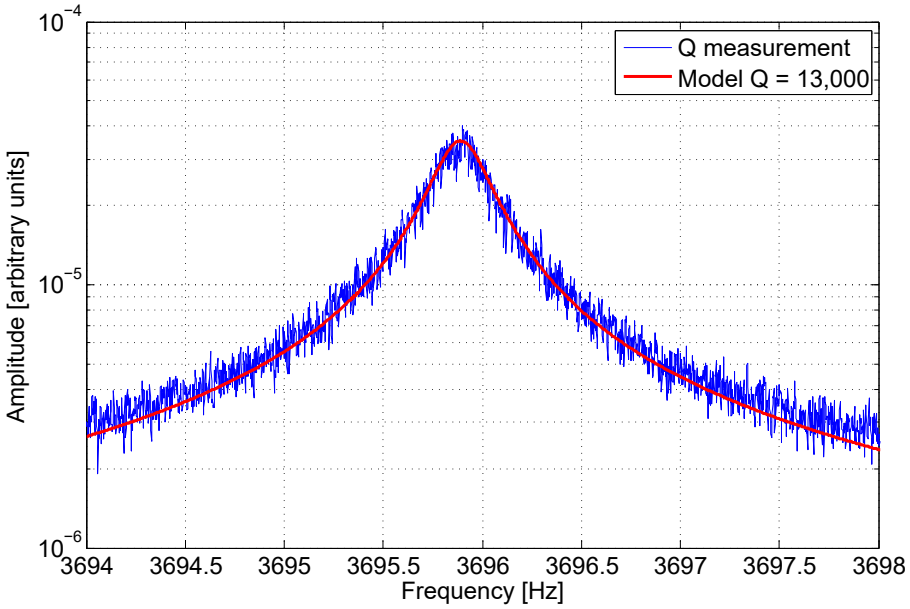

Figure 3.26: Measurement of the Q for the yaw mode after the chip was installed and after the laser beam was aligned onto the cantilever of interest. The blue trace is the measured trace and the red curve is a model with a Q of 13,000.

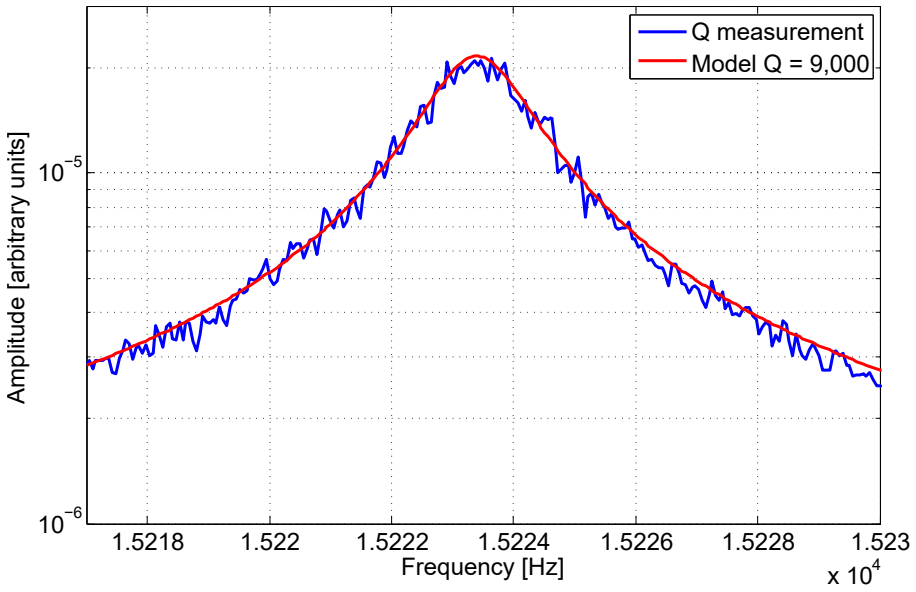

Figure 3.27: Measurement of the Q for the pitch mode after the chip was installed and after the laser beam was aligned onto the cantilever of interest. The blue trace is the measured trace and the red curve is a model with a Q of 9,000.

Chapter 4
Radiation-Pressure-Mediated Control of an Optomechanical Cavity

We describe and demonstrate a method to control a detuned movable-mirror Fabry-Pérot cavity using radiation pressure in the presence of a strong optical spring. At frequencies below the optical spring resonance, self-locking of the cavity is achieved intrinsically by the optomechanical (OM) interaction between the cavity field and the movable end mirror. The OM interaction results in a high rigidity and reduced susceptibility of the mirror to external forces. However, due to a finite delay time in the cavity, this enhanced rigidity is accompanied by an anti-damping force, which destabilizes the cavity. The cavity is stabilized by applying external feedback in a frequency band around the optical spring resonance. The error signal is sensed in the amplitude quadrature of the transmitted beam with a photodetector. An amplitude modulator in the input path to the cavity modulates the light intensity to provide the stabilizing radiation pressure force. This chapter is adapted from [47].

4.1 Introduction

Cavity optomechanics, the interaction between electromagnetic radiation and mechanical motion, provides an ideal platform for measuring mechanical displacements and preparing and detecting mechanical resonators in the quantum regime [87]. In a simple cavity-coupled optomechanical system, the mechanical oscillator is driven by the radiation pressure force exerted by the probing laser field. The fluctuations in the radiation pressure force due to power fluctuations modulate the motion of the mechanical oscillator, effectively changing the length of the cavity and modifying the resonance condition of the cavity. This leads to changes in the optical power circulating inside the cavity, thus cyclically modulating the radiation pressure force exerted on the mechanical oscillator. This feedback results in the optical spring effect.

The optical spring effect was first discussed for Fabry-Perot cavities by Braginsky [88,

89]. Braginsky *et al.* [90], Buonanno and Chen [91], and Harms *et al.* [52] proposed using the optical bar and optical spring to enhance the sensitivity of gravitational wave detectors. Over the past two decades, many experiments have observed the optical spring in a variety of systems [45, 46, 87, 92, 93, 94, 95, 96, 97, 98, 99] and used it to optically cool mechanical resonators [100, 101, 102, 103, 104, 105, 106, 107, 108]. Furthermore, proposals to increase the sensitivity of Michelson-type gravitational wave detectors using the optical spring effect have included adding a signal-recycling cavity [109, 110, 111], using a detuned cavity to amplify the interferometric signal [112], adding a signal-extraction cavity or resonant sideband extraction [113, 114], and dynamically tuning the cavities to follow a gravitational wave chirp signal [115, 116]. Signal-recycling and signal-extraction cavities have been used in the GEO 600 [117] and Advanced LIGO [10] gravitational wave detectors, and are planned to be used in Advanced VIRGO [118], and KAGRA [119].

For a blue-detuned high-finesse optomechanical Fabry-Pérot cavity in which the cavity's resonance frequency is less than the laser frequency, the system's effective mechanical resonance frequency is shifted to a higher frequency than the mechanical oscillator's eigenfrequency via the addition of the optical spring constant. This leads to self-stabilization of the optomechanical system at frequencies below the optical spring frequency [63]. At the optical spring frequency, however, the lag in optical response due to the round trip optical delay leads to a dominating anti-damping force that renders the system unstable [93, 94, 120]. Such anti-damping forces normally require active feedback control to stabilize the optomechanical dynamics [93, 120].

Conventionally, detuned cavities are locked by using a simple "side of fringe" locking method. In this method the error signal is obtained from the slope of the cavity intensity profile on a transmission/reflection photodetector. This error signal is filtered and fed back to a piezoelectric actuator on the cavity mirror or to the frequency of the laser. The lock bandwidth is limited by the piezoelectric transducer's mechanical resonance frequency. The laser frequency modulation on the other hand has more bandwidth, but requires a large

actuation range for short length cavities. As an alternative, in previous experiments, we have demonstrated the stabilization of the optomechanical cavity by utilizing the double optical spring effect [46].

In this paper, we introduce a new feedback control method to lock a movable mirror Fabry-Pérot cavity using radiation pressure. We have implemented this scheme at two independent experiments at LSU and MIT. This scheme relies on the suppression of external disturbances by having a large in-loop optomechanical gain as a result of the large optical spring constant. This suppression, which is mediated via the radiation pressure force, lowers the fluctuations in cavity length and power. A schematic representation of the method is shown in Figure 5.1, where the error signal is derived from the transmitted power out of the cavity and is used to control the radiation pressure force acting on the cavity by modulating the intensity of the input laser field passing through an amplitude modulator (AM). An optimal error signal is extracted by passing the transmitted field through a filter. This filter comprises of a gain and a band-pass component. The gain and low-pass filter of the servo controller are to stabilize the anti damping on the optical spring. The high-pass filter is to avoid saturation of the AM actuator due to ambient/seismic fluctuations that are largest at low frequencies (below a few kHz for a typical lab environment). These seismically and acoustically driven fluctuations in cavity length are self-stabilized in the optomechanical dynamics due to the high OM gain at frequencies below optical spring.

4.2 Theoretical framework

In understanding the noise stabilization of a strong optical spring system with feedback, it is informative to view the optical spring itself as a feedback mechanism. In this view, a closed-loop feedback system is formed between the mechanical oscillator and the optical cavity. The mechanical oscillator, with susceptibility χ_{m}, transduces a force into a displacement. The optical cavity, in turn, transduces the displacement back into a radiation pressure force, forming a closed loop. For simplicity, we consider the frequency dependent

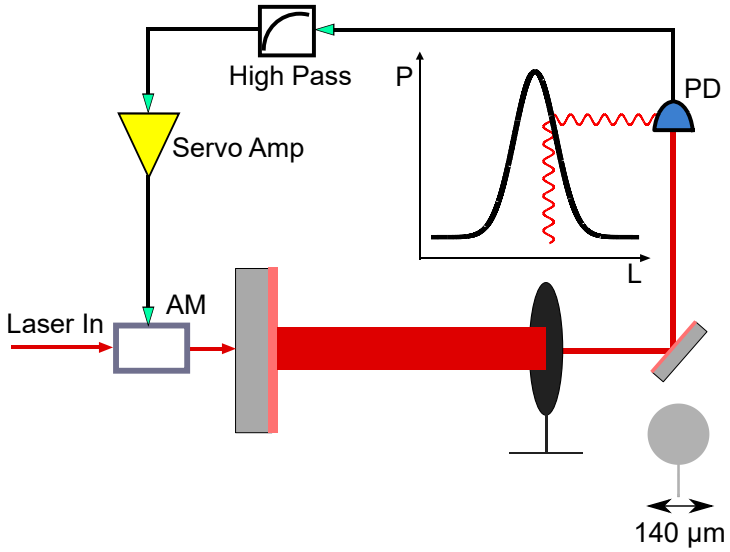

Figure 4.1: Schematic of the experimental setup. The laser is passed through an amplitude modulator (AM), which modulates the intensity of the field before entering the detuned optomechanical cavity. The light is detected in transmission of the cavity and passed through a high pass filter and servo controller containing a gain and low pass filter component to obtain the error signal which is fed back to the AM. The inset shows the scale of the movable mirror that forms one of the cavity mirrors.

susceptibility of a single mechanical resonance at Ω_{m}, such that

$$\chi_{\mathrm{m}} = \frac{1}{m\left(\Omega_{\mathrm{m}}^2 - \Omega^2 + i\Omega\Gamma_{\mathrm{m}}\right)}, \tag{4.1}$$

where Ω is frequency, m is the effective mass of the mode of oscillation, $\Gamma_{\mathrm{m}} = \Omega_{\mathrm{m}}/Q_{\mathrm{m}}$ with Γ_{m} and Q_{m} the mechanical damping and quality factor of the mechanical oscillator, respectively. [1].

The open-loop gain pertaining to the cavity's closed-loop response as shown in Figure

[1] A more realistic form including multiple resonances could be used instead, but the single resonance susceptibility works well for this analysis. This is because the higher-order modes have a larger effective mass than the fundamental mode due to their poor overlap with the cavity mode and hence don't contribute much to the broadband behavior.

4.2 may be given in the limit $\Omega \ll \gamma$ as [121]

$$\begin{aligned} G_{\rm os} &= -\frac{32\pi\chi_{\rm m}P_{\rm cav}}{c\lambda_0 T}\frac{\delta_\gamma}{(1+\delta_\gamma^2)}\left(1-\frac{2i\Omega}{\gamma(1+\delta_\gamma^2)}\right) \\ &= -\chi_{\rm m}K_0\left(1-\frac{2i\Omega}{\gamma[1+\delta_\gamma^2]}\right) \\ &= -m\chi_{\rm m}\left(\Omega_{\rm os}^2 - i\Gamma_{\rm os}\Omega\right), \\ &= \frac{\Omega_{\rm os}^2}{(\Omega_{\rm m}^2-\Omega^2+i\Omega\Gamma_{\rm m})}\left(1-i\frac{\Gamma_{\rm os}\Omega}{\Omega_{\rm os}^2}\right) \end{aligned} \tag{4.2}$$

where $P_{\rm cav}$ is the intra-cavity power, λ_o is the center wavelength of the laser, c is the speed of light, T is the total fraction of light leaving the cavity via loss and mirror transmissions, γ is the half width at half maximum (HWHM) for the cavity optical resonance in rad/s, $\delta_\gamma = \frac{\delta}{\gamma} = \frac{\omega_L-\omega_C}{\gamma}$ is the dimensionless detuning of the laser field from the cavity's resonance, and K_0 is the optical spring constant. The optical spring frequency is given by $m\Omega_{\rm os}^2 = K_0$, and its HWHM is $\Gamma_{\rm os} = 2\Omega_{\rm os}^2/\gamma/(1+\delta_\gamma^2)$. The real part of Equation 2 corresponds to a position dependent restoring force and the imaginary part corresponds to a velocity dependent anti-damping force. [2]

The effective susceptibility of the system to a force is then

$$\begin{aligned} \chi_{\rm os} &= \frac{x}{F_{\rm ext}} = \frac{\chi_{\rm m}}{1+G_{\rm os}} \\ &\approx \frac{1}{m}\frac{1}{\Omega_{\rm os}^2-\Omega^2-i\Gamma_{\rm os}\Omega}, \end{aligned} \tag{4.3}$$

where x is the displacement of the resonator, $F_{\rm ext}$, is an external force, and in the last step we assume that the $\Omega_{\rm os} \gg \Omega_{\rm m}$ and $\Gamma_{\rm os} \gg \Gamma_{\rm m}$. At frequencies below the optical spring frequency the ambient motion is therefore reduced by the factor

$$\left|\frac{\chi_{\rm m}}{\chi_{\rm os}}\right| \approx \left|\frac{\Omega_{\rm os}^2}{\Omega_{\rm m}^2-\Omega^2+i\Omega\Gamma_{\rm m}}\right|, \tag{4.4}$$

[2] This force will be anti-restoring and damping for a red detuned laser.

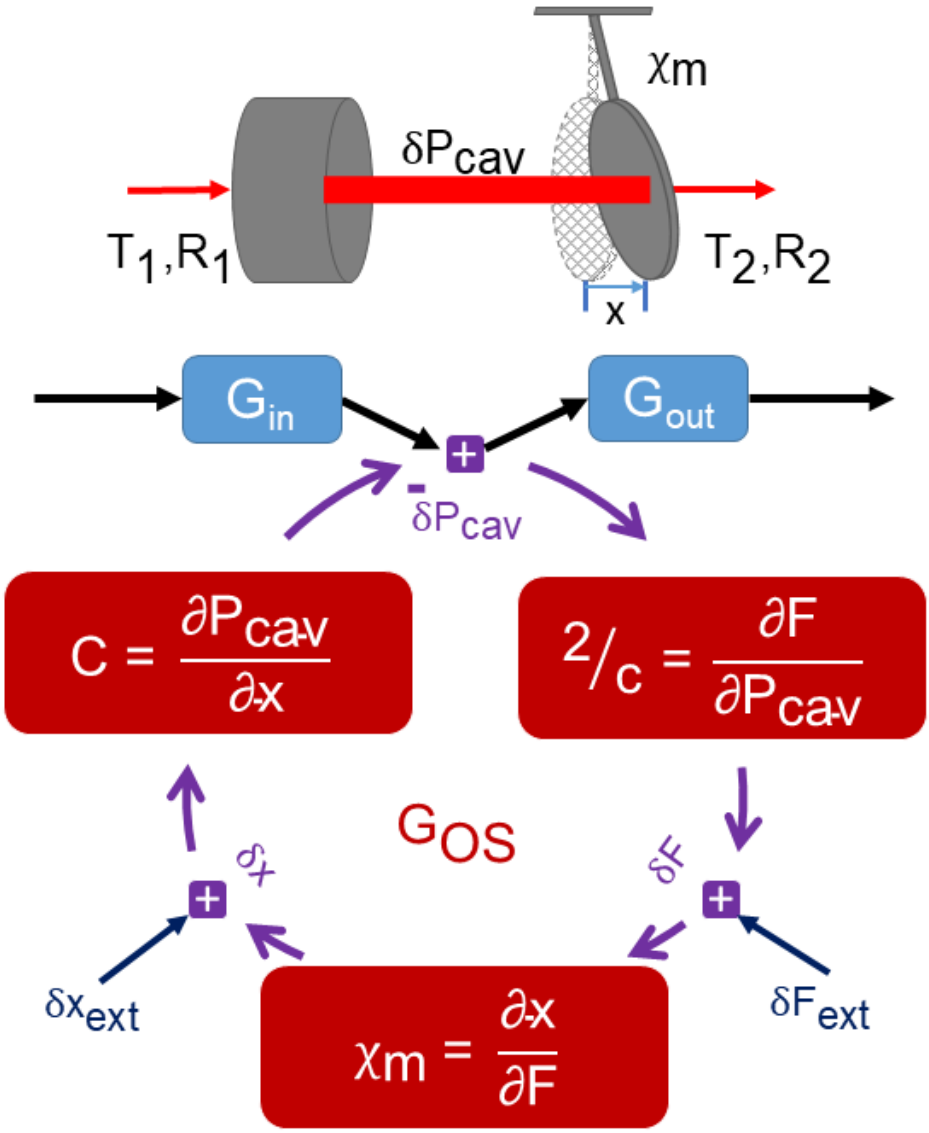

Figure 4.2: Detailed loop diagram for the cavity's transfer function. The amplitude modulator adds to the intra-cavity power P_{cav}. The cavity power converts into radiation pressure force F, which then converts into cantilever displacement x via its mechanical susceptibility χ_{m}. The displacement causes a length change for the cavity, leading again to a change in the intracavity power via the cavity response C. This forms a closed loop system.

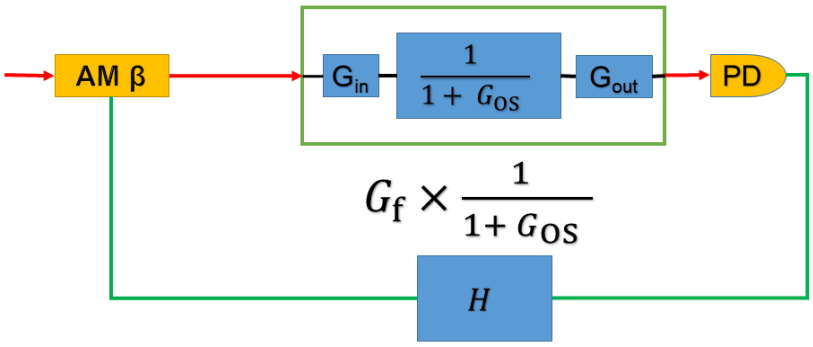

Figure 4.3: Loop diagram for the feedback $G_{\rm f}$. H is the response of the high pass filter and servo controller, and β is the response of the amplitude modulator. $\frac{1}{1+G_{\rm os}}$ is the closed loop response of the cavity's optical spring system, as shown in Fig 4.2. $G_{\rm in} = \frac{4T_1}{T^2}\frac{1}{1+\delta_\gamma^2}$ is the transfer function of the power input to power inside the cavity with the effect of the detuning taken into account, and similarly $G_{\rm out} = T_2$ is the transfer function from cavity power to transmitted power that is measured on the PD. Here T_1 is the transmission of the input mirror, T_2 is the transmission of the microresonator, and T is the total loss of power from the cavity, in the form of transmission, scattering, absorption, etc. $G_{\rm f} = G_{\rm out} \times {\rm PD} \times H \times \beta \times G_{\rm in}$ is calculated by using the measurements of the individual transfer functions.

with the approximation assuming $\Omega_{\rm os} \gg \Omega$. This factor of suppression may be made very large if $\Omega_{\rm os} \gg \Omega_{\rm m}$.

In the limit of a large optical spring frequency, the optical spring provides sufficient stabilization to maintain cavity lock. Due to the negative damping (gain) of the optical spring feedback, however, the system is unstable on its own. This can be seen by writing the closed-loop gain in the s-domain by substituting $s = i\Omega$,. The closed-loop gain $G_{\rm cl}$ corresponding to this open-loop gain $G_{\rm os}$ is given by

$$\begin{aligned} G_{\rm cl} &= \frac{1}{1+G_{\rm os}} \\ &= \frac{\Omega_{\rm m}^2 + s^2 + s\Gamma_{\rm m}}{\Omega_{\rm m}^2 + s^2 + s\Gamma_{\rm m} + \Omega_{\rm os}^2 - s\Gamma_{\rm os}} \end{aligned} \tag{4.5}$$

From the above expression, one can see that this closed-loop gain has at least one right-half-plane pole [3] and will thus be unstable. This system must be stabilized by an external damping force. The feedback may be localized to frequencies near the optical spring reso-

[3]The terms in the denominator are not all of the same sign.

nance, and its only purpose is to stabilize the unity gain crossing.

The main purpose of the applied feedback G_{f} shown in Figure 4.3 is to change the shape of the phase response of the system so that the system is stable as well as has good stability margins.

Radiation pressure is a natural transducer to stabilize such a system because there is strong coupling of radiation pressure by assumption. In addition, amplitude modulators have higher response bandwidth than piezoelectric actuators and better range than laser frequency modulation. Furthermore, because these systems are typically operated detuned (within a few line-widths to achieve strong optical springs), the transmitted power through the cavity is a natural readout of the cavity motion.

4.3 Experimental setup

The schematic shown in Figure 5.1 illustrates the experimental setup. The laser field from an NPRO Nd:YAG laser is passed through an amplitude modulator before passing through a half-wave plate and mode-matching lenses en route to the optomechanical cavity. The in-vacuum cavity is 1 cm long and consists of a 0.5-inch (12mm) diameter input mirror with a 1 cm radius of curvature and a microresonator as the second mirror. The input mirror is mounted on a piezoelectric actuator to allow for fine-tuning of the cavity length. The microresonator is fabricated from a stack of crystalline $Al_{0.92}Ga_{0.08}As/GaAs$ layers. It has a diameter of 140 µm and a mass of about 500 ng [46, 66, 67, 68, 69]. The microresonator has a natural mechanical frequency of $\Omega_{\mathrm{m}} = 2\pi \times 288$ Hz and a measured mechanical quality factor $Q_{\mathrm{m}} = 8000$, which gives $\Gamma_{\mathrm{m}} = 2\pi \times 36$ mHz.

The field transmitted through the cavity is detected by a photodetector. The photodetector signal is sent through a high-pass filter and servo controller before being used as the error signal to the amplitude modulator.

4.4 Results and Discussion

To help understand the feedback mechanisms and individual components of the feedback loops, Figure 4.2 and Figure 4.3 show the loop diagrams for the feedback loop G_{f}

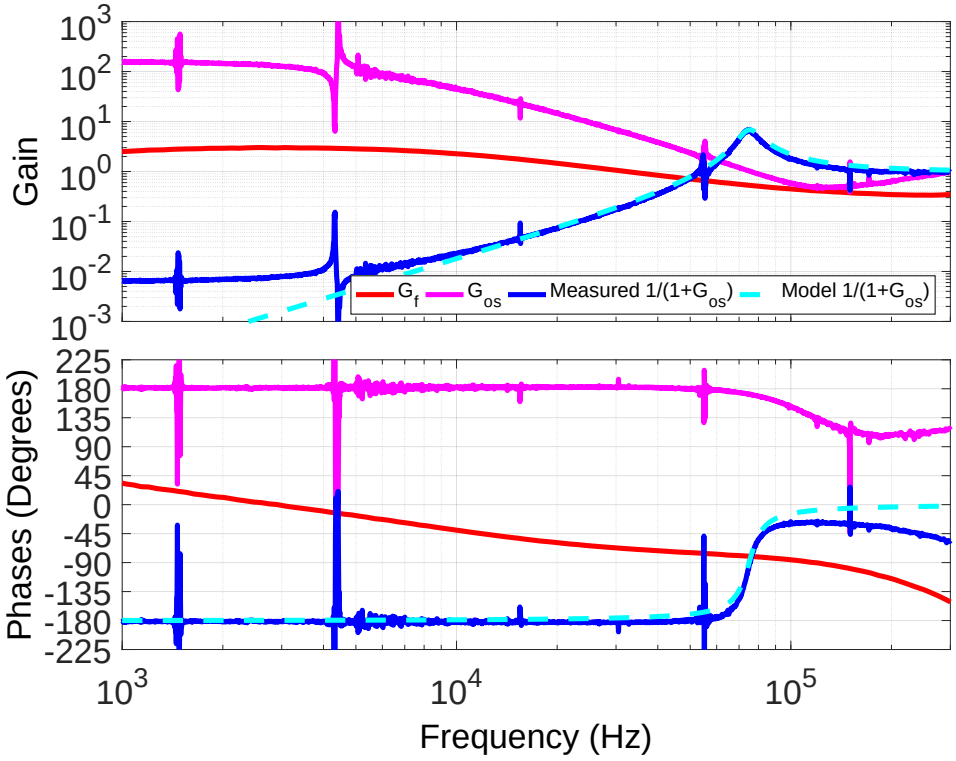

Figure 4.4: Transfer function measurements of the plant, $G_{\mathrm{CL}} = \frac{1}{1+G_{\mathrm{os}}}$ shown in blue, the feedback, G_{f} shown in red, and the open loop optical spring, G_{os} shown in pink. A model for the plant, shown in dashed cyan, is calculated with Equation 4.2 using the measured values for Ω_{os}, Ω_{m}, and Γ_{m} and setting Γ_{os} so that the peak height and width match the measured data. G_{cl} is obtained using the open loop gain, $\frac{G_{\mathrm{f}}}{1+G_{\mathrm{os}}}$, shown in Figure 4.5 and dividing out the measured G_{f}. The effect of the optical spring is visible with the peak at 75 kHz and a rise in phase of the plant transfer function. The measurement begins to flatten out below 5 kHz due to other circuitous signal couplings (eg scattered light). G_{os} is then obtained from G_{cl}. The applied feedback loop is G_{f}. At 75 kHz, G_{f} has a magnitude of 0.53 and a phase of $-80°$.

and the optical spring G_{os}. Measurements of the open loop gain, plant transfer function, individual loop gains, and closed loop gain are described below.

In Figure 4.4, the blue curves show the plant transfer function, which is the system we would like to control. We see a peak corresponding to the optical spring at around 75 kHz in the magnitude. Since the system is unstable on its own, the plant transfer function is obtained using the open loop gain measurement with the feedback on. This open loop gain is shown in Figure 4.5, and we later divide it by the measured G_{f}, shown in red in Figure 4.4 to obtain the plant transfer function.

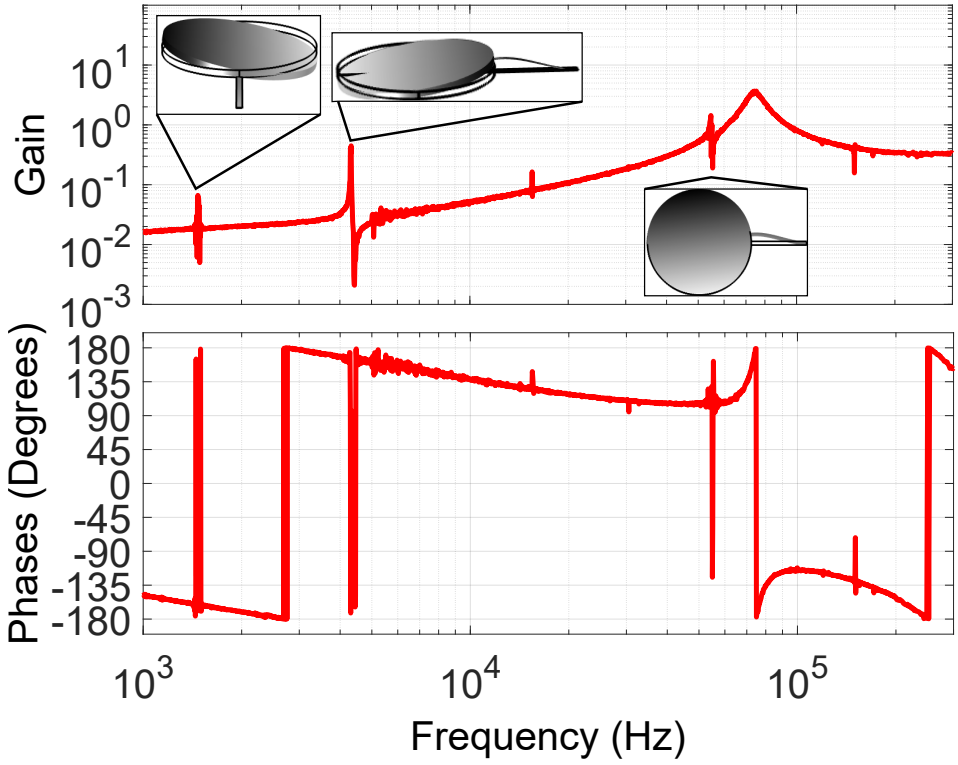

Figure 4.5: Measurement of the open-loop gain or $\frac{G_{\mathrm{f}}}{1+G_{\mathrm{os}}}$ taken by injecting a signal before H, done with a circulating power of 0.2 W. Higher-order mechanical modes are visible at 1.4 kHz (yaw), 4.3 kHz (pitch), and 54 kHz (translation and yaw) are shown in the inset. Unity-gain crossings are at 61 kHz and 93 kHz with phases 109° and −115°. The gain is 0.34 at 250 kHz where the phase crosses −180°. Thus, the system is stable with phase margins of 71° and 65°, respectively, and a gain margin of 9.4 dB.

Figure 4.4 also shows the transfer function of the $G_{\rm os}$ loop, which is obtained from the open loop transfer function shown in Figure 4.5. The large magnitude of $G_{\rm os}$ at frequencies below the optical spring shows the large suppression that the system's internal response is providing.

The external electronic feedback loop, $G_{\rm f}$, which is used to stabilize the system, is shown in Figure 4.4 in the red curves. The measurement of $G_{\rm f}$ is obtained by measuring the response of individual elements in the loop, which includes the photodetector (PD), the high-pass filter and servo controller (H), and the amplitude modulator (AM), and multiplying them together. The high-pass filter has a corner frequency at 800 Hz and the servo controller has a P-I corner at 100 kHz with a low frequency gain limit of 20 dB. We chose these values to supply sufficient phase margin while also attenuating the feedback at low-frequencies to avoid saturating the AM actuator. The measurement of the elements of $G_{\rm f}$ is done without using the cavity, so it gives the correct shape of $G_{\rm f}$, but does not provide the absolute scaling of the loop because the effect of the cavity is not included. The calibrated $G_{\rm f}$ is obtained by taking the effect of the cavity into account using the open-loop gain measurement above the optical spring peak where $\frac{1}{1+G_{\rm os}} \approx 1$.

Figure 4.5 shows the measurement of the open loop gain taken by injecting a signal before H (Figure 4.3) and measuring the response after PD. Since the measurement enters the $G_{\rm os}$ loop, the open loop transfer function is given by $\frac{G_{\rm f}}{1+G_{\rm os}}$. The effect of the optical spring is also visible in Figure 4.5 with a resonance peak at 75 kHz and a falloff with f^2 below the optical spring. There are two unity-gain crossings at 61 kHz and 93 kHz with phases of 109° and −115°. The gain at 250 kHz where the phase crosses −180° has a magnitude of 0.34. Thus, the system is stable with phase margins of 71° and 65°, respectively, and a gain margin of 9.4 dB. We note that while the $G_{\rm f}$ shown in Figure 4.4 does produce a stable system, it is not a unique solution. While other solutions for $G_{\rm f}$ may be more stable, the $G_{\rm f}$ we use is simple and achieves our goal of stabilizing the system. We also note that the measurement of $G_{\rm os}$ deviates from the expected f^{-2} slope above $\sim$ 100

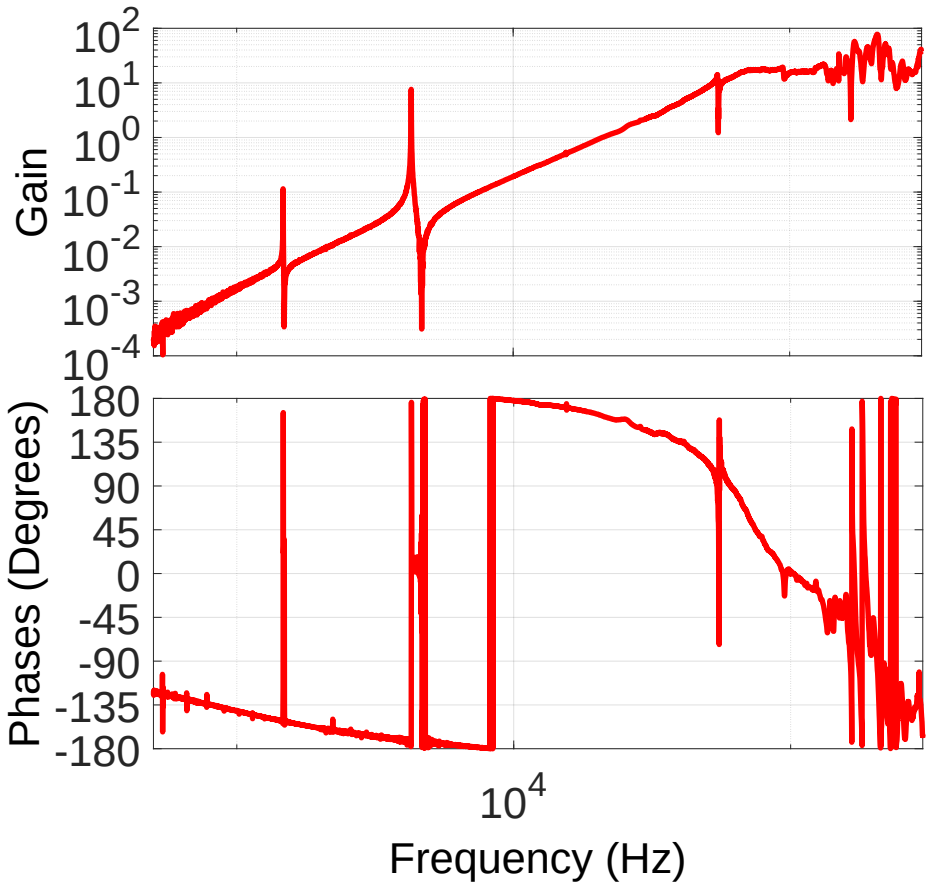

Figure 4.6: Measurement of the closed-loop response performed by modulating the laser frequency. This plot shows the suppression of low-frequency frequency noise below the optical spring frequency at ≈ 75 kHz. The amount of suppression is calculated by taking the ratio of the measurement above the optical spring and at a low frequency below the optical spring. Using the values at 100 kHz and 500 Hz, noise is suppressed by a factor of at least 50,000. Higher order mechanical modes are again visible at 1.4 kHz, 4.3 kHz, and 61 kHz.

kHz. This is a result of imperfect measurements of the individual components of the loops, which leads to errors in the subtraction for the transfer functions of $G_{\rm os}$ and $\frac{1}{1+G_{\rm os}}$.

Another result of the dynamics of the optomechanical system is the reduced response to disturbances at frequencies below the optical spring frequency. Ambient motion causes the cavity length to change by $\Delta L \sim 10^{-7}$m, while the cavity linewdith is $\Delta\lambda \sim 10^{-11}$m. It is therefore necessary to suppress the ambient motion in order to operate the cavity. Figure 4.4 shows the optical spring resonance at 75 kHz. According to Equation 4.4, the ambient motion should be reduced at low frequencies by the factor $\left|\frac{\Omega_{\rm os}^2}{\Omega_{\rm m}^2-\Omega^2+i\Omega\Gamma_{\rm m}}\right|$.

To verify this calculation, we modulate the laser frequency, which in effect, is the same as introducing a disturbance $\delta x_{\rm ext}$ in Figure 4.2. Figure 4.6 shows a measurement of

$$-\frac{L_p}{f_0}\frac{G_{\rm out}\times C\times PD}{1+G_{\rm f}+G_{\rm os}} \tag{4.6}$$

taken by modulating the laser frequency and measuring the output of the PD with $\frac{L_p}{f_0}$ the change in the laser frequency for a given change in length for the laser piezo. The amount that low-frequency vibrations are reduced by is calculated by taking the ratio of the value of the measurement above the optical spring frequency where the measurement is flat and the value of the measurement at low frequencies, yielding a suppression of at least 50,000.

The response of the system to an external force is

$$\frac{x}{F_{\rm ext}} \;=\; \frac{\chi_{\rm m}(1+G_{\rm f})}{1+G_{\rm os}+G_{\rm f}}. \tag{4.7}$$

According to Equation 4.7, ambient fluctuations are suppressed by the factor $1+G_{\rm os}+G_{\rm f}$. Since this factor is in common in Equation 4.6 and Equation 4.7, the laser frequency scan shown in Figure 4.6 is an accurate measure of the suppression of ambient fluctuations.

4.5 Conclusion

In conclusion, we have demonstrated a stable feedback control method to lock a movable mirror Fabry-Pérot cavity using radiation pressure. In this scheme, the use of radiation pressure as an actuator provides a large locking bandwidth compared to a piezoelectric transducer used in the simple "side of fringe" locking. We have experimentally shown that the system is stable and reduces low-frequency disturbances by a factor of at least 50,000. The combination of the stable system and excellent low-frequency noise suppression allows the optomechanical cavity to be operated on time scales of hours to days without losing lock. With the low-frequency noise reduced, we aim to measure broadband quantum radiation pressure noise and ponderomotive squeezing at frequencies relevant to Advanced LIGO. In addition, since the quadrature of the field inside the cavity is actually rotated

with respect to the input field, the feedback gain could be increased by modulating in a different quadrature. A modulation in an arbitrary quadrature can be achieved by stitching together two amplitude modulator crystals and adding a relative drive between them [122]. This configuration could be useful if the negative damping is too high to be compensated with a single amplitude modulator.

Chapter 5
Observation of an Optical Spring from a Beamsplitter

We present the experimental observation of an optical spring without the use of an optical cavity. The optical spring is produced by interference at a beamsplitter and, in principle, does not have the damping force associated with optical springs created in detuned cavities. The experiment consists of a Michelson-Sagnac interferometer (with no recycling cavities) with a partially reflective GaAs microresonator as the beamsplitter that produces the optical spring. Our experimental measurements at input powers of up to 360 mW show the shift of the optical spring frequency as a function of power and are in excellent agreement with theoretical predictions. In addition, we show that the optical spring is able to keep the interferometer stable and locked without the use of external feedback. This work is adapted from [123].

5.1 Introduction

Optomechanical cavities consisting of a moveable mirror or resonator allow the electromagnetic radiation of the cavity mode to couple to the motion of the mechanical oscillator. Optomechanical cavities have been proposed for improving the sensitivity of gravitational wave detectors below the standard quantum limit (SQL), tests of quantum mechanics, and quantum information [87].

One feature resulting from the coupling light to a mechanical resonator in a cavity is the optical spring effect, which was first discussed for Fabry-Pérot cavities by Braginsky [88, 89]. For the traditional case of the Fabry-Pérot cavity, the optical spring is created in a detuned cavity where the cavity's circulating power, and therefore the radiation pressure force on the mirrors, is proportional to the cavity length [92]. For a blue-detuned cavity in which the cavity's resonance frequency is less than the laser frequency, the linear relationship between the radiation pressure force and cavity length creates a positive restoring force with an effective spring constant K_{OS} and an antidamping force Γ_{OS}. The combination of the optical spring constant and the mechanical spring constant of the device combine

to shift the resonance frequency of the system from Ω_{m} to $\sqrt{\Omega_{\mathrm{m}}^2 + \Omega_{\mathrm{OS}}^2}$ where Ω_{m} is the resonance frequency of the mechanical oscillator and Ω_{OS} is the optical spring frequency [47, 63, 92]. This frequency shift is an experimental signature of the optical spring.

The antidamping force created by the optical spring can overwhelm the mechanical damping and lead to dynamic instabilities [93, 94, 120] and is usually controlled with feedback loops [47, 93, 120]. An alternative method to stabilizing the optical spring is to modify the damping force by adding a second optical spring [46, 95] or utilizing thermo-optic effects [45, 48].

Although the detuned Fabry-Pérot cavity is the canonical example of creating an optical spring, it is possible to create an optical spring in other topologies. An optical spring can be created in any system that is able to produce a linear relationship between the radiation pressure force and displacement. Dual-recycled gravitational wave detectors such as Advanced LIGO [10] and Advanced Virgo [118] are able to create an optical spring in the signal recycling cavity by detuning the signal recycling mirror [91, 111]. An optical spring can also be produced in a membrane in the middle setup [124, 125] or a Michelson-Sagnac interferometer with a tuneable signal recycling mirror at the dark port [96, 126].

These examples, however, still rely on the use of a cavity to produce the optical spring. In this paper, we present the measurement of an optical spring produced by the interaction of two input fields at a beamsplitter, which we will refer to as the microresonator, similar to the scheme outlined in [127]. To achieve this, we utilize a Michelson-Sagnac interferometer for simplicity. Previous results using a Michelson-Sagnac interferometer have included a signal recycling mirror and have not directly observed the frequency shift that accompanies the optical spring [96]. We measure the optical spring at input powers of 50 mW, 100 mW, 200 mW, and 360 mW and compare our experimental results with a theoretical model. The optical springs created at all four input powers are strong enough to keep the interferometer stable and locked without the use of any external electronic feedback or additional optical fields.

The optomechanical setup is shown in Fig. 5.1. The in-air Michelson-Sagnac interferometer contains a partially reflective microresonator as the end/common mirror of the interferometer. The Michelson-Sagnac topology was used to simplifiy the alignment of the laser beams onto the microresonator. The microresonator is similar to the one used in [46, 47] and described in [66, 69] but consists only of a 358-nm thick GaAs cantilever without the highly reflective stack of crystalline $Al_{0.92}Ga_{0.08}As$/GaAs layers. The GaAs microresonator has a power reflectivity of $R_{\rm osc} = 65\%$ for the laser wavelength of $\lambda = 1064$nm. The microresonator has a diameter of 140 µm, a mass of about 30 ng, a natural mechanical frequency of $\Omega_{\rm m} = 2\pi \times 850$ Hz. The quality factors for the fundamental and yaw resonances are $Q_{\rm m_f} = 5$ and $Q_{\rm m_y} = 13$, respectively, and are obtained by matching the theoretical model to the measured data. The low mechanical Q's are a result of performing the experiment in air. A photomicrograph of the microresonator is included as a subset in Fig. 5.1c.

5.2 Theory

To realize the optical spring, let us first consider the microresonator and its associated normalized fields as shown in Fig. 5.1b [128]. The normalized input fields a and d each receive half the power from the laser source, and we allow for a phase shift in d, accounting for the difference between the path lengths. We assume the motion of the microresonator is small and that the path length difference remains constant, so we relate the normalized fields:

$$a = \sqrt{\tfrac{P_0}{2}} \tag{5.1}$$

$$b = \rho a + \tau d \tag{5.2}$$

$$c = \tau a - \rho d \tag{5.3}$$

$$d = \sqrt{\tfrac{P_0}{2}} e^{i\phi} \tag{5.4}$$

$$\phi = \tfrac{L\omega_0}{c}, \tag{5.5}$$

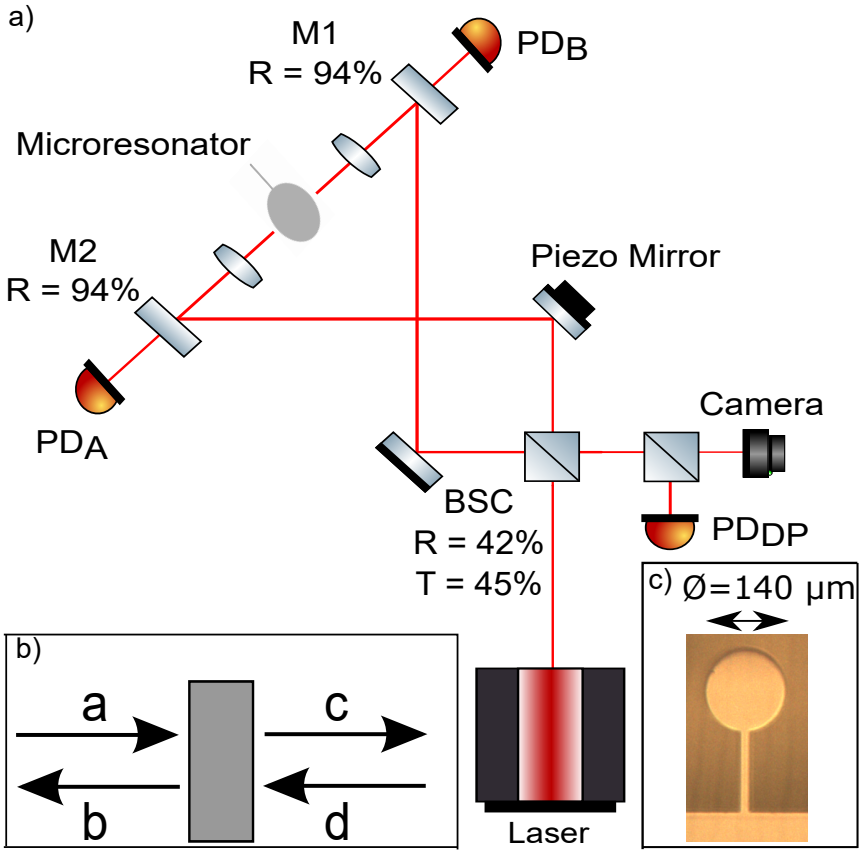

Figure 5.1: Schematic of the experimental optomechanical setup. The Nd:YAG laser is split into two beams by a beamsplitter cube (BSC) and directed towards the partially reflective microresonator. One arm of the interferometer contains a steering mirror attached to a piezoeletric transducer that generates a phase difference ϕ between the two arms of the interferometer. Both arms contain partially transmissive steering mirrors (M1 and M2) that allow some of the reflected and transmitted light to be detected for locking the interferometer. The two reflected and two transmitted beams from the microresonator interfere at the BSC and are detected by a photodetector ($\mathrm{PD_{DP}}$). (b) Fields a and d are incident on the microresonator from opposite sides. The input fields are supplied by a laser of power P_0 and frequency ω_0 with a and d each receiving about half the total power. The microresonator has power refelctivity $R_{\mathrm{osc}} = \rho^2 = 65\%$. (c) Photomicrograph of the microresonator with a diameter of 140 μm supported by a 200 μm long by 20 μm wide cantilever structure.

where ρ and τ are the amplitude reflectivity and trasmissitivity such that $\rho^2 + \tau^2 = 1$, ω_0 is the laser frequency, P_0 is the laser power incident on the beamsplitter cube, and L and ϕ are the difference in length and phase of the two interferometer arms, respectively. We solve the equations and find the net power leaving the microresonator

$$P_{\text{net}} = |b|^2 - |c|^2 = 2\rho\tau P_0 \cos\phi. \tag{5.6}$$

To understand why we are interested in the net power leaving the microresonator, consider the forces acting on the microresonator. The net force from a, b, c, and d is

$$F_{\text{net}} = (P_a + P_b - P_c - P_d)/c. \tag{5.7}$$

If the input powers P_a and P_d are balanced, then a nonzero value for $P_b - P_c$ gives rise to a net force on the microresonator exerted by radiation pressure $F_{\text{RP}} = P_{\text{net}}/c$. For small displacements δL around an equilibrium position, the microresonator experiences a differential force

$$\delta F_{\text{RP}} = \frac{1}{c}\frac{dP_{\text{net}}}{dL}\delta L \tag{5.8}$$

which can be expressed as the equivalent spring constant

$$K_{\text{OS}} \;=\; -\frac{1}{c}\frac{dP_{\text{net}}}{dL} = \frac{2}{c^2}\omega P_0 \rho\tau \sin(\phi). \tag{5.9}$$

K_{OS} is purely real indicating that it provides a restoring force without the addition of a damping force that normally arises from the imaginary part of K_{OS}. While damping from the Doppler effect does exist, it is very small in comparison to the mechanical damping in the system. The maximum K_{OS} occurs for a path difference of $\phi = \pi/2$, as shown in Fig. 5.2.

5.3 Experiment

One of the arms of the interferometer contains a steering mirror which is mounted onto a piezoelectric transducer. The piezo mirror is used to control the phase difference between the two arms of the interferometer and to lock the interferometer. The steering mirrors on either side of the microresonator have a power reflectivity of 94% to allow for some of the light to be used for locking the interferometer. The interferometer is locked by taking the signal from either $\mathrm{PD_{DP}}$, PD_A, or PD_B, filtering it, and feeding it back to the piezo mounted to the mirror in one of the arms of the interferometer. The relative phase difference between the two interferometer arms can be adjusted by tuning the locking setpoint on the PID controller.

5.4 Data and discussion

We measure the optical spring effect by measuring the optical response of the system. This is performed by modulating the piezo in the interferometer, and measuring the resulting power fluctuation at one of the photodetectors as a function of the modulating frequency. In the absence of an optical spring, we should measure a featureless response. However, with an optical spring, we measure the effective closed loop gain of the optomechanical system

$$G_{\mathrm{cl}} = \frac{1}{1+G_{\mathrm{OS}}} \tag{5.10}$$

$$= \frac{\Omega_{\mathrm{m_f}}^2 - \Omega^2 + i\Omega\Gamma_{\mathrm{m_f}}(\Omega)}{\Omega_{\mathrm{m_f}}^2 - \Omega^2 + i\Omega\Gamma_{\mathrm{m_f}}(\Omega) + \Omega_{\mathrm{OS}}^2} + \frac{\Omega_{\mathrm{m_y}}^2 - \Omega^2 + i\Omega\Gamma_{\mathrm{m_y}}}{\Omega_{\mathrm{m_y}}^2 - \Omega^2 + i\Omega\Gamma_{\mathrm{m_y}} + \Omega_{\mathrm{OS}}^2} \tag{5.11}$$

as described in [47] where the first term is for the fundamental mode and the second term is for the yaw mode with $\Gamma_{\mathrm{m_f}}$ and $\Gamma_{\mathrm{m_y}}$ the mechanical damping for fundamental and yaw modes, respectively. The contribution from the yaw mode is a result of the laser beam not being perfectly centered on the microresonator. The position dependent coupling of the optical spring to the yaw mode is analogous to attaching a mechanical spring to different

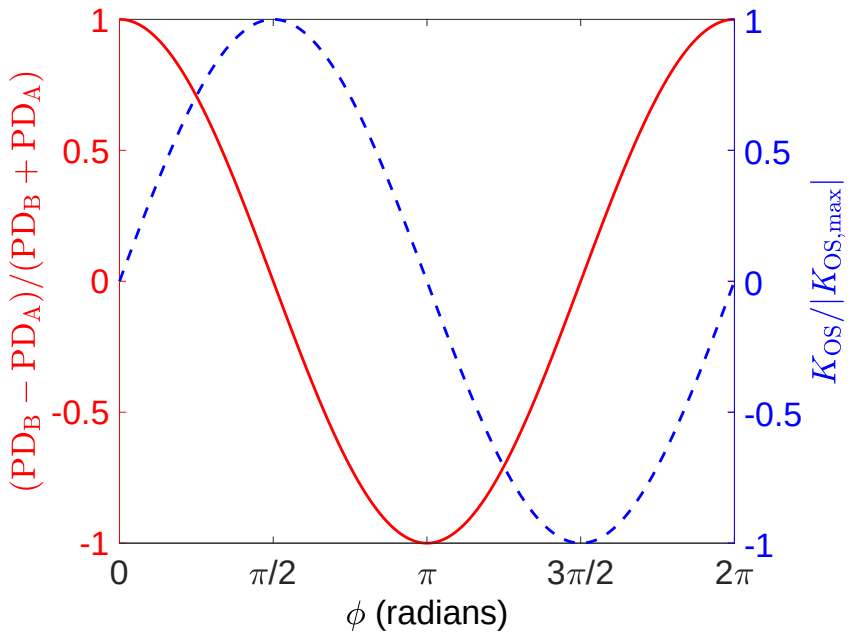

Figure 5.2: Plot of the normalized power at the side photodetectors and of the normalized $\mathrm{K_{OS}}$ as a function of ϕ. The interferometer is locked at approximately $\phi = \pi/2$ where the optical spring effect is largest.

points on the microresonator.

We lock the interferometer at the mid-fringe point of PD_B, which corresponds to the point at which the optical spring is largest, as shown in Eqs. 5.6 and 5.9, and in Fig. 5.2. We measure the transfer function at input powers of 50 mW, 100 mW, 200 mW, and 360 mW, as shown in Fig. 5.3. The optical spring peak is visible in each of the measurements at frequencies of 1000 Hz, 1120 Hz, 1310 Hz, and 1640 Hz, as well as a dip corresponding to the fundamental mechanical resonance at about 850 Hz. The effect of the optical spring is also visible on the yaw mode of the microresonator at at 4.2 kHz.

An interesting feature of the system is its ability to remain locked without any external feedback. At all four input powers, the optical spring is strong enough to stabilize the system and keep the interferometer locked at a desired fringe setpoint without the application of any feedback. Unlike the traditional case of the optical spring in a detuned Fabry-Pérot cavity where the antidamping of the optical spring must be controlled using electronic feedback or another method, our system does not have an antidamping term and

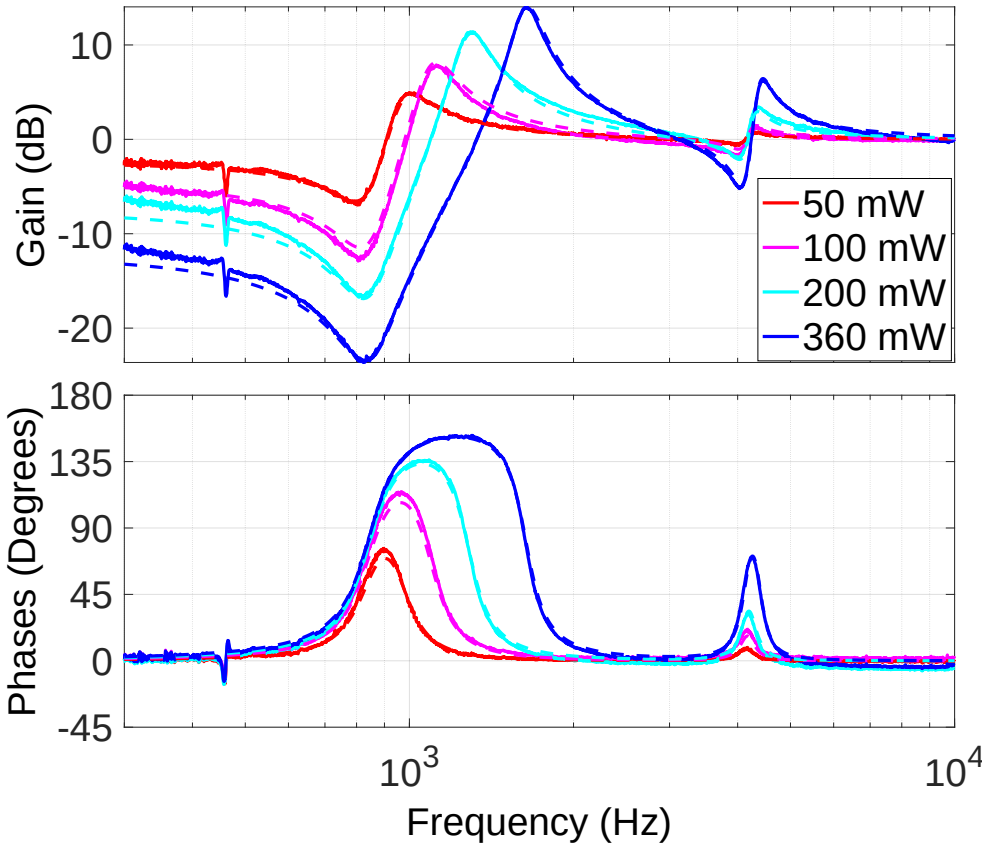

Figure 5.3: Measurements (solid) and theoretical model (dashed) of the optical spring at input powers of 50 mW, 100 mW, 200 mW, and 360 mW. The measured transfer function is taken by injecting a signal to the PID controller connected to the piezo mirror in one arm of the interferometer and measuring its effect at $\mathrm{PD_{DP}}$. The dip at about 850 Hz corresponds to the fundamental mechanical resonance of the microresonator, and the feature at 4.2 kHz is the optical spring coupled to the yaw mode of the microresonator.

is therefore stable as a result of the restoring force provided by the optical spring. External disturbances at frequencies below the optical spring frequency are suppressed by a factor of approximately

$$\frac{1}{G_{\mathrm{cl}}} \approx \frac{\Omega_{\mathrm{OS}}^2}{\Omega_{\mathrm{m}}^2} \approx 4 \tag{5.12}$$

for the 360 mW measurement at low frequencies [47, 63]. The stability of the system is visible in Fig. 5.3 where the noise at 300 Hz is suppressed by a factor of up to 11.6 dB or

a magnitude of approximately 4 [1]. Further suppression of the external disturbances could be achieved by increasing the optical spring frequency by increasing the input power.

5.5 Conclusion

In conclusion, we have shown the measurement of the optical spring from a beamsplitter in a Michelson-Sagnac interferometer, without the use of a cavity. The measurements at input powers of 50 mW, 100 mW, 200 mW, and 360 mW clearly show the change in the system's resonance frequency created by the optical spring effect and match well with theoretical predictions. The optical spring created at all four input powers is strong enough to keep the interferometer stable and locked to the desired fringe setpoint and reduces disturbances at 300 Hz by up to 11.6 dB.

In the future, we would like to investigate the possibility of using the partially reflective microresonators in experiments with quantum radiation pressure noise. As a result of not having the highly reflective stack of crystalline $Al_{0.92}Ga_{0.08}As$/GaAs layers, the mass of these microresonators is lower than the highly reflective microresonators. The reduction in mass, m, increases the signal-to-noise ratio of the quantum radiation pressure noise over the thermal noise by a factor of $\sqrt{m}$. We also aim to measure the mechanical dissipation as a function of frequency to investigate thermal noise models. In addition, the microresonators could have use in experiments studying unstable optomechanical filter cavities, such as those proposed in [129].

[1] The measurements shown in Fig. 3 are taken with the interferometer locked with the PID controller to avoid overly exciting a resonance and causing the system to lose lock

Chapter 6
Broadband Measurement of Quantum Radiation Pressure Noise at Room Temperature

Quantum mechanics places a fundamental limit on the precision of continuous measurements. The Heisenberg uncertainty principle dictates that as the precision of a measurement of an observable (e.g. position) increases, back action creates increased uncertainty in the conjugate variable (momentum). In gravitational wave (GW) interferometers, the laser power is increased as much as possible to reduce the position uncertainty created by shot noise but at the expense of back-action in the form of quantum radiation pressure noise (QRPN) [28]. Once at design sensitivity, Advanced LIGO [10], VIRGO [118], and KAGRA [119] will be limited by QRPN at frequencies between 10 Hz and 100 Hz. To improve the detection rate of GWs, ideas have been proposed to mitigate the QRPN [49, 50, 51, 52, 53, 130], but until now there has been no platform to experimentally test these ideas. Here we present a broadband measurement of QRPN at room temperature at frequencies relevant to GW detectors. The measured noise spectrum shows effects from the QRPN between about 2 kHz to 90 kHz, and the measured magnitude of QRPN agrees with our model. We now have a testbed for studying techniques to mitigate back-action, such as variational readout and squeezed light injection [51], that could be used to improve the sensitivity of GW detectors. This chapter is adapted from [131].

6.1 Introduction

Gravitational wave detectors such as Advanced LIGO continuously monitor the position of test masses using electromagnetic waves. In this case the Heisenberg uncertainty principle requires that $\Delta N \cdot \Delta\phi \geq 1/2$, where ΔN is the uncertainty in the number of photons and $\Delta\phi$ is the uncertainty in the phase. The photon number uncertainty exerts back-action (QRPN) on the mirrors on reflection, causing them to vibrate [28, 132, 133]. GW interferometers typically use as much laser power as possible in order to minimize the phase uncertainty and maximize the signal-to-noise ratio for GWs. At sufficiently high

powers, however, the QRPN becomes larger than the phase uncertainty, and it is no longer advantageous to further increase the laser power. Advanced LIGO will be limited by QRPN at low frequency when running at its full laser power.

Given the imperative for more sensitive GW detectors, it is important to study the effects of QRPN in a system similar to Advanced LIGO, which will be limited by QRPN across a wide range of frequencies far from the mechanical resonance frequency of the test mass suspension. Studying quantum mechanical motion is challenging, however, due to the fact that classical noise sources such as environmental vibrations and thermally-driven fluctuations [54] usually dominate over quantum effects. Previous observations of QRPN have observed such subtle quantum effects, even at room temperature, but these experiments have thus far been limited to high frequencies (MHz-GHz) and in a narrow band around a mechanical resonance [55, 56, 57, 58].

6.2 Experimental setup

In this work, we present a broadband and off resonance measurement of QRPN in the audio frequency band. We have developed low-loss single-crystal microresonators with sufficiently minimized thermal noise (TN) at room temperature such that the quantum effects can be observed. The optomechanical system, shown in detail in Figure 6.1, is a Fabry-Pérot cavity with a mechanical oscillator as one of the cavity mirrors. The optomechanical cavity is slightly less than 1-cm long and consists of a high-reflectivity single-crystal microresonator that serves as the input coupler and a macroscopic mirror with a 1-cm radius of curvature as the back reflector. The cavity is made slightly shorter than the 1-cm radius of curvature of the large mirror in order to achieve a small spot size on the microresonator while maintaining stable cavity modes. The microresonator consists of a roughly 70-μm diameter mirror pad suspended from a single-crystal GaAs cantilever with a thickness of 220-nm, width of 8-μm, and length of 55-μm. The mirror pad is made up of 23 pairs of quarter-wave optical thickness GaAs/$Al_{0.92}Ga_{0.08}As$ layers for a transmission of $T = 250$ ppm and exhibits both low optical losses and a high mechanical quality factor

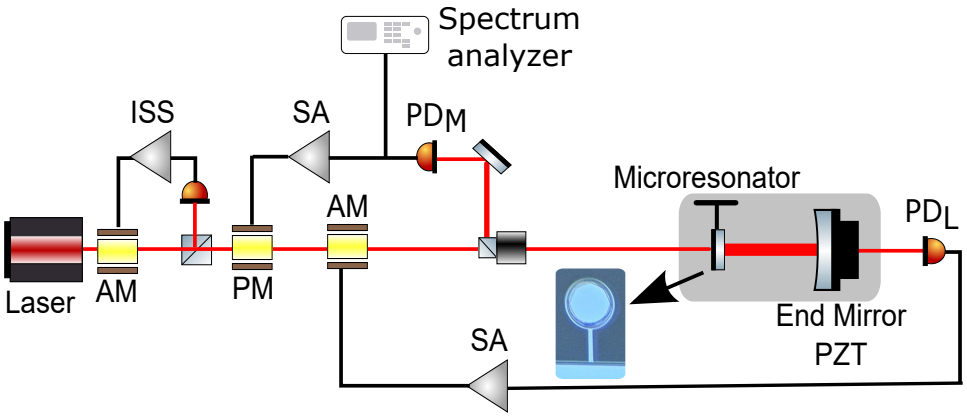

Figure 6.1: Experimental setup. Light from a 1064 nm Nd:YAG laser is passed through an amplitude modulator (AM), phase modulator (PM), and second AM before being injected into the in-vacuum optomechanical cavity, which sits on a suspended optical breadboard to reduce seismic motion (shown in shaded grey). A micrograph of the single-crystal microresonator, comprising a 70-μm diameter GaAs/AlGaAs mirror pad supported by a GaAs cantilever, is included in the diagram. An intensity stabilization servo (ISS) is used to stabilize the laser power to shot noise by feeding back to the AM. The light transmitted through the optomechanical cavity is detected by PD_L. The signal from PD_L is sent through a servo amplifier (SA) before being sent to the second AM to initiate the cavity lock sequence. The beam reflected by the cavity is detected by photodetector PD_M. The signal from PD_M is used to lock the cavity by sending it through a separate SA feeding back to the PM. The PD_L locking loop is turned off after the PD_m locking loop is active. The signal from PD_M is also sent to a spectrum analyzer for further analysis.

[46, 66, 67, 68, 69]. The microresonator has a mass of 50 ng, a natural mechanical frequency of 876 Hz, and a measured mechanical quality factor $Q_m = 16,000$ at room temperature. The cavity has a finesse of $\mathcal{F} = 13,000$ and linewidth (HWHM) of $2\pi \times 500$ kHz.

A 1064 nm Nd:YAG laser beam is passed through an amplitude modulator (AM), a phase modulator (PM), and a second AM before it is injected into the optomechanical cavity. The cavity is locked at a detuning of about 0.6 linewidths to stabilize the cavity using a strong optical spring with a resonance frequency above 100 kHz [47] using the $\mathrm{PD_L}$ and $\mathrm{PD_M}$ feedback loops as described in Figure 6.1. The final measurement configuration uses only the reflected light because the transmitted light has relatively large shot noise due to the small transmission (≈ 50 ppm) of the end mirror, which may pollute the measurement. The reflection locking with the PM is less robust, and we are not able to directly acquire lock without first using the transmission locking.

6.3 Thermal and quantum noise models

Thermal noise and quantum noise must be modeled to fully account for the measured noise in the experiment. Thermal noise, which is governed by the fluctuation dissipation theorem [134], sets a limit on the precision of mechanical experiments [59]. Thermal noise models are loosely divided into viscous or velocity-dependent models and internal friction models, depending on the source of dissipation. Structural damping models contain a frequency independent loss angle, ϕ, and for a harmonic oscillator have a displacement amplitude spectral density of

$$x(\omega) = \sqrt{\frac{4\mathrm{k_B}T\omega_\mathrm{m}^2}{\omega m Q[(\omega_\mathrm{m}^2 - \omega^2)^2 + \frac{\omega_\mathrm{m}^4}{Q^2}]}} \tag{6.1}$$

where $\mathrm{k_B}$ is the Boltzmann constant, T is temperature, m is mass, $Q = 1/\phi$ is the quality factor, $\omega = 2\pi \times f$, and ω_m is the angular frequency of the mechanical mode [54]. For structural damping, the thermal noise falls off as $1/\omega^{5/2}$ above the mechanical resonance frequency. Viscous damping, on the other hand, is proportional to $1/\omega^2$ above the mechanical

resonance [54].

We model the TN using a finite element model of the microresonator that is constrained by measurements of the frequencies and quality factors of the fundamental mode and the next three higher-order modes. We infer the modal mass for each mode by using the TN measurement presented below and are able to reproduce the inferred modal masses using the finite element model. The TN spectrum is calculated using Eq. 6.1 by summing the contribution of each mechanical mode in quadrature.

The quantum noise is modeled using the input-output relations, which consist of a set of equations that relate the output fields to the input fields [62, 63]. Cavity losses are also included and serve as an input for vacuum fluctuations to enter the cavity. The dynamics of the microresonator are added based on the same finite element model that is used for the thermal noise model and measurements of the Q, frequency, and modal mass of each mechanical mode. This data is used to calculate the mechanical susceptibility of the microresonator. The cavity losses and detuning from resonance are determined by measurements of the optical spring. Using the optical spring measurement to constrain the cavity losses also allows us to rule out photothermal effects [135] because any excess damping would be observed in mechanical response measurements. The input-output relations give the circulating power inside the cavity and the amount of light that is transmitted and reflected by the cavity for the carrier and sideband fields. The QRPN, shown in Figure 6.2, is calculated using these input-output relations and is proportional to $1/\omega^2$ above the mechanical resonance frequency.

6.4 Results and discussion

After the cavity is locked, the signal from PD_M is sent to a spectrum analyzer for analysis. We measure an uncalibrated noise spectrum by first measuring the power spectral density of the error signal. We calibrate the spectrum by dividing it by the transfer function from the laser-cavity piezo to our error signal. This method treats the optical spring as a feedback loop as described in [47], and by removing its effect, we restore the observed

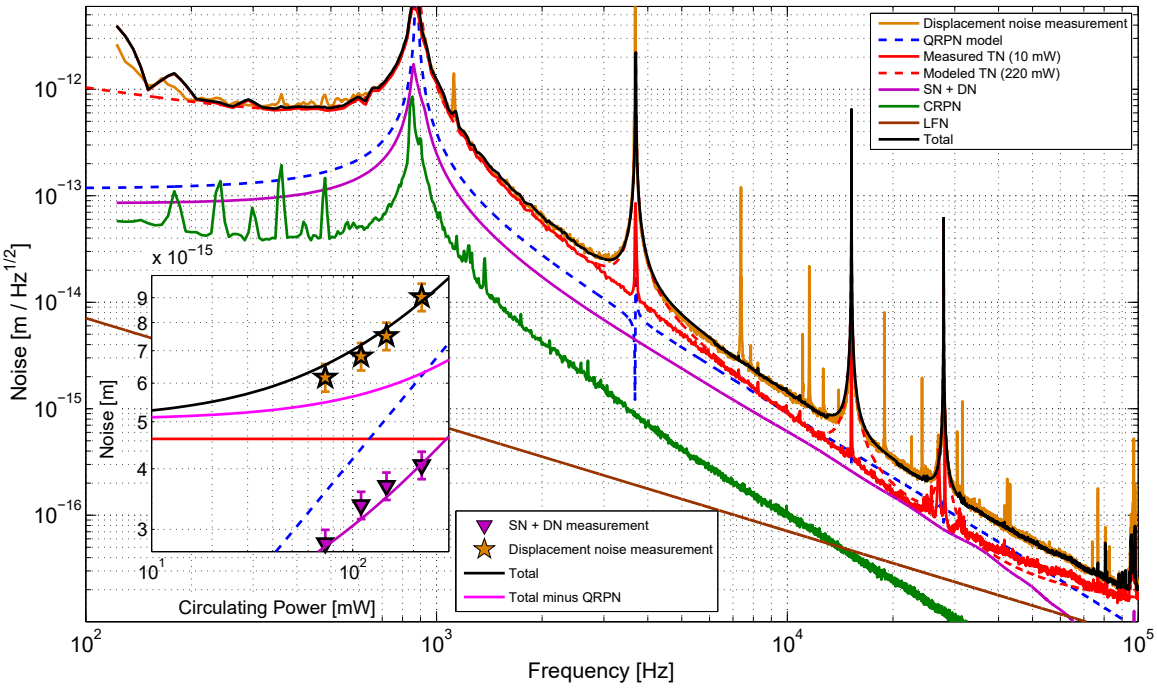

Figure 6.2: Noise spectrum taken with a cavity circulating power of 220 mW as a function of frequency (f). The noise spectrum includes shot noise (SN) and dark noise (DN), classical radiation pressure noise (CRPN), laser frequency noise (LFN), measured and modeled thermal noise (TN), modeled QRPN, and a displacement noise measurement. The contributions from SN and DN, CRPN, thermal noise, and modeled QRPN are added in quadrature for a prediction of the total noise. The total noise includes a contribution from the measured TN away from the resonances of the higher order mechanical modes and uses the modeled TN around the resonance peaks to account for the change in mode coupling between low and high circulating power as described in the text. The TN measurement was taken with 5% of the circulating power used in the displacement noise measurement shown in orange. The peaks that are present in the displacement noise measurement that are not associated with a mechanical resonance are a result of nonlinear coupling that is not present at low circulating powers. The inset includes four measurements at circulating powers of 73 mW, 110 mW, 150 mW, and 220 mW to show how each of the noise sources scale with cavity circulating power. Each type of noise shown in the noise spectrum is integrated over a 1 kHz frequency bin between 21 kHz and 22 kHz. The purple triangles are measurements of the SN plus DN, and the purple curve is a model of the SN plus DN. The stars correspond to the displacement noise measured for the four power levels and the red line is the measured TN. CRPN and LFN are not shown in the inset because they are well below the other noise sources. The black curve in the inset is the expected total noise including the contributions from the measurements of SN and DN, CRPN, LFN, TN, and the modeled QRPN and is not a mathematical fit of the data points. The error bars on the measured data represent the measurement error based on the statistical uncertainty from multiple measurements. The magenta curve is the expected total noise without including the contribution from QRPN.

displacement spectrum to what it would be in the absence of the optical spring and our electronic feedback. The laser piezo has been calibrated in frequency, which allows the resulting signal to be calibrated to displacement by using the cavity length.

To measure the TN, we decrease the circulating power to a level at which the QRPN is small compared to the Brownian motion of the microresonator and shot noise remains insignificant. The measurement of TN, shown in Figure 6.2, agrees with the structural damping model from 200 Hz to 30 kHz. We observe excess noise above 30 kHz, which may be related to thermoelastic damping, but is not entirely understood. The modeled TN shown in Figure 6.2 includes a thermoelastic damping contribution from the low Q drumhead mode that is between 5 MHz and 10 MHz based on the finite element model of the microresonator. The measured noise also deviates from the model around the yaw mode at 3.7 kHz, pitch mode at 15 kHz, and side-to-side mode at 28 kHz as the coupling of these modes changes as a function of power due to radiation pressure induced torque. The coupling to all three modes was minimized for a low circulating power when the thermal noise measurement was taken. At higher circulating powers the radiation pressure force from the light is enough to bend the cantilever structure and cause the beam to hit the mirror at a slightly different location, enhancing the optomechanical coupling.

We take measurements at four cavity circulating powers of 73 mW, 110 mW, 150 mW, and 220 mW while maintaining a constant cavity detuning of about 0.6 linewidths. The detuning of 0.6 linewidths is chosen to maximize the circulating power inside the cavity while maintaining a stable feedback loop to lock the cavity. The optical spring frequencies for the four measurements are 104 kHz, 119 kHz, 131 kHz, and 137 kHz, respectively. The noise spectrum of the 220 mW measurement is shown in Figure 6.2. The noise spectrum shows that QRPN is the largest displacement noise source between 10 kHz and 50 kHz. Below 10 kHz, thermal noise is the biggest contributor to the displacement noise, but the effect of QRPN is still visible in the displacement noise measurement down to 2 kHz, where it accounts for about 30% of the measured displacement noise. The measured classical

radiation pressure noise (CRPN) from intensity fluctuations of the laser and laser frequency noise are below the other noise sources across the measurement band [136].

The data from each of the four displacement noise measurements, along with other known noise sources, is shown in the inset in Figure 6.2 where it has been integrated over a 1 kHz band between 21 kHz and 22 kHz. QRPN scales with the square root of power [28] and is the largest noise source for circulating powers above 150 mW. For the measurement at 220 mW shown in the inset of Figure 6.2, QRPN represents 48% of the total noise, while the TN accounts for 27%, and the shot noise (SN) plus dark noise (DN) contributes 21% of the total noise. TN is the biggest noise source for circulating powers below 150 mW, but again, QRPN still contributes to the total displacement noise at circulating powers of 10 mW and below. For each of the measurements shown in the inset of Figure 6.2, the sum of SN and DN is the third largest noise source. While SN scales with the square root of power, the purple triangles shown in the inset of Figure 6.2 include a contribution from DN and thus deviate from the expected scaling. While it may be counter intuitive that SN (calibrated to length) increases with power, this scaling is well understood as a result of the optical spring suppressing the signal [63]. Removing the effect of the optical spring using the calibration discussed above causes the white shot noise to have the frequency dependence shown in Figure 6.2 and the power dependence shown in the inset [47, 63]. We sum the contribution of each of the noise sources to compute the total expected noise. We find that our four displacement noise measurements, shown as orange stars in the inset, agree with the total expected noise (black curve in the inset) with the statistical measurement error taken into account. The measurement error is calculated by repeating the measurement multiple times and is dominated by the fluctuations in the transfer function measurement that is used to calibrate the spectrum. The magenta curve shown in the inset of Figure 6.2 is the predicted displacement noise without a contribution from QRPN. All four measurements of the displacement noise rule out the model without QRPN.

One effect that might mimic QRPN is bulk heating of the cantilever mirror caused by

the absorption of the laser light. Due to the structural damping observed in our device, the mirror motion is dominated by TN below 10 kHz, while still being QRPN limited above. The low frequency TN may be used as a thermometer to measure any heating as a result of higher power. To explain the factor of two increase in noise observed at 20 kHz between low and high power as a result of heating, the temperature would have had to increase by a factor of 4. We can rule out this large increase in temperature by observing that the measured noise at frequencies dominated by TN (between 1 kHz and 2 kHz for example) only increases by 2%, which is within measurement uncertainty.

6.5 Conclusion

In conclusion, we present a measurement of quantum radiation pressure noise in a broad band of frequencies far from resonance of the mechanical oscillator. The observed noise spectrum shows the motion of the micro-resonator is affected by QRPN between about 2 kHz to 90 kHz. Analyzing all known significant noise sources, we show that the QRPN is the largest contributor between 10 kHz and 50 kHz, and that it scales as the square root of the optical power, as expected for quantum noise.

Since the first proposals of interferometric GW detectors, QRPN has been known to present a fundamental limit to the low frequency sensitivity of GW detectors. For the past two decades, the measurement of QRPN at frequencies relevant for gravitational wave detectors has eluded increasingly sensitive experiments. Meanwhile, several proposals for reducing QRPN [49, 50, 51, 52, 53, 130] have been relegated to theoretical concepts without the means to experimentally test them. This measurement of QRPN at frequencies in the gravitational wave band opens up the possibility of experimental tests of QRPN-reduction schemes. In addition, we are currently within a factor of five of the standard quantum limit [32] at room temperature, which paves the way for a sensitivity below the standard quantum limit by cryogenically cooling the microresonator to reduce the TN.

Measurement back-action limits the sensitivity of all force and position measurement. Moreover, QRPN buffets the mirrors of GW detectors, limiting the sensitivity to GWs.

Measuring the QRPN over this broad frequency band enables experimental tests of QRPN-reduction schemes to manipulate and mitigate this vexing noise source. More fundamentally, this measurement amounts to observation of the quantum vacuum fluctuation moving a macroscopic object.

6.6 Looking forward: Limits on cavity circulating power

In the experiment and results described above, the circulating power inside the optomechnical cavity was brought up to 220 mW. While further increasing the circulating power would increase the effects of QRPN, there were several factors that limited the amount of power inside the cavity.

One limiting factor on the amount of circulating power inside the cavity is the speed of the feedback control loops used to lock the cavity. We rely on a large optical spring to keep the cavity locked. Increasing the power inside the cavity, and hence the frequency of the optical spring, causes the optical spring response to broaden in frequency. The combination of the high frequency and broadness of the optical spring pushes the unity gain frequency of the feedback control loop to 200 kHz and above and reduces the gain and phase margins at the unity gain crossing. The gain margin can be increased by increasing the gain on the servo amplifier in the control loop, but this further reduces the phase margin and eventually causes the loop to become unstable. We reduced the optical and electric path lengths between the sensor (photodetector PD_M) and the actuators (amplitude and phase modulators) in the control loop to reduce delays and increase the phase margin in the feedback. Further increasing the phase margin to allow for more light inside the cavity will require further reducing the delay in the feedback loop. We have recently purchased fiber modulators that we hope will allow us to reduce these delays.

Another limiting factor to the amount of power that we can achieve inside the cavity is the amount of range on the piezo that is attached to the macroscopic mirror. The cavity is initially locked at a large detuning, and the piezo is used to decrease the detuning to the desired operating point. In this experiment, the cavity was locked at a detuning of

$\delta_\gamma = 0.57$ linewidths from resonance. Nearly all of the piezo's range was utilized to achieve this detuning. Further increasing the power by shifting to a smaller detuning would require a piezo with more range to be installed.

Increasing the speed of the feedback control loops and increasing the range of the piezo may allow us to increase the circulating power by a factor of two or three and thereby increase the QRPN by a factor of $\sqrt{2}$ to $\sqrt{3}$. The ultimate limit to the amount of power that can circulate inside the cavity is set by the fact that the classical radiation pressure force will at some point be strong enough to break the cantilever mirror. Previous generations of cantilever mirrors have broken at approximately 500 mW of circulating power. The current generation of cantilever mirrors is expected to have a higher threshold power before breaking because they have lower absorption than previous generations. For the current generation of cantilever mirrors that are used in this experiment, we have yet to reach (and have not actively tried) a high enough circulating power to break the mirror, so we do not know the upper limit to the amount of power that can be inside the cavity. Collaborators at the Albert Einstein Institute in Hannover, Germany are currently investigating the power threshold and breaking mechanism.

Chapter 7
Quantum Radiation Pressure Noise Reduction and Evasion

The measurement of quantum radiation pressure noise in Chapter 6 creates the opportunity to study various techniques for reducing QRPN. This chapter describes two experiments in which we reduce the amount of QRPN. The first experiment demonstrates the elimination of QRPN from the measurement, or QRPN evasion, by modifying how the light from the cavity is detected. The second experiment modifies or squeezes the light that is injected into the optomechanical cavity by altering the quantum mechanical fluctuations in the amplitude and phase quadratures of the light. The motivation for doing each of these experiments stems from the fact that they represent two methods that have been proposed for reducing quantum radiation pressure noise in gravitational wave detectors [51], with squeezing currently being installed in the LIGO interferometers for reducing the shot noise during the third observing run and beyond.

7.1 Back-action evasion

In the experiment described in Chapter 6, the laser light is injected through the cantilever mirror side of the optomechanical cavity and detected in reflection of the cavity. In order to perform a QRPN evasion measurement, the experimental setup is modified so that the light is injected through the macroscopic mirror and detected in transmission of the cavity, as shown in Figure 7.1. This simple change in where the light is injected into the cavity and where the light is detected after interacting with the cavity allows for the QRPN to be removed from the detected light. This fact was realized by Yanbei Chen in 2012 but has not been previously published [137]. The theory behind the back-action evasion measurement is described below.

For light that is detected in the amplitude quadrature in transmission of an optomechanical cavity under the influence of a strong optical spring, the three sources of amplitude fluctuations are:

1. Intracavity amplitude fluctuations δI_q when the movable mirror isn't moving.

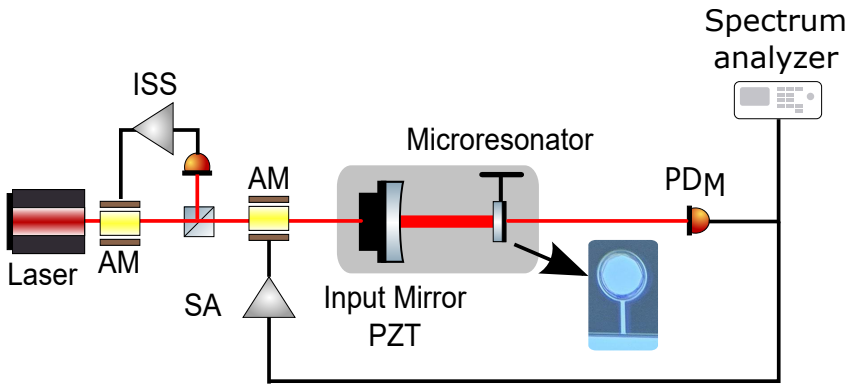

Figure 7.1: Experimental setup for the back-action evasion measurement. Light from a 1064 nm Nd:YAG laser is passed through two amplitude modulators (AM) before being injected into the in-vacuum optomechanical cavity, which sits on a suspended optical breadboard to reduce seismic motion (shown in shaded grey). A micrograph of the single-crystal microresonator, comprising a 70-μm diameter GaAs/AlGaAs mirror pad supported by a GaAs cantilever, is included in the diagram. An intensity stabilization servo (ISS) is used to stabilize the laser power to shot noise by feeding back to the AM. The light transmitted through the optomechanical cavity is detected by $\mathrm{PD_M}$. The signal from $\mathrm{PD_M}$ is sent through a servo amplifier (SA) before being sent to the second AM to lock the cavity. The signal from $\mathrm{PD_M}$ is also sent to a spectrum analyzer for further analysis.

2. Fluctuations produced by the mirror motion δx.

3. Fluctuations in the amplitude quadrature of the vacuum field that is directly reflected from the output mirror.

The intracavity amplitude fluctuations make up a fraction of the light that is inside the cavity and produce fluctuations in the amplitude quadrature equal to

$$a_{\mathrm{intracavity}} = \frac{\delta I_q}{2I_{\mathrm{in}}}, \tag{7.1}$$

where I_{in} is the total amplitude of the light inside the cavity, and the factor of 2 is a result of moving from amplitude to power.

The amplitude fluctuations produced by the motion of the mirror can be written as

$$a_{\mathrm{BA}} = \frac{1}{2I_{\mathrm{in}}}\left(\frac{\partial I_{\mathrm{in}}}{\partial x}\right)\delta x. \tag{7.2}$$

For a system with a strong optical spring, the motion is given by Hooke's law

$$\delta x = \frac{2I_{\mathrm{in}}}{c}\frac{1}{K_{\mathrm{OS}}}, \tag{7.3}$$

where K_{OS} is the optical spring constant

$$K_{\mathrm{OS}} = -\frac{2}{c}\left(\frac{\partial I_{\mathrm{in}}}{\partial x}\right). \tag{7.4}$$

Inserting Equations 7.3 and 7.4 into Equation 7.2 yields

$$a_{\mathrm{BA}} = \frac{1}{2I_{\mathrm{in}}}\left(\frac{\partial I_{\mathrm{in}}}{\partial x}\right)\left(2\frac{\delta I_q}{c}\right)\left(-\frac{2}{c}\frac{\partial I_{\mathrm{in}}}{\partial x}\right)^{-1} = -\frac{\delta I_q}{2I_{\mathrm{in}}}. \tag{7.5}$$

The result of Equation 7.5 is equal in magnitude but opposite in sign to Equation 7.1. Combining Equations 7.1 and 7.5 gives

$$a_{\mathrm{intracavity}} + a_{\mathrm{BA}} = 0. \tag{7.6}$$

The remaining source of amplitude fluctuations in the light transmitted by the cavity is the amplitude fluctuations of the vacuum field that is directly reflected by the output mirror. Hence, the measurement of the amplitude quadrature in transmission of the cavity is free from the QRPN of the light that is injected into the cavity.

The derivation performed above for light detected in transmission of the optomechanical cavity fits within the larger concept of variational readout schemes [51, 138]. Variational readout interferometers have modified output optics to achieve a frequency dependent readout angle of the light that exits the interferometer. The interferometer readout is performed with a homodyne detector, which is sensitive to all readout quadratures rather than a single quadrature. The frequency dependence is obtained by reflecting the interferometer output field off of a detuned optical cavity or "filter cavity." The detuned filter cavity imprints

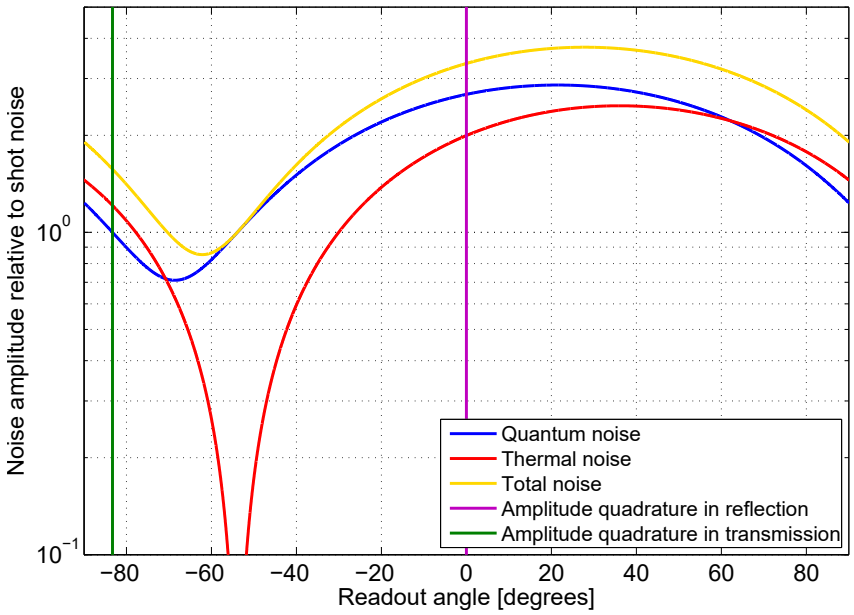

Figure 7.2: Total noise, quantum noise, and thermal noise at 20 kHz as a function of readout angle with a circulating power of 220 mW. The amplitude quadrature for light detected in reflection of the cavity is set at 0 degrees and marked with the vertical purple line. The amplitude quadrature for the light detected in transmission is marked with the vertical green line.

a frequency dependent amount of phase on the output light, which rotates the readout quadrature of the detected light as a function of frequency [51, 139]. The advantage of using a variation readout scheme on the output light of the interferometer is the ability to completely remove the back-action noise from the light detected at the output of the interferometer.

In this context the above derivation is similar to a variational readout type measurement in which the back-action is removed from the measurement. The scheme and result presented here, however, differ from the proposals in [51, 138] in that our optical system is a detuned Fabry-Perot rather than a Michelson interferometer. This results in a frequency independent readout angle for frequencies below the optical spring frequency with the amplitude quadrature of the transmission light as the quadrature in which the back-action is canceled. Figures 7.2 and 7.3 show how the quantum noise, thermal noise, and total noise at 20 kHz vary as a function of readout angle for the light detected in transmission of the

cavity. Figure 7.2 assumes a circulating power inside the cavity of 220 mW to match the power used in the QRPN measurement in Chapter 6. Figure 7.3 is modeled with a circulating power of 10 mW, which is similar to the thermal noise measurement in Chapter 6, where thermal noise is the largest noise source. In both figures, the noise is scaled to shot noise, and there are two readout angles at which the quantum noise curve is equal to one. At these points, the quantum noise is equal to the shot noise and contains no contribution from quantum radiation pressure noise.

An interesting feature that appears in both Figures 7.2 and 7.3 is the the quantum noise dips below the shot noise level for a range of readout angles between about -80 degrees and -60 degrees. This reduction of the quantum noise below the shot noise level represents the ponderomotive squeezing that the optomechanical cavity produces, which will be discussed in more detail in Chapter 8. Comparing the two figures demonstrates how thermal noise can overwhelm an attempt to measure ponderomotive squeezing when it is the largest noise source. When this is the case, the total noise never goes below the shot noise level, as in Figure 7.3. When the quantum noise is the largest noise source, however, the total noise drops below shot noise for a small range of readout angles, as seen in Figure 7.2. It is interesting that the minimum of the total noise does not occur at either the minimum of the thermal noise or the minimum of the quantum noise. This is a result of the total noise be the sum of the two individual noise sources, which do not have a minimum at the same readout angle. The minimum of the thermal noise occurs at a readout angle that is insensitive to the motion of the cantilever mirror. This is also evident by the fact that the total noise is equal to the shot noise at this readout angle. The quantum noise, however, does not have a minimum at this location because the ponderomotive squeezing produced by the cavity relies on the quantum correlations that are produced by the mirror's movement [89].

Figures 7.2 and 7.3 do not include technical noise sources, so they serve more as a proof-of-principle that the total noise can be reduced rather than a detailed noise budget.

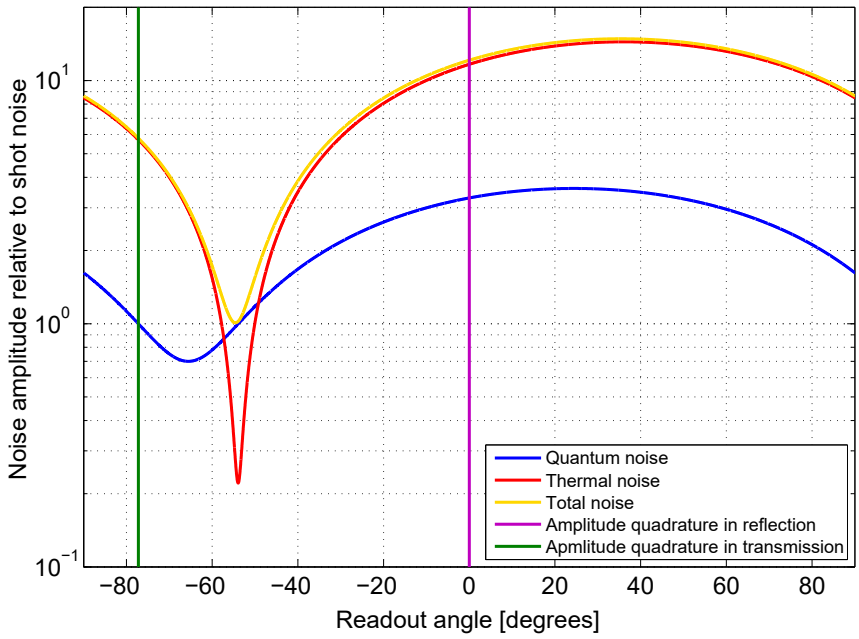

Figure 7.3: Total noise, quantum noise, and thermal noise at 20 kHz as a function of readout angle with a circulating power of 10 mW. The amplitude quadrature for light detected in reflection of the cavity is set at 0 degrees and marked with the vertical purple line. The amplitude quadrature for the light detected in transmission is marked with the vertical green line.

Before switching the orientation of the cavity, we performed a benchmark measurement of the displacement noise of the cavity with the light injected on the cantilever mirror side of the cavity and detected in reflection. The cavity orientation and feedback for this measurement mimic that of the QRPN measurement in chapter 6. The benchmark measurement was performed with an input power of 50 μW, a circulating power of 150 mW inside the cavity and a detuning of 0.57 linewidths. With these parameters, the optical spring frequency was measured to be 145 kHz. The measurement of the optical spring, along with the cavity detuning and input power, was used to calculate the intracavity loss to be 190 ppm.

To switch which side of the cavity the light is incident on, an optical fiber was simply switched from a fiber coupler on the side of the cavity with the cantilever mirror to a fiber coupler on the side of the macroscopic mirror. The same photodetector, PD_{M}, was used to detect the light in the back-action experiment as in the radiation pressure experiment in Chapter 6. In this orientation, the cavity feedback uses an amplitude modulator, as shown in Figure 7.1, rather than the phase modulator used in Chapter 6. The back-action evasion experiment was performed with the same detuning, circulating power, and optical spring frequency as the benchmark measurement described above to keep the parameters consistent between the two measurements.

The results from both the benchmark measurement and the back-action evasion measurement are shown in Figure 7.4. The inset shows the reduction in noise by plotting the ratio (in dB) of the measured displacement noise of the evasion measurement to the displacement noise of the benchmark measurement. The measured displacement noise is reduced between $\sim$ 2 kHz and $\sim$ 50 kHz, with a reduction of 2 dB at 20 kHz. A detailed noise budget of the noise sources that contribute to the back-action evasion measurement is shown in Figure 7.5. The largest noise source in Figure 7.5 is the thermal noise, which is plotted in red. The next largest noise source is the combination of the shot noise and dark noise of PD_{M}. The shot noise show in Figure 7.5 is smaller than the shot noise plotted in

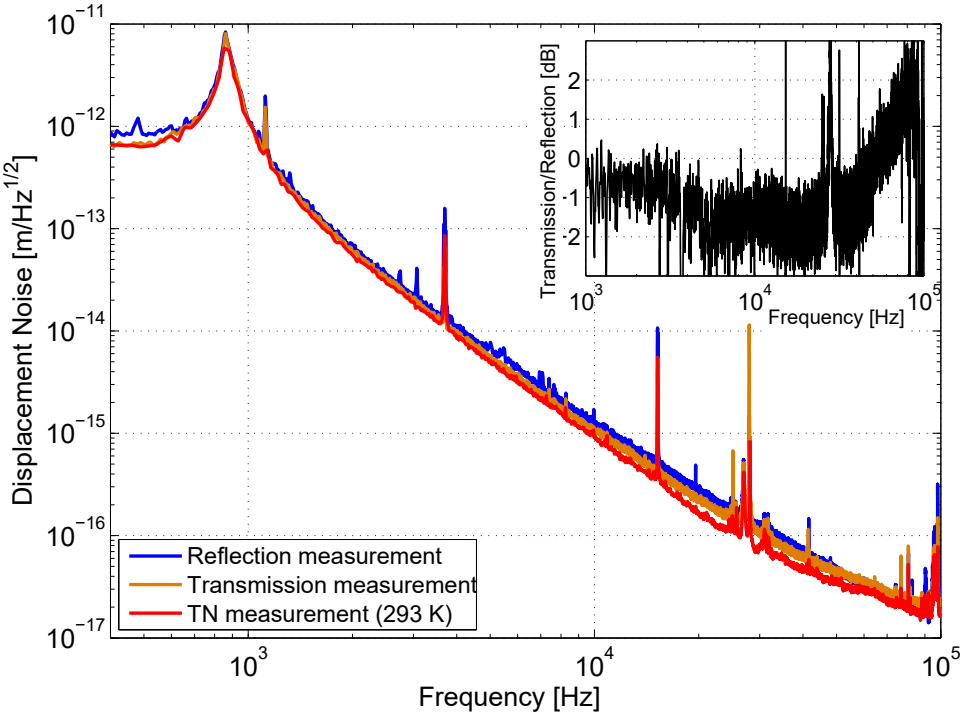

Figure 7.4: Measured displacement spectrum in reflection (blue) and transmission (orange) of the cavity. A measurement of the thermal noise (TN, red) is also plotted for reference. The inset shows the ratio (in dB) of the measured displacement noise of the transmission measurement to the displacement noise of the reflection measurement.

Figure 6.2 . This is a result of the light being detected in transmission of the cavity, which means that PD_{M} does not have any light that is directly reflected from the cavity as it does in Chapter 6. This effect decreases the amount of light measured at the photodetector and therefore the amount of shot noise in the measurement. The other two noise sources, the classical laser intensity noise and laser frequency noise, are both smaller than the thermal noise and shot noise in the measurement band. We calculate the total noise budget by adding the four noise sources in quadrature. As seen in Figure 7.5, the sum of the individual noise sources (black curve) agrees with the measured displacement noise (orange curve) across the entire measurement band from 100 Hz to 100 kHz. We also calculated what the expected displacement noise would be if the amount of QRPN that is present in the reflection measurement were to also appear in the transmission measurement. When this extra term is added to the noise budget, the expected noise, which is shown in grey in Figure 7.5, no longer agrees with the measured displacement noise. This effect is largest between 10 kHz and 40 kHz where the QRPN would have the largest contribution.

The spectra shown in Figures 7.4 and 7.5 are cleaner and contain fewer lines than the spectrum shown in Chapter 6. The cleaner spectra are a result of reducing the optomechanical coupling between laser beam and the higher order mechanical modes of the cantilever mirror. The optomechanical coupling was reduced by more finely positioning the laser beam at the node of the mechanical modes. To achieve the position accuracy necessary to reduce the optomechanical coupling strength, we installed a tuneable voltage source to the linear piezo-actuated positioning stages that control the position of the mirror relative to the laser beam and light inside the cavity. The positioning of the mirror relative to the laser was previously done with a fixed step size that limited the accuracy of the positioning. The tuneable voltage source allows for positioning on the order of 100 nm.

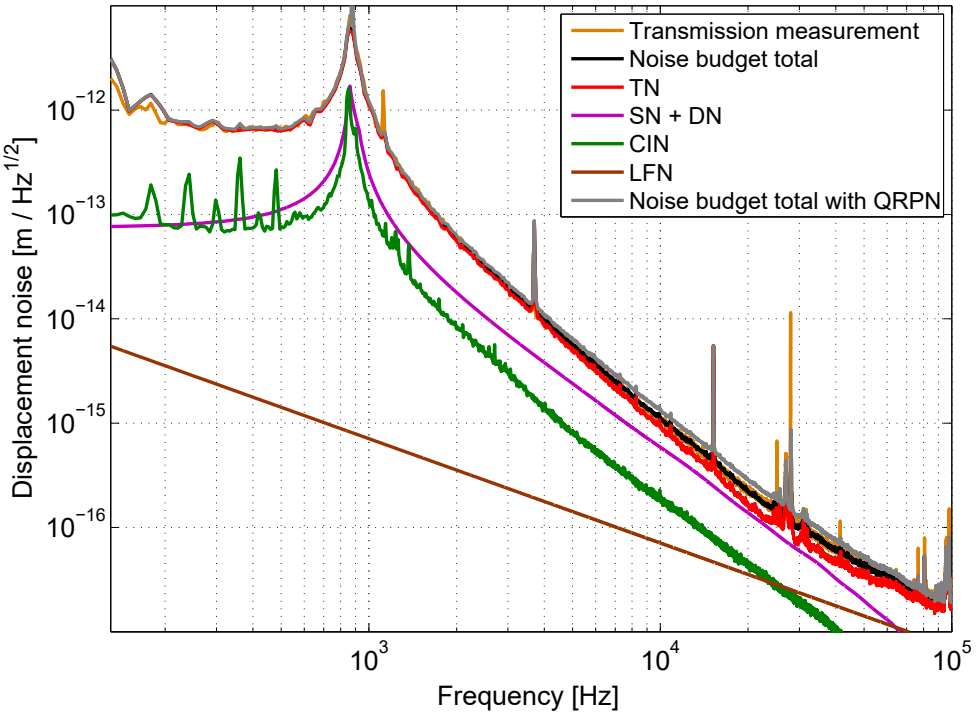

Figure 7.5: Noise budget for the QRPN evasion measurement in transmission of the cavity. The noise sources that contribute to the measured displacement noise are thermal noise (TN), shot noise and dark noise (SN + DN), classical laser intensity noise (CIN), and laser frequency noise (LFN). Adding these noise sources in quadrature produces the noise budget total (black curve). Including a contribution in the noise budget from the QRPN that would be present in a measurement in reflection of the cavity yields the grey curve, which disagrees with the displacement noise measured in transmission of the cavity (orange curve).

7.2 Reduction of quantum radiation pressure noise with bright squeezed light

7.2.1 Generation of bright squeezed light

The second experiment that demonstrates the reduction of quantum radiation pressure noise involves altering the light injected into the optomechanical cavity. In the following experiment, the coherent field from the laser is replaced by a bright squeezed field, also known as squeezed light, as described in Chapter 1.

Previous experiments involving squeezed states in gravitational wave detectors have all utilized phase squeezed states to reduce the uncertainty or noise in the phase quadrature or shot noise [33, 34, 35], but amplitude squeezed states have yet to be used to reduce quantum radiation pressure noise in the amplitude quadrature at audio band frequencies. The reduction of QRPN by using amplitude squeezed light has only recently been demonstrated at MHz frequencies [140] because QRPN itself has only recently been measured [55, 56, 57, 58]. As described in Chapter 6, we now possess a system that is dominated by QRPN in the audio band and serves as a testbed for various proposals for reducing QRPN. In collaboration with the Australian National University, we have designed an experiment to reduce QRPN by injecting amplitude squeezed light into the optomechanical cavity. In addition, we can show that the optomechanical interaction between the movable mirror and phase squeezed light further amplifies the noise in the amplitude quadrature.

The design of the experiment is shown in Figure 7.7. The preparation of the light that is injected into the cavity, the feedback control loops to lock the cavity, and the detection of the light in reflection of the cavity are all identical to the experiment described in Chapter 6 except for the fact that the unsqueezed coherent state injected into the cavity is replaced by a amplitude squeezed coherent state.

The bright squeezed state is created using the following procedure [141]. A portion of the laser (Main Laser) that is injected into the cavity is picked off and used as the pump field for a second harmonic generation (SHG) cavity. The Fabry-Perot SHG cavity contains a nonlinear Periodically Poled Potassium Titanyl Phosphate (PPKTP) crystal within the

cavity. The PPKTP crystal converts around 50 % of the 1064 nm light into a frequency doubled 532 nm field. The crystal is placed inside the cavity to enhance the interaction and increase the amount of green light that is produced. The green light generated by the SHG cavity is passed through a phase modulator (PM) to produce sidebands at 70 MHz for locking the Optical parametric oscillator (OPO) cavity using the Pound-Drever-Hall locking technique [142].

The frequency-shifted light is then used as the pump field for the optical parametric oscillator (OPO) cavity. The OPO cavity is doubly resonant for 1064 nm and 532 m light and contains a second PPKTP crystal. The PPKTP crystal is temperature-controlled and wedged to maintain the dual resonance of both wavelengths. A portion of the pump light reflected from the OPO is detected at a photodetector, whose signal is passed through a servo amplifier system and fed back to a piezoelectric transducer on one of the OPO cavity mirrors to lock the cavity on resonance.

Some of the green photons that pass through the PPKTP crystal in the OPO cavity are converted into two 1064 nm photons. Since they originate from the same green photon, the two red photons are correlated. The correlation between their upper and lower sidebands gives rise to a squeezed vacuum field that exits the cavity. The squeezed vacuum field is then combined with the coherent field at a 97 % reflective beamsplitter (SQZ BS). The reflection of the beamsplitter contains the bright squeezed field, which is injected into the optomechanical cavity. Figure 7.6 depicts a simplified schematic of how the squeezed vacuum field is combined with the coherent field.

7.2.2 Reduction of quantum radiation pressure noise

In order to reduce QRPN, the bright squeezed state injected into the cavity must have a reduction in noise in the amplitude quadrature. The quadrature in which the bright squeezed state is squeezed is dependent on the relative phase between the squeezed vacuum field and the coherent field. The control of this angle is done in a two-step process using a second laser field. First, we frequency shift the coherent locking field (CLF) laser by 12.5

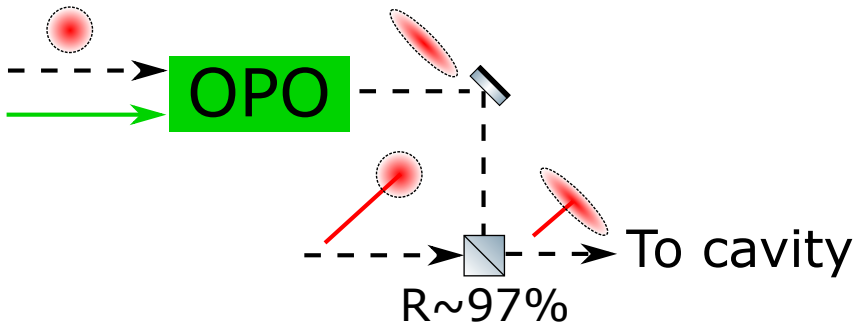

Figure 7.6: Simplified schematic of the production of a bright squeezed state [143]. The squeezed vacuum field from the OPO is combined with a strong coherent field at a beamsplitter. The output of the beamsplitter is a bright squeezed state and is injected into the optomechanical cavity.

MHz at 1064 nm from the main laser and pass it through a single-pass SHG (SPSHG) to create a small amount of 532 nm light. The 532 nm light produced by the SPSHG is frequency shifted from the green light produced in the SHG cavity. We then combine the two green fields at a beamsplitter (Green BS) and detect them with the Green CLF PD. We use the beat note of the two green fields at 25 MHz to lock the phase of the two fields at 532 nm by feeding back to the Main Laser PZT.

In the second step, we use the 1064 nm light from the CLF laser that is not frequency doubled by the SPSHG. This field is reflected off the OPO cavity and copropogates with the squeezed vacuum toward the SQZ BS. We detect both the 1064 nm fields from the main laser and CLF laser with the Red CLF PD. The 12.5 MHz beat note between the two fields on this PD is used to lock the phase of the 1064 nm fields together. We can change the relative phase of the two fields by feeding back to a piezo mirror in the green OPO pump field, which changes the phase between the 12.5 MHz and 25 MHz phase lock loops.

The combination of both of these phase locking loops is used to lock the phase of the coherent field and the OPO pump field. This in turn stabilizes the squeezing quadrature of the bright squeezed field injected into the optomechanical cavity.

We then inject the bright squeezed light into the optomechanical cavity and detect the light in both transmission and reflection of the cavity. The cavity locking sequence for the

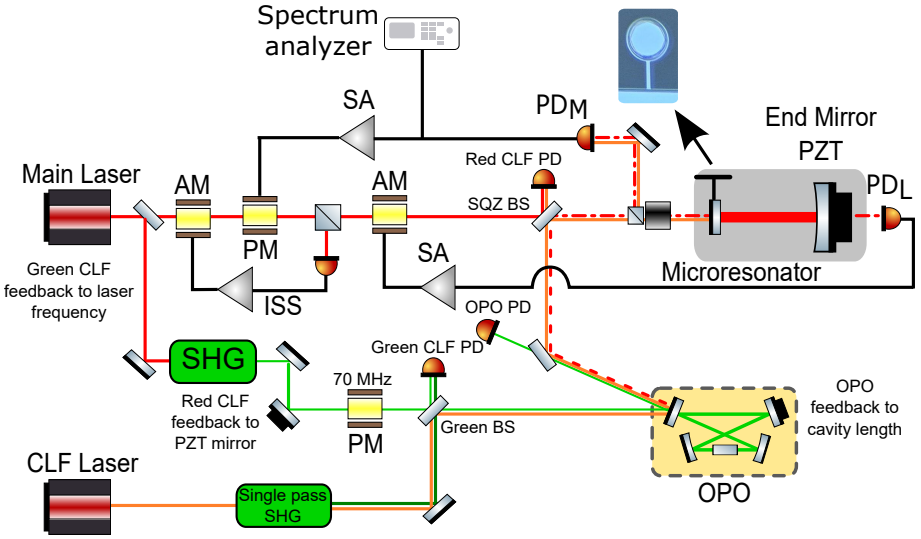

Figure 7.7: Experimental setup for the generation and injection of bright squeezing into the optomechanical cavity. Light from a Nd:YAG laser (main, red line) is split at a beamsplitter, with part of the light being sent towards the optomechanical cavity, and the other portion used as the pump field for the SHG cavity. Some of the light that passes through the SHG cavity is frequency doubled to 532 nm and passed through a phase modulator (PM) before being used as the pump for the OPO cavity. A second Nd:YAG laser (CLF, orange line) is offset in frequency by 25 MHz from the main laser. The CLF laser pumps a single-pass SHG (SPSHG) to produce a small amount of frequency doubled light. Both frequency doubled beams are interfered at a beamsplitter (Green BS) and detected by the Green CLF PD to lock the phase of the two lasers together at 532 nm. The light from the SPSHG is used as the seed for the OPO cavity. The OPO cavity is doubly resonant for 1064 nm and 532 nm light and contains a wedged PPKTP crystal that is used to correlate the sidebands of the 1064 nm vacuum field in the cavity. These correlations produce squeezed vacuum. The squeezed vacuum is sent from the cavity to a 97 % reflective beamsplitter (SQZ BS), where it combines with the coherent field from the main laser to create bright squeezed light. At the same beamsplitter, the seed beam is combined with the main laser and detected on the Red CLF PD to lock the phase of the two lasers together at 1064 nm. The bright squeezed light is then injected into the optomechanical cavity and detected in transmission and reflection. The transmission PD, PD_{L}, is used to feed back to an amplitude modulator (AM) in the main laser path to initially lock the cavity as described in Chapters 4 and 6. The reflection PD, PD_{M}, is used to feed back to a separate PM in the main laser path. Once the PD_{M} control loop is active, the PD_{L} loop is turned off. The signal from PD_{M} is also sent to a spectrum analyzer for analysis.

cavity is identical to that in Chapter 6. The reflected light is detected at PD_{M} and sent to a spectrum analyzer for analysis. First, we take a reference trace with no squeezed light by locking the OPO cavity to the resonance that is resonant for 532 nm light but not for the 1064 nm light. Locking the OPO to this "wrong" resonance ensures that the OPO does not produce any squeezing. We measure the power spectrum of the cavity for this reference using the spectrum analyzer. Next, we lock the OPO to the correct resonance to produce squeezing, and vary the phase angle between the squeezed field and the coherent field until the power spectrum is minimized (for amplitude squeezing) and maximized (for amplitude anti-squeezing). Since we are only using a single photodetector, PD_{M}, to measure the squeezing, we are only able to detect the amplitude quadrature of the light. We measure the squeezing and anti-squeezing at PD_{M} with the cavity both locked and unlocked to confirm that the reduction in the displacement noise when the cavity is locked corresponds to when amplitude squeezing is injected.

The measured spectra of the reference and squeezing and anti-squeezing with the cavity unlocked are shown in Figure 7.8. Around 20 kHz, amplitude squeezing is 2.2 dB below the shot noise reference, and the anti-squeezing is 15.5 dB above the shot noise reference. The bright squeezed and anti-squeezed fields in Figure 7.8 contain 50 μW of optical power when they are combined at the SQZ BS and are reduced to 25 μW of power at PD_{M} by optical losses between the SQZ BS and PD_{M}. The amount of bright squeezing measured with the cavity unlocked is limited by optical losses that introduce uncorrelated vacuum fields and degrade the squeezing. The loss sources are listed in Table 7.1. The diffraction loss at the cantilever was determined by measuring the total loss between the optical fiber and the photodetector and accounting for the individually measured loss sources. We increased the quantum efficiency of PD_{M} from 85 % to 97 % by retroreflecting the light that is reflected from the photodiode window back onto PD_{M}.

The measured spectra of the reference and squeezing and anti-squeezing with the cavity locked are shown in Figure 7.9. The spectra shown in Figure 7.9 include the effects of the

Table 7.1: Optical efficiencies and losses in the path of the squeezed field. The mode matching efficiency and intracavity loss are only applicable when the cavity is locked.

Parameter	Value
OPO escape efficiency	96 ± 1 %
SQZ beamsplittler transmission	97 ± 0.5 %
Fiber coupling efficiency	85 ± 2 %
Faraday isolator transmission	96 ± 1 %
Input optics efficiency	93.5 ± 1 %
Diffraction loss at cantilever mirror	20 ± 5 %
Photodiode quantum efficiency	97 ± 1 %
Mode matching efficiency	75 ± 5 %
Intracavity loss	180 ± 10 ppm

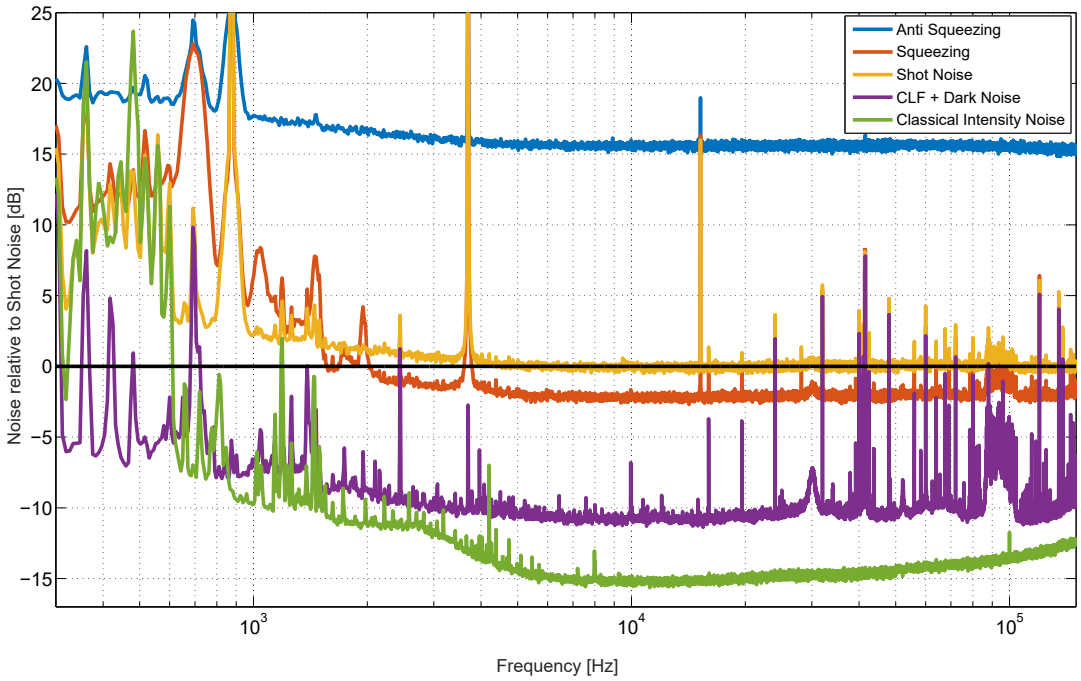

Figure 7.8: Noise spectrum of bright squeezing and anti-squeezing scaled to shot noise. The squeezed and anti-squeezed fields contain 25 μW of optical power when they are detected at PD_{M}. The black horizontal line serves as a reference for 0 dB. The shot noise reference measurement is done with the OPO cavity locked to a point that is resonant for the 532 nm light but not for the 1064 nm light, so no squeezing is produced. The squeezing and anti-squeezing measurements are performed with the OPO locked to the resonance that is resonant for both 532 nm and 1064 nm light. The noise is reduced by 2.2 dB with amplitude squeezing and increased by 15 dB with anti-squeezing. The noise from the CLF control loops lies 10 dB below the reference trace, and the classical intensity noise is about 15 dB below the reference.

optical spring, which appears as the broad peak at 150 kHz. Keeping the optical spring in the spectra, as opposed to removing in as in Figure 6.2, makes it easier to see the effects of the squeezing and anti-squeezing. With the optical spring still in the data, the quantum radiation pressure noise is flat, and the structural thermal noise has a slope of $1/f^{1/2}$ below the optical spring frequency. Around 20 kHz, QRPN in the largest noise source, and the measured displacement noise is reduced by 1.2 dB below the reference when amplitude squeezing is injected and increased by 10.2 dB when anti-squeezing is injected. Below 20 kHz, the amount of observed squeezing is reduced as the thermal noise becomes larger than the QRPN, but the reduction in noise is still visible below 2 kHz. Compared to the spectra with squeezing and without squeezing, the spectrum with anti-squeezing is much flatter at frequencies below the optical spring. This is a result of QRPN being the dominant noise source. At frequencies below 10 kHz, the anti-squeezing spectrum slopes slightly upward as the thermal noise makes a small contribution to the total displacement noise. The inset in Figure 7.9 shows a zoomed graph of the displacement noise spectrum with a calibration line created by injecting a signal at 11.2 kHz to the piezo attached to the back of the macroscopic cavity mirror. This injection shows up as a peak in the displacement noise measurement. If we consider the injection as signal that we are trying to measure, then we can determine the amount that injecting squeezing or anti-squeezing increases or decreases the signal-to-noise ratio [144]. The injection of the squeezed light reduces the noise at 11 kHz from $6 \times 10^{-18\mathrm{m}}/\mathrm{Hz}$ to $5.3 \times 10^{-18\mathrm{m}}/\mathrm{Hz}$, which corresponds to a 13 % or 1.1 dB increase in the signal-to-noise ratio. Injecting anti-squeezing increases the background noise at 11 kHz from $6 \times 10^{-18\mathrm{m}}/\mathrm{Hz}$ to $1.8 \times 10^{-17\mathrm{m}}/\mathrm{Hz}$, resulting in a 340 % or 10.6 dB decrease in the signal-to-noise ratio. In addition, we used the injection to ensure that the calibration remained constant across measurements. This consistency is evident in the inset of Figure 7.9 as the amplitude of the peak staying consistent across all three measurements.

To confirm that the decrease (increase) in the displacement noise is due to the reduction (amplification) of QRPN and not simply the decrease (increase) in shot noise at the

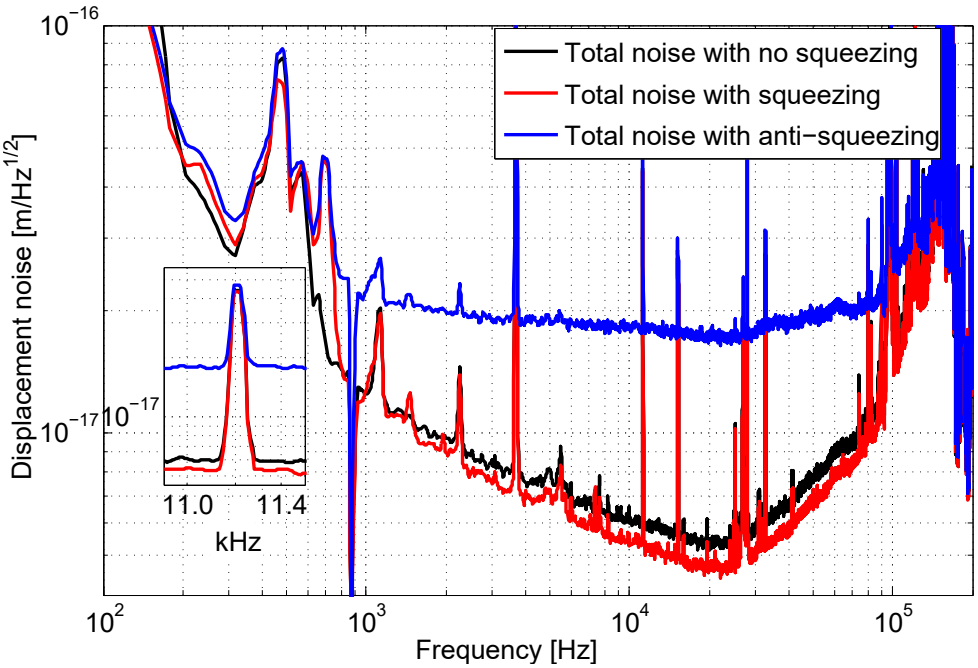

Figure 7.9: Displacement noise measurement with squeezed and anti-squeezed light injected into the cavity. The total noise is reduced between 1.5 kHz and 90 kHz, with the largest reduction of 1.2 dB around 20 kHz. The displacement noise is increased between 800 Hz and 100 kHz when anti-squeezing is injected. The noise is 10 dB above the reference at 20 kHz. The narrow peak at 11.2 kHz is an injected calibration line that is used to check that the calibration is constant between the three measurements. The narrow peaks at 3.7 kHz, 15 kHz, and 25 kHz are higher order mechanical modes of the cantilever mirror. The broad peak at 150 kHz is the optical spring resonance. The inset shows the added calibration line for all three measurements.

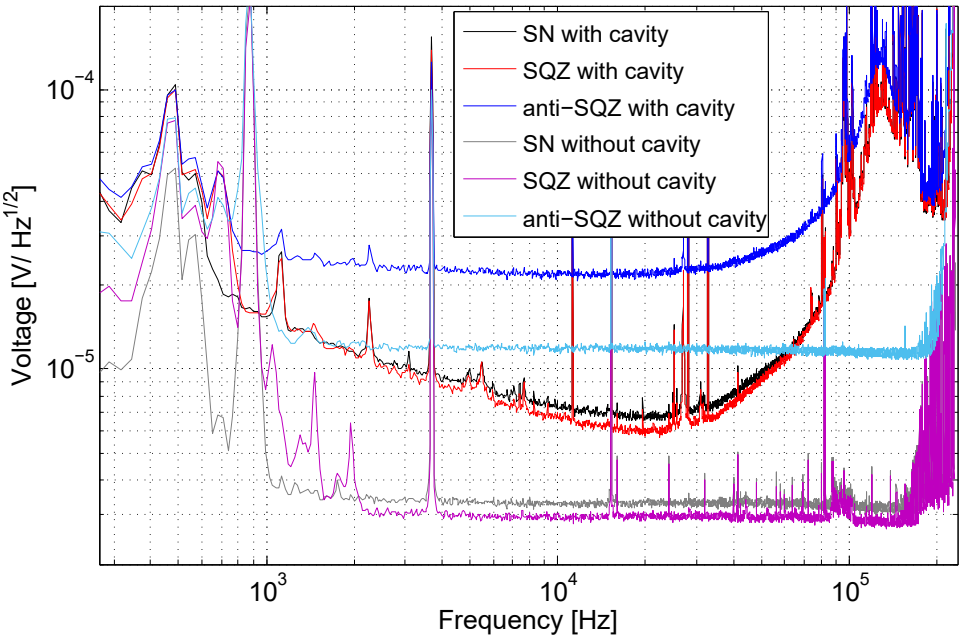

Figure 7.10: Measured squeezing and anti-squeezing with and without the cavity locked. A shot noise reference is shown for both cases.

photodetector, we compare the squeezing results with and without the cavity using the power spectrum with units of Volts. The comparison is shown in Figure 7.10. Using the shot noise without the cavity locked as a reference, the anti-squeezing without the cavity locked is 9.6 dB above the reference. The measured anti-squeezing with the cavity locked is 15 dB above the reference. The extra 5.4 dB of noise measured with the cavity locked is a result of the increase in the QRPN of the cavity. The increase in noise can be understood as the optomechanical cavity acting as a squeezer and amplifying or anti-squeezing the noise of the light that is injected. The amount of squeezing measured with the cavity locked is also limited by optical losses, which are included in 7.1. The intracavity loss is determined by fitting measurements of the optical spring with a model. We are currently working on incorporating the measured losses and noise sources into a detailed noise budget.

In the future, reducing the amount of optical loss between the OPO and the optomechanical cavity will increase the benefits of injecting squeezed light and will further reduce the total displacement noise. The additional benefit of more squeezing is currently limited by the fact that thermal noise lies below the QRPN across the measurement band. To

further exploit the benefits of injecting more squeezed light, the thermal noise will need to be decreased by cryogenically cooling the cantilever mirrors.

7.2.3 Author contributions

The research described in this section was done in collaboration with David McClelland's group in the Department of Quantum Science at the Australian National University. The experiment was built and performed in Thomas Corbitt's laboratory at Louisiana State University. David McClelland's group provided the squeezed light source. Min Jet Yap led the construction of the squeezed light source with input from Georgia Mansell, Bram Slagmolen, Robert Ward, Terry McRae, Daniel Shaddock, and David McClelland.

Chapter 8
Future Work and Conclusion

The measurement of quantum radiation pressure noise in the audio-frequency band opens the door for many exciting future projects. As described in Chapter 7, a QRPN-limited system provides a test bed for studying methods to reduce or mitigate QRPN. More generally, it presents a system to investigate mechanics of macroscopic objects in the quantum regime. The sections below illustrate a few of the exciting possibilities now within reach.

8.1 Ponderomotive squeezing

Chapter 7 describes the reduction of QRPN by injecting squeezed light produced by an OPO cavity into the optomechanical cavity. An alternative source of squeezed light is the optomechanical cavity itself. Quantum correlations between the optical field and the mechanical motion are produced when quantum radiation pressure is the largest driving force of a resonator. One can use these correlations to suppress, or squeeze, fluctuations in the output optical field below the shot noise level [145, 146]. The squeezed light produced by the quantum correlations is called ponderomotive squeezing [89]. Ponderomotive squeezing has previously been produced by optomechanical cavities [147, 148, 149], but these experiments have only produced squeezing at frequencies above 100 kHz and in a small range of frequencies around the mechanical resonance of their oscillator. For the purposes of using squeezed light in LIGO, we desire the squeezing across a wide range of frequencies in the audio band.

The quantum noise and thermal noise calculated in Chapter 3 can be added in quadrature to give the total noise. When plotting the total noise as a function of frequency or readout quadrature and scaled to shot noise, any regions of the plot that dip below the shot noise level are areas in which ponderomotive squeezing is produced by the optomechanical cavity. The amount and bandwidth of ponderomotive squeezing detected on the photodetector, however, will be reduced by optical losses between the cavity and the photodetector.

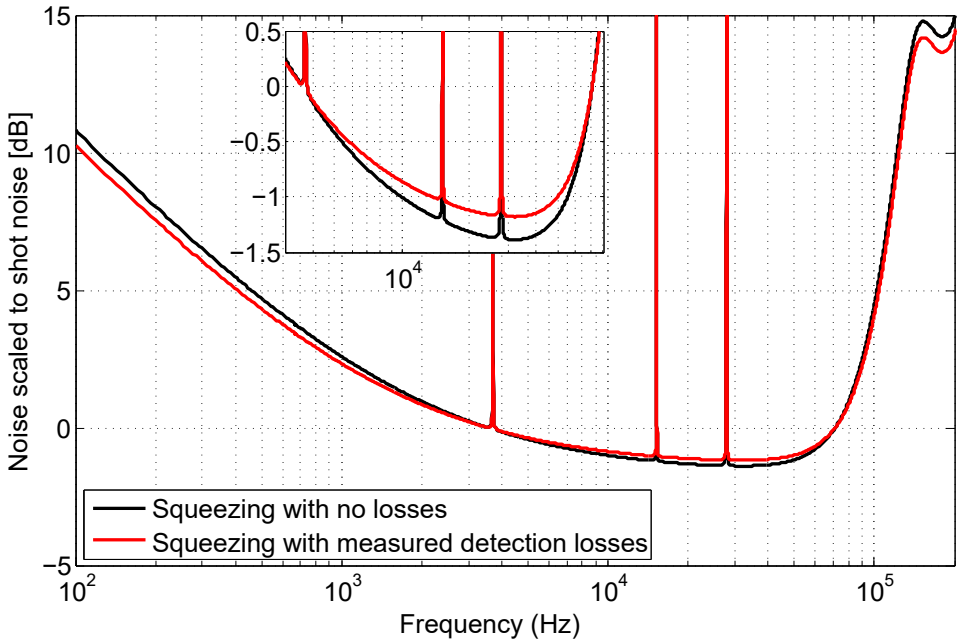

Figure 8.1: Calculation of the ponderomotive squeezing as a function of frequency with a readout angle of $-\pi/3$. The calculation is done with $T1 = 50$ ppm, $T2 = 250$ ppm, intracavity loss $L = 170$ ppm, $\delta_\gamma = 0.57$, and 50 μW of power incident on the movable mirror from the right. The light is detected in reflection of the cantilever mirror and includes measured losses of 13 % between the cavity and the photodetector (including the losses from the photodetector itself).

These losses can be taken into account in the code included in Appendix A by adding a term that represents the optical loss from the optics as well as the quantum efficiency of the photodetector. Figures 8.1 and 8.2 show the predicted amount of ponderomotive squeezing with the experimental parameters and measured noise described in Chapter 6.

As evident from Figures 8.1 and 8.2, the optomechanical cavity described in Chapter 6 is currently producing ponderomotive squeezed light since QRPN is the largest noise source. We have yet to measure any ponderomotive squeezing because the measurement requires a homodyne detector or a device that can sample readout quadratures other than the amplitude quadrature that a single photodetector is sensitive to. We have previously built a phase sensitive readout scheme, shown in Figure 8.3, by combining the light from the optomechanical cavity with a local oscillator (LO) beam at a beamsplitter and measuring the combined beam. The LO beam path contains a mirror attached to a piezo used to

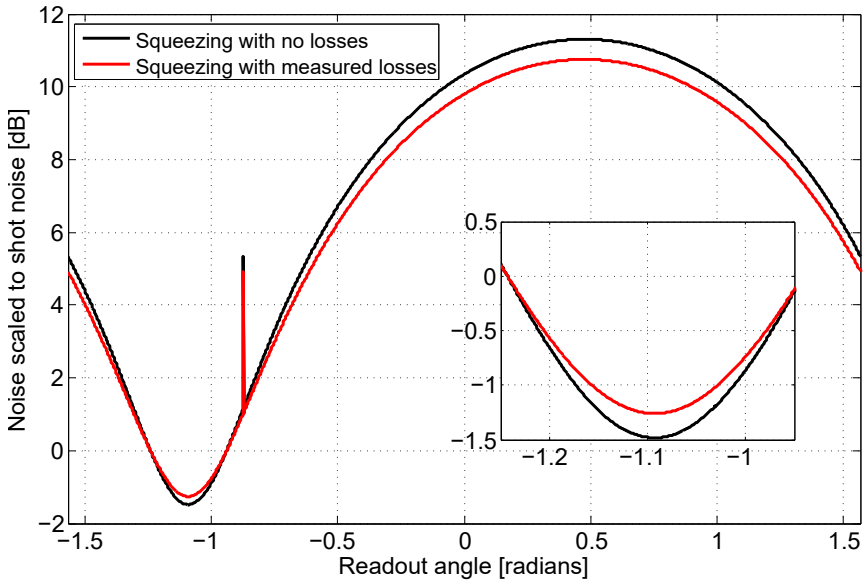

Figure 8.2: Calculation of the ponderomotive squeezing as a function of readout angle at 21 kHz. The calculation is done with $T1 = 50$ ppm, $T2 = 250$ ppm, intracavity loss $L = 170$ ppm, $\delta_\gamma = 0.57$, and 50 μW of power incident on the movable mirror from the right. The light is detected in reflection of the cantilever mirror and includes measured losses of 13 % between the cavity and the photodetector (including the losses from the photodetector itself).

control the phase of the LO in relation to the beam from the cavity. Changing the phase between the two beams allows us to measure different quadratures, and in principle, measure ponderomotive squeezing. Previous measurements with this scheme, however, were limited by excess noise from scattered light in the cavity beam. Noise from scattered light is produced when light from the laser beams scatters off of a reflective surface and later recombines with the main laser beam [150]. When the scattered light beam recombines with the main beam, it adds phase noise to the measurement because it travels a separate optical path from the main beam. This phase noise mimics cavity motion in the measurement and hides the cavity's true motion below it. This effect is magnified for a cavity with a strong optical spring because the optical spring suppresses the cavity's real motion but has no effect on the scattered light. We have since worked to reduce the amount of scattering but have yet to retake any measurements with the LO beam present.

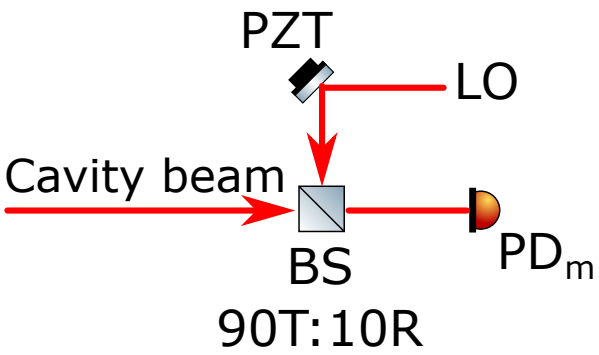

Figure 8.3: Schematic for detecting the ponderomotive squeezing produced by the optomechanical cavity. The beam that is transmitted or reflected by the cavity is interfered on a 90 % transmissive beamsplitter with a coherent field or local oscillator (LO). The phase of the coherent field relative to the cavity field is varied using a piezoelectric transducer (PZT) in the LO path.

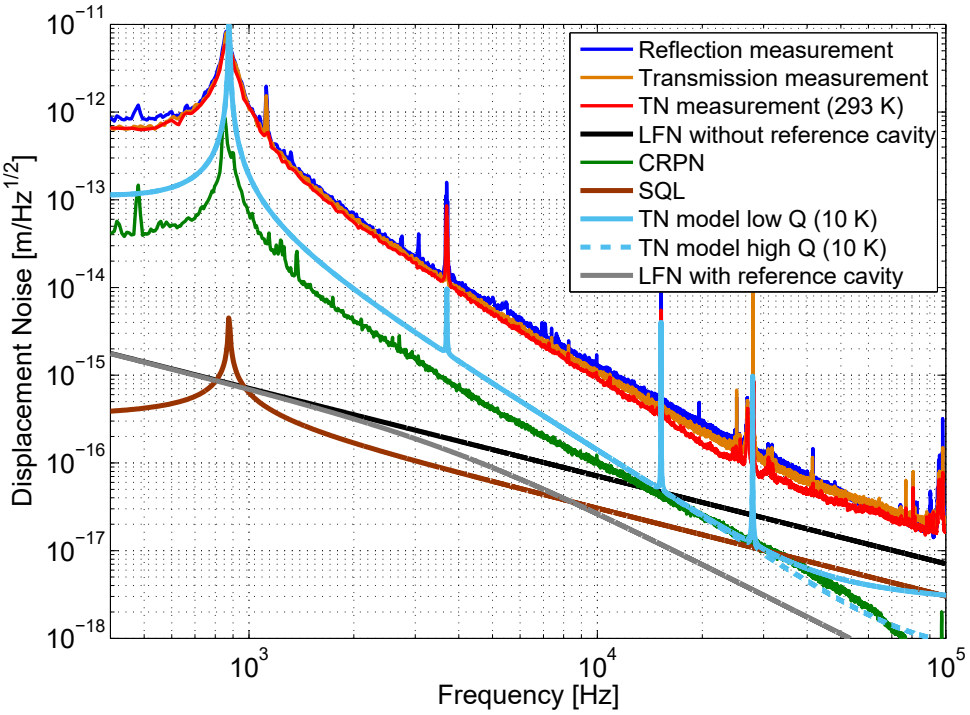

Figure 8.4: Noise budget with the cantilever mirror cooled to 10 K. The current measured displacement noise (green and red curves) is a factor of 4.5 above the SQL (brown curve) at 80 kHz. Two laser frequency noise (LFN) curves are plotted with one assuming the free-running LFN of the laser with no reference cavity (black), and the second including a reference cavity to reduce the LFN (gray). The parameters for the reference cavity are a length of 30 cm, mirror reflectivities of 50 ppm each, and a linewidth (HWHM) of 4 kHz. The three thermal noise curves include a measurement at room temperature (dark blue) and two models at 10 K. One model includes a quality factor of 7,000 for the drumhead mode (solid light blue), while the other uses a quality factor of 100,000 (dashed light blue).

8.2 Standard quantum limit

An exciting prospect for the future of the experiment is the possibility of reaching a sensitivity at or below the standard quantum limit (SQL) [32]. The measured displacement noise spectrum shown in Figure 6.2 is a factor of 4.5 above the SQL between about 80 kHz, as seen in Figure 8.4. As described in Chapter 7, operating the cavity with the light input through the macroscopic mirror and detected in transmission of the cantilever mirror removes the effects of QRPN from the measured spectrum. Below the QRPN, the largest noise source at 80 kHz is the thermal noise. The cantilever mirrors are currently connected to a cryostat as described in Section 3.6 and Figure 3.16 and have previously been cooled to 9 K. Reducing the temperature of the cantilever mirrors from room temperature to 9 K will reduce the thermal noise of the mirrors by a factor of $\sqrt{\frac{293}{9}} = 5.7$, which is below the SQL. In addition to the decrease in noise from cooling the mirrors, we expect a further reduction in the thermal noise around 80 kHz due to the increase in the quality factor of the drumhead mode at low temperatures. At room temperature, the drumhead mode has a Q of about 3,000, which creates the leveling off of the thermal noise above 30 kHz. An increase in the quality factor of the drumhead mode will allow the thermal noise to continue to decrease above 30 kHz. Previous generations of cantilever mirrors have had measured quality factors of up to 200,000. Figure 8.4 shows the modeled thermal noise at 10 K with the quality factor of the drumhead mode equal to 7,000 (low Q curve) and 100,000 (high Q curve). In the near future, we plan to build a reference cavity to reduce the laser frequency noise above 10 kHz. The in-vacuum reference cavity will have an approximate length of 30 cm and will be composed of two mirrors with transmissivities of 50 ppm each. These parameters will produce a cavity with a linewidth (HWHM) of 4 kHz. The reference cavity will act as a low pass filter and will suppress laser frequency noise above the cavity linewidth to below the level of the SQL. The remaining noise source above the SQL, shot noise, will be reduced by detecting the light in transmission of the cavity through the cantilever mirror as opposed to in reflection of the cavity. The shot noise level in Figure 6.2 contains excess

noise from the light that is directly reflected by the cantilever mirror without entering the cavity. This light and excess noise will be eliminated by detecting the light in transmission rather than reflection. In addition, the optical spring can be used to shape the quantum noise sensitivity [91] and create a dip at a desired frequency to surpass the SQL.

8.3 Conclusion

The era of gravitational wave astronomy is here! The first detections of gravitational waves from binary black holes and binary neutron stars has opened a new window to the universe. The continued improvement of Advanced LIGO's sensitivity will provide the opportunity for continued detections and new, exciting results in future observation runs. Despite their vast size, the Advanced LIGO detectors will soon be limited by quantum fluctuations across the majority of its frequency band.

In this thesis, we have investigated the quantum back-action noise that will soon limit Advanced LIGO. For the first time, we have observed quantum radiation pressure noise at frequencies within the gravitational wave detection band. Having done so, we have also shown that quantum radiation pressure noise can be reduced by using squeezed light and that it can be avoided by measuring in the appropriate quadrature. The quantum radiation pressure dominated system that we have constructed provides a platform to test further quantum noise reduction schemes and a way to study the quantum mechanics of macroscopic objects.

References

[1] A. Einstein, Preussische Akademie der Wissenschaften, Sitzungsberichte pp. 844–847 (1915).

[2] F. W. Dyson and A. S. Eddington, Philosophical Transactions of the Royal Society of London A: Mathematical, Physical and Engineering Sciences **220**, 291 (1920).

[3] A. Einstein, Preussische Akademie der Wissenschaften, Sitzungsberichte pp. 688–696 (1916).

[4] J. Taylor and J. Weisberg, Astrophys. J. **253:2** (1982).

[5] B. P. A. an others (LIGO Scientific Collaboration and Virgo Collaboration), Phys. Rev. Lett. **116**, 061102 (2016).

[6] P. R. Saulson, *Fundamentals of Interferometric Gravitational Wave Detectors* (World Scientific, 2017), 2nd ed.

[7] W. R. Johnston, *Illustration of effect of gravitational waves on test masses* (2005), URL `http://www.johnstonsarchive.net/relativity/pictures.html`.

[8] K. Riles, Progress in Particle and Nuclear Physics **68**, 1 (2013).

[9] J. Weber, Phys. Rev. Lett. **18**, 498 (1967).

[10] J. A. et al., Classical and Quantum Gravity **32**, 074001 (2015).

[11] R. Weiss, Quarterly Progress Report, Research Laboratory of Electronics, MIT **105**, 54 (1972).

[12] A. Abramovici et al., Science **256**, 325 (1992).

[13] B. P. Abbott et al., Rep. Prog. Phys. **72**, 076901 (2009).

[14] T. Accadia et al., Journal of Instrumentation **7**, P03012 (2012).

[15] B. Willke et al., Classical and Quantum Gravity **19**, 1377 (2002).

[16] J. Aasi et al. (LIGO Scientific Collaboration and Virgo Collaboration), Phys. Rev. D **89**, 122003 (2014).

[17] J. Aasi et al. (LIGO Scientific Collaboration), Classical and Quantum Gravity **32**, 074001 (2015).

[18] F. Acernese et al. (Virgo Collaboration), Classical and Quantum Gravity **32**, 024001 (2015).

[19] LIGO Lab/Caltech/MIT, *LIGO Livingston Observatory* (2018), URL `https://www.ligo.org/multimedia/gallery/llo.php`.

[20] A. Siegman, *Lasers* (University Science Books, 1986), 1st ed.

[21] H. Bachor and T. Ralph, *A Guide to Experiments in Quantum Optics* (Wiley-VCH, 2004), 2nd ed.

[22] S. Dwyer, Ph.D. thesis, Massachusetts Institute of Technology (2013).

[23] G. Gonzlez, Classical and Quantum Gravity **17**, 4409 (2000).

[24] R. X. Adhikari, Rev. Mod. Phys. **86**, 121 (2014).

[25] G. M. Harry, A. M. Gretarsson, P. R. Saulson, S. E. Kittelberger, S. D. Penn, W. J. Startin, S. Rowan, M. M. Fejer, D. R. M. Crooks, G. Cagnoli, et al., Classical and Quantum Gravity **19**, 897 (2002).

[26] C. Gerry and P. Knight, *Introductory Quantum Optics* (Cambridge University Press, 2005).

[27] C. M. Caves, Phys. Rev. D **23**, 1693 (1981).

[28] C. M. Caves, Phys. Rev. Lett. **45**, 75 (1980).

[29] R. E. Slusher, L. W. Hollberg, B. Yurke, J. C. Mertz, and J. F. Valley, Phys. Rev. Lett. **55**, 2409 (1985).

[30] L.-A. Wu, H. J. Kimble, J. L. Hall, and H. Wu, Phys. Rev. Lett. **57**, 2520 (1986).

[31] H. Vahlbruch, M. Mehmet, K. Danzmann, and R. Schnabel, Phys. Rev. Lett. **117**, 110801 (2016).

[32] V. B. Braginsky, Sov. J. Exp. Theor. Phys. **26**, 831 (1968).

[33] J. Abadie et al. (LIGO Scientific Collaboration), Nat. Phys. **7**, 962 (2011).

[34] H. Grote, K. Danzmann, K. L. Dooley, R. Schnabel, J. Slutsky, and H. Vahlbruch, Phys. Rev. Lett. **110**, 181101 (2013).

[35] J. Aasi et al. (LIGO Scientific Collaboration), Nature Photonics **7**, 613619 (2013).

[36] B. P. Abbott et al. (LIGO Scientific Collaboration and Virgo Collaboration), Phys. Rev. Lett. **116**, 241103 (2016).

[37] B. P. Abbott et al. (LIGO Scientific Collaboration and Virgo Collaboration), Phys. Rev. Lett. **118**, 221101 (2017).

[38] B. P. Abbott et al. (LIGO Scientific Collaboration and Virgo Collaboration), Phys. Rev. Lett. **119**, 141101 (2017).

[39] LIGO Lab/Caltech/MIT, *ligo20170927d* (2018), URL `https://www.ligo.caltech.edu/image/ligo20170927d`.

[40] B. Farr, *GW170817 signal* (2018), URL `http://www.gw.iucaa.in/news/gw170817/`.

[41] F. Elavsky, *BH and NS Mass Chart* (2017), URL `https://www.ligo.caltech.edu/image/ligo20171016a`.

[42] B. P. Abbott et al. (LIGO Scientific Collaboration and Virgo Collaboration), Phys. Rev. Lett. **119**, 161101 (2017).

[43] B. P. Abbott et al. (LIGO Scientific Collaboration and Virgo Collaboration), ApJL **848**, L12 (2017).

[44] T. Corbitt, Ph.D. thesis, Massachusetts Institute of Technology (2008).

[45] D. Kelley, J. Lough, F. Mangaña Sandoval, A. Perreca, and S. W. Ballmer, Phys. Rev. D **92**, 062003 (2015).

[46] R. Singh, G. D. Cole, J. Cripe, and T. Corbitt, Phys. Rev. Lett. **117**, 213604 (2016).

[47] J. Cripe, N. Aggarwal, R. Singh, R. Lanza, A. Libson, M. J. Yap, G. D. Cole, D. E. McClelland, N. Mavalvala, and T. Corbitt, Phys. Rev. A **97**, 013827 (2018).

[48] P. A. Altin, T. T.-H. Nguyen, B. J. J. Slagmolen, R. L. Ward, D. A. Shaddock, and D. E. McClelland, Scientific Reports **7**, 14546 (2017).

[49] V. B. Braginsky, Y. I. Vorontsov, and K. S. Thorne, Science **209**, 547 (1980).

[50] V. B. Braginsky, M. L. Gorodetsky, F. Y. Khalili, and K. S. Thorne, Phys. Rev. D **61**, 044002 (2000).

[51] H. J. Kimble, Y. Levin, A. B. Matsko, K. S. Thorne, and S. P. Vyatchanin, Phys. Rev. D **65**, 022002 (2001).

[52] J. Harms, Y. Chen, S. Chelkowski, A. Franzen, H. Vahlbruch, K. Danzmann, and R. Schnabel, Phys. Rev. D **68**, 042001 (2003).

[53] E. Oelker, T. Isogai, J. Miller, M. Tse, L. Barsotti, N. Mavalvala, and M. Evans, Phys. Rev. Lett. **116**, 041102 (2016).

[54] P. R. Saulson, Phys. Rev. D **42**, 2437 (1990).

[55] T. P. Purdy, R. W. Peterson, and C. A. Regal, Science **339**, 801 (2013).

[56] J. D. Teufel, F. Lecocq, and R. W. Simmonds, Phys. Rev. Lett. **116**, 013602 (2016).

[57] T. P. Purdy, K. E. Grutter, K. Srinivasan, and J. M. Taylor, Science **356**, 1265 (2017).

[58] V. Sudhir, R. Schilling, S. A. Fedorov, H. Schütz, D. J. Wilson, and T. J. Kippenberg, Phys. Rev. X **7**, 031055 (2017).

[59] H. B. Callen and T. A. Welton, Phys. Rev. **83**, 34 (1951).

[60] T. T.-H. Nguyen, C. M. Mow-Lowry, B. J. J. Slagmolen, J. Miller, A. J. Mullavey, S. Goßler, P. A. Altin, D. A. Shaddock, and D. E. McClelland, Phys. Rev. D **92**, 112004 (2015).

[61] R. Lifshitz and M. L. Roukes, Phys. Rev. B **61**, 5600 (2000).

[62] T. Corbitt, Y. Chen, and N. Mavalvala, Phys. Rev. A **72**, 013818 (2005).

[63] T. Corbitt, Y. Chen, F. Khalili, D. Ottaway, S. Vyatchanin, S. Whitcomb, and N. Mavalvala, Phys. Rev. A **73**, 023801 (2006).

[64] C. M. Caves and B. L. Schumaker, Phys. Rev. A **31**, 3068 (1985).

[65] B. L. Schumaker and C. M. Caves, Phys. Rev. A **31**, 3093 (1985).

[66] G. D. Cole, S. Gröblacher, K. Gugler, S. Gigan, and M. Aspelmeyer, Applied Physics Letters **92**, 261108 (pages 3) (2008).

[67] G. D. Cole, W. Zhang, M. J. Martin, J. Ye, and M. Aspelmeyer, Nat Photon **7**, 644 (2013).

[68] G. D. Cole, W. Zhang, B. J. Bjork, D. Follman, P. Heu, C. Deutsch, L. Sonderhouse, J. Robinson, C. Franz, A. Alexandrovski, et al., Optica **3**, 647 (2016).

[69] G. D. Cole, in *Proc. SPIE 8458, Optics & Photonics, Optical Trapping and Optical Micromanipulation IX* (SPIE, 2012), p. 845807.

[70] G. D. Cole, E. Behymer, T. C. Bond, and L. L. Goddard, Opt. Express **16**, 16093 (2008).

[71] G. D. Cole, E. S. Bjorlin, Q. Chen, C.-Y. Chan, S. Wu, C. S. Wang, N. C. MacDonald, and J. E. Bowers, IEEE Journal of Quantum Electronics **41**, 390 (2005).

[72] S. Groblacher, J. B. Hertzberg, M. R. Vanner, G. D. Cole, S. Gigan, K. C. Schwab, and M. Aspelmeyer, Nat Phys **5**, 485 (2009).

[73] F. Sugihwo, M. C. Larson, and J. S. Harris, Applied Physics Letters **72**, 10 (1998).

[74] T. Chalermsongsak, E. D. Hall, G. D. Cole, D. Follman, F. Seifert, K. Arai, E. K. Gustafson, J. R. Smith, M. Aspelmeyer, and R. X. Adhikari, Metrologia **53**, 860 (2016).

[75] Ioffe Institute, *Gallium Arsenide (GaAs): Basic Properties*, URL `http://www.ioffe.ru/SVA/NSM/Semicond/GaAs/basic.html`.

[76] Ioffe Institute, *Gallium Arsenide (GaAs): Thermal Properties*, URL `http://www.ioffe.ru/SVA/NSM/Semicond/GaAs/thermal.html`.

[77] Ioffe Institute, *Aluminum Gallium Arsenide (AlGaAs): Basic Properties*, URL `http://www.ioffe.ru/SVA/NSM/Semicond/AlGaAs/basic.html`.

[78] Ioffe Institute, *Aluminum Gallium Arsenide (AlGaAs): Thermal Properties*, URL http://www.ioffe.ru/SVA/NSM/Semicond/AlGaAs/thermal.html.

[79] Autodesk Inc., *Autodesk Inventor* (2016), URL https://www.autodesk.com/products/inventor/overview.

[80] Copper Development Association, *Oxygen-free high conductivity copper - cu-of, cu-ofe* (2018), URL http://copperalliance.org.uk/copper-and-its-alloys/alloys/copper-conductivity-materials-database/oxygen-free-high-conductivity-copper.

[81] S. R. Domen, International Journal of Radiation Applications and Instrumentation. Part C. Radiation Physics and Chemistry **37**, 199 (1991).

[82] Newport Corporation, *Piezo motor driven linear stage, 12 mm travel*, URL https://www.newport.com/p/AG-LS25.

[83] Newport Corporation, *Piezo driven mount, 1 in., limit switches, vacuum compatible*, URL https://www.newport.com/p/AG-M100LV6.

[84] NIST Material Measurement Laboratory Cryogenic Technologies Group, *Material properties: G-10 CR (fiberglass epoxy)*, http://cryogenics.nist.gov/MPropsMAY/G-10%20CR%20Fiberglass%20Epoxy/G10CRFiberglassEpoxy_rev.htm.

[85] P. R. Saulson, Review of Scientific Instruments **55**, 1315 (1984).

[86] Lumen Learning, *Eddy currents and magnetic damping* (2018), URL https://courses.lumenlearning.com/suny-physics/chapter/23-4-eddy-currents-and-magnetic-damping/.

[87] M. Aspelmeyer, T. J. Kippenberg, and F. Marquardt, Rev. Mod. Phys. **86**, 1391 (2014).

[88] V. B. Braginsky and I. I. Minakova, Moscow Univ. Phys. Bull. **1**, 83 (1964).

[89] V. B. Braginsky and A. B. Manukin, Soviet Physics JETP **25**, 653 (1967).

[90] V. Braginsky, M. Gorodetsky, and F. Khalili, Physics Letters A **232**, 340 (1997).

[91] A. Buonanno and Y. Chen, Classical and Quantum Gravity **19**, 1569 (2002).

[92] B. S. Sheard, M. B. Gray, C. M. Mow-Lowry, D. E. McClelland, and S. E. Whitcomb, Phys. Rev. A **69**, 051801 (2004).

[93] T. Corbitt, D. Ottaway, E. Innerhofer, J. Pelc, and N. Mavalvala, Phys. Rev. A **74**, 021802 (2006).

[94] T. J. Kippenberg, H. Rokhsari, T. Carmon, A. Scherer, and K. J. Vahala, Phys. Rev. Lett. **95**, 033901 (2005).

[95] T. Corbitt, Y. Chen, E. Innerhofer, H. Müller-Ebhardt, D. Ottaway, H. Rehbein, D. Sigg, S. Whitcomb, C. Wipf, and N. Mavalvala, Phys. Rev. Lett. **98**, 150802 (2007).

[96] A. Sawadsky, H. Kaufer, R. M. Nia, S. P. Tarabrin, F. Y. Khalili, K. Hammerer, and R. Schnabel, Phys. Rev. Lett. **114**, 043601 (2015).

[97] M. Hossein-Zadeh and K. J. Vahala, Opt. Lett. **32**, 1611 (2007).

[98] M. P. Edgar, J. Macarthur, B. W. Barr, S. Hild, S. Huttner, B. Sorazu, and K. A. Strain, Classical and Quantum Gravity **33**, 075007 (2016).

[99] N. A. Gordon, B. W. Barr, A. Bell, C. Graef, S. Hild, S. H. Huttner, S. S. Leavey, J. Macarthur, B. Sorazu, J. Wright, et al., Classical and Quantum Gravity **34**, 035020 (2017).

[100] C. H. Metzger and K. Karrai, Nature **432**, 1002 (2004).

[101] A. Naik, O. Buu, M. D. LaHaye, A. D. Armour, A. A. Clerk, M. P. Blencowe, and K. C. Schwab, Nature **443**, 193 (2006).

[102] S. Gigan, H. R. Bohm, M. Paternostro, F. Blaser, G. Langer, J. B. Hertzberg, K. C. Schwab, D. Bauerle, M. Aspelmeyer, and A. Zeilinger, Nature **444**, 67 (2006).

[103] D. Kleckner and D. Bouwmeester, Nature **444**, 75 (2006).

[104] O. Arcizet, P.-F. Cohadon, T. Briant, M. Pinard, and A. Heidmann, Nature **444**, 71 (2006).

[105] A. Schliesser, P. Del'Haye, N. Nooshi, K. J. Vahala, and T. J. Kippenberg, Phys. Rev. Lett. **97**, 243905 (2006).

[106] S. Mancini, D. Vitali, and P. Tombesi, Phys. Rev. Lett. **80**, 688 (1998).

[107] T. Corbitt, C. Wipf, T. Bodiya, D. Ottaway, D. Sigg, N. Smith, S. Whitcomb, and N. Mavalvala, Phys. Rev. Lett. **99**, 160801 (2007).

[108] C. M. Mow-Lowry, A. J. Mullavey, S. Goßler, M. B. Gray, and D. E. McClelland, Phys. Rev. Lett. **100**, 010801 (2008).

[109] B. J. Meers, Phys. Rev. D **38**, 2317 (1988).

[110] G. Heinzel, K. A. Strain, J. Mizuno, K. D. Skeldon, B. Willke, W. Winkler, R. Schilling, A. Rüdiger, and K. Danzmann, Phys. Rev. Lett. **81**, 5493 (1998).

[111] A. Buonanno and Y. Chen, Phys. Rev. D **65**, 042001 (2002).

[112] P. Verlot, A. Tavernarakis, T. Briant, P.-F. Cohadon, and A. Heidmann, Phys. Rev. Lett. **104**, 133602 (2010).

[113] J. Mizuno, K. Strain, P. Nelson, J. Chen, R. Schilling, A. Rdiger, W. Winkler, and K. Danzmann, Physics Letters A **175**, 273 (1993).

[114] G. Heinzel, J. Mizuno, R. Schilling, W. Winkler, A. Rdiger, and K. Danzmann, Physics Letters A **217**, 305 (1996).

[115] B. J. Meers, A. Krolak, and J. A. Lobo, Phys. Rev. D **47**, 2184 (1993).

[116] D. A. Simakov, Phys. Rev. D **90**, 102003 (2014).

[117] C. Affeldt, K. Danzmann, K. L. Dooley, H. Grote, M. Hewitson, S. Hild, J. Hough, J. Leong, H. Lck, M. Prijatelj, et al., Classical and Quantum Gravity **31**, 224002 (2014).

[118] F. A. et al., Classical and Quantum Gravity **32**, 024001 (2015).

[119] K. Somiya, Classical and Quantum Gravity **29**, 124007 (2012).

[120] O. Miyakawa, R. Ward, R. Adhikari, M. Evans, B. Abbott, R. Bork, D. Busby, J. Heefner, A. Ivanov, M. Smith, et al., Phys. Rev. D **74**, 022001 (2006).

[121] N. Aggarwal and N. Mavalvala, A control systems approach to cavity optomechanics, in preparation.

[122] W. Yam, E. Davis, S. Ackley, M. Evans, and N. Mavalvala, Opt. Lett. **40**, 3675 (2015).

[123] J. Cripe, B. Danz, B. Lane, M. C. Lorio, J. Falcone, G. D. Cole, and T. Corbitt, Opt. Lett. **43**, 2193 (2018).

[124] J. D. Thompson, B. M. Zwickl, A. M. Jayich, F. Marquardt, S. M. Girvin, and J. G. E. Harris, Nature **452**, 72 (2008).

[125] A. M. Jayich, J. C. Sankey, B. M. Zwickl, C. Yang, J. D. Thompson, S. M. Girvin, A. A. Clerk, F. Marquardt, and J. G. E. Harris, New Journal of Physics **10**, 095008 (2008).

[126] A. Xuereb, R. Schnabel, and K. Hammerer, Phys. Rev. Lett. **107**, 213604 (2011).

[127] S. L. Danilishin and F. Y. Khalili, Living Reviews in Relativity **15**, 5 (2012).

[128] T. Corbitt, Y. Chen, and N. Mavalvala, Phys. Rev. A **72**, 013818 (2005).

[129] H. Miao, Y. Ma, C. Zhao, and Y. Chen, Phys. Rev. Lett. **115**, 211104 (2015).

[130] C. Grf *et al.*, Class. Quantum Grav. **31**, 215009 (2014).

[131] J. Cripe, N. Aggarwal, B. Lanza, A. Libson, R. Singh, P. Heu, D. Follman, G. D. Cole, N. Mavalvala, and T. Corbitt (2018), URL `https://arxiv.org/abs/1802.10069`.

[132] V. B. Braginsky and A. B. Manukin, *Measurement of Weak Forces in Physics Experiments* (University of Chicago Press, 1977).

[133] C. M. Caves, Phys. Rev. D **23**, 1693 (1981).

[134] H. Nyquist, Phys. Rev. **32**, 110 (1928).

[135] V. Braginsky, M. Gorodetsky, and S. Vyatchanin, Physics Letters A **264**, 1 (1999).

[136] B. Willke, S. Brozek, K. Danzmann, V. Quetschke, and S. Gossler, Opt. Lett. **25**, 1019 (2000).

[137] Y. Chen (2012), Back-action evasion for a trapped mirror, unpublished note from Macrosopic Quantum Mechanics discussion.

[138] H. Miao, H. Yang, R. X. Adhikari, and Y. Chen, Class. Quantum Grav. **31**, 165010 (2014).

[139] M. Evans, L. Barsotti, P. Kwee, J. Harms, and H. Miao, Phys. Rev. D **88**, 022002 (2013).

[140] J. B. Clark, F. Lecocq, R. W. Simmonds, J. Aumentado, and J. D. Teufel, Nature Physics **12** (2016).

[141] K. McKenzie, N. Grosse, W. P. Bowen, S. E. Whitcomb, M. B. Gray, D. E. McClelland, and P. K. Lam, Phys. Rev. Lett. **93**, 161105 (2004).

[142] R. W. P. Drever, J. L. Hall, F. V. Kowalski, J. Hough, G. M. Ford, A. J. Munley, and H. Ward, Applied Physics B **31**, 97 (1983), ISSN 1432-0649.

[143] M. J. Yap, *Sledgehammer/ beamsplitter approach* (2016), URL `https://dcc.ligo.org/LIGO-G1602264`.

[144] K. Goda, O. Miyakawa, E. E. Mikhailov, S. Saraf, R. Adhikari, K. McKenzie, R. Ward, S. Vass, A. J. Weinstein, and N. Mavalvala, Nature Physics **4**, 472 (2008).

[145] C. Fabre, M. Pinard, S. Bourzeix, A. Heidmann, E. Giacobino, and S. Reynaud, Phys. Rev. A **49**, 1337 (1994).

[146] S. Mancini and P. Tombesi, Phys. Rev. A **49**, 4055 (1994).

[147] D. W. C. Brooks, T. Botter, S. Schreppler, T. P. Purdy, N. Brahms, and D. M. Stamper-Kurn, Nature **488**, 476 (2012).

[148] A. H. Safavi-Naeini, S. Gröblacher, J. T. Hill, J. Chan, M. Aspelmeyer, and O. Painter, Nature **500**, 185 (2013).

[149] T. P. Purdy, P.-L. Yu, R. W. Peterson, N. S. Kampel, and C. A. Regal, Phys. Rev. X **3**, 031012 (2013).

[150] J. Vinet, V. Brisson, and S. Braccini, Phys. Rev. D **54**, 1276 (1996).

Appendix A
Matlab Code for Calculating Thermal Noise and Quantum Noise

A.1 Thermal noise code

The code described in this section calculates the structural and viscous thermal noise of the cantilever mirror. The inputs to the code are the mechanical frequencies and modal masses of the cantilever mirror's mechanical resonances. These are calculates separately in a finite element model. The other inputs to this code are the temperature of the cantilever mirrors and the quality factors (Qs) of the mechanical resonances. The inputs are identified in single quotation marks. The output of the code is the thermal noise spectrum in units of $^{m}/\sqrt{Hz}$.

```
% Define a frequency space for the calculations. Here we use 3400
    points between 100 Hz and 3 MHz. Increasing the number of
    points will increase the frequency resolution but increase the
    computation time.
f = logspace(2,log10(3000000),3400);

% Read in the COMSOL text file containing the information about
    the resonant frequecies and coupling strengths of the j
    mechanical modes.
A = importdata('COMSOL output file.txt');

% Calculate the modal mass for each of the j mechanical modes.
% The 2e-4 factor is a normalization constant from the COMSOL
    model, and 'Density' density of the cantilever mirror
    material in units of kg/m^3
MT = 2e-4./(A(:,2)).^2*'Density';


% Set the modal mass of the fundamental mode. The units are
    kilograms.
MT(1) = 'Mass';

% Define the temperature of the cantilever mirrors in Kelvin.
Te = 293;

% Define the quality factor for the fundamental mode.
Q0 = 'Fundamental Q';

% Define a matrix for the strcutral thermal noise (TS) and
    viscous thermal noise (TT).
TT = 0;
TS = 0;
```

```
% Calculate the strcutral thermal noise (TS) and viscous thermal
    noise (TT) of the fundamental mode. The functions THN and THv
    are equations 6.1 and 3.4.
TT = sqrt(TT.^2+THv(f,MT(1),A(1,1),Q0,Te).^2);
TS = sqrt(TS.^2+THN(f,MT(1),A(1,1),Q0,Te).^2);

% Define the mechanical susceptibility of the mechanical
    oscillator using Equation 2.19.
S = 1/MT(1)/(2*pi)^2./(f.^2-A(1,1)^2-i*f*A(1,1)/Q0);


% Set the quality factors for the higher order modes that have
    measurements of their Q. The j = 2 mode is the yaw mode, and
    the j = 3 mode is the pitch mode. Then calculate the thermal
    noise contribution for the j higher order mechanical modes.
    The thermal noise from each mode is added in quadrature to
    form the total thermal noise. Also calculate the mechanical
    suseptibility while including the higher order modes.

for j=2:length(MT)
    if A(j,1) > 1e5
        Q = 'Higher order mode Q';
     elseif j==2
        Q = 'Yaw Q'

     elseif j==3
        Q = 'Pitch Q'

    else
        Q = Q0;
    end


      TT = sqrt(TT.^2+THv(f,MT(j),A(j,1),Q,Te).^2);
      TS = sqrt(TS.^2+THN(f,MT(j),A(j,1),Q,Te).^2);

      S = S + 1/MT(j)/(2*pi)^2./(f.^2-A(j,1)^2-i*f*A(j,1)/Q);
end


% Plot the thermal noise spectrum in units of  m/sqrt(Hz)
loglog(f,TT,'r',f,TS,'b')
```

This ends the thermal noise section of the code. We have calculated the viscous thermal

noise (TT) and structural thermal noise (TS).

A.2 Quantum noise code

This code consists of the input-output relations described in Section 3.3. This code can be run in conjuction with the thermal noise code decribed above.

```
% Define the input, output, and intracavity fields.

%        M1              M2
% a --> ||  c --> e --> ||  g -->
% b <-- ||  d <-- f <-- ||  h <--

% r = b at 0 phase (ie rotate so that r1 is amplitude, r2 is
    phase)
% t = g at 0 phase

% Define the laser wavelength and frequency and the lenth of the
    cavity.

hbar=1e-34; % Reduced Planck's constant
lambda = 1064e-9; % Laser wavelength in meters
L = 0.01; % Cavity length in meters
c=3e8; % Speed of light in meters per second
w0 = 2*pi*c/lambda; % Laser frequency

% Define the mirror reflectivities and transmissivities and
    losses and the input laser power.
Loss = 'Intracavity loss';
T1 = 'T1';
R1 = 1-T1;
T2 = 'T2';
R2 = 1-T2-Loss;
Pin = 'Input power'; % Laser power in W

% Define photodetector quantum efficiency. Optical losses in the
    readout path can also be added here.
DetEff = 'Detection efficiency';

% Define the cavity detuning in linewidths and phase
dL = 'Detuning'; % Detuning in linewidths
dL = dL*lambda*(T1+T2+Loss)/8/pi; % Detuning in linewidths

% Define frequency space and angle space (for varying the readout
     quadrature)
f = logspace(2,log10(3000000),3400);
```

```
angles = linspace(-pi/2,pi/2,3400);

% Define the standard quantum limit (SQL)
xsql = sqrt(2*hbar.*abs(S));

% Solve for DC carrier fields as in Equation 3.9
M0 = zeros(8); % M0 * (a-h) = inputs, a=1, b=2, etc

for z = 1:8
    M0(z,z) = -1;
end;



M0(2,1) = sqrt(R1); % b = rho1 * a + tau1*d
M0(2,4) = sqrt(T1);

M0(3,1) = sqrt(T1); % c = tau1 * a - rho1*d
M0(3,4) = -sqrt(R1);

M0(4,6) = exp(i*w0*dL/c); % d gets phase shift from length

M0(5,3) = exp(i*w0*dL/c); % e gets phase shift from length

M0(6,5) = -sqrt(R2); % f = -rho2*e + tau2*h
M0(6,8) = sqrt(T2);
M0(7,5) = sqrt(T2); % g = tau2*e + rho2*h
M0(7,8) = sqrt(R2);

M0(8,8) = 1;
iM0 = inv(M0);
P=1:1:8;
for z=1:8
% Comment out one of the below depending on which side of the
   cavity is used as the input.
    P(z) = iM0(z,1)*sqrt(Pin); % Amplitude of carrier when the
       macroscopic mirror is input mirror.
    P(z) = iM0(z,8)*sqrt(Pin); % Amplitude of carrier when
       cantilever is input mirror.
end

% Calculate the circulating power
Pcirc = (abs(P(3)))^2

% Solve for sidebands as in Equation 3.11.
```

```
M = zeros(22); %M0 * (a-h) = inputs * 2 quadratures (amplitude
    and phase)

% Indices for matrix M
a1 = 1;
a2 = 2;
b1 = 3;
b2 = 4;
c1 = 5;
c2 = 6;
d1 = 7;
d2 = 8;
e1 = 9;
e2 = 10;
f1 = 11;
f2 = 12;
g1 = 13;
g2 = 14;
h1 = 15;
h2 = 16;
X = 17; % Small displacement of the moveable mirror
F = 18; % Force on the movable mirror
r1 = 19;
r2 = 20;
t1 = 21;
t2 = 22;

for z = 1:22
    M(z,z) = -1;
end;


% Solve for all the matrix elements.
for z=1:length(f)
% Use this when solving the equations as a fuction of frequnecy
    with a constant readout angle. Comment out if doing a function
     of readout angle.
readout_angle = 0;
% Use this when solving the equations as a function of readout
    angle at a constant frequency. Comment out if doing a function
     of frequency.
for za = 1:length(angles)
readout_angle = angles(za);
z = 1000; % This is the set frequency chosen from f.
```

```
O = -2*pi*f(z); % sideband frequency


M(b1,a1) = sqrt(R1); % b = rho1*a + tau1*d
M(b1,d1) = sqrt(T1);
M(b2,a2) = sqrt(R1);
M(b2,d2) = sqrt(T1);

M(c1,a1) = sqrt(T1); % c = tau1*a - rho1*d
M(c1,d1) = -sqrt(R1);
M(c2,a2) = sqrt(T1);
M(c2,d2) = -sqrt(R1);

% Phase shift and rotation from free space
M(d1,f1) = exp(i*O*L/c)*cos(w0*dL/c);
M(d1,f2) = exp(i*O*L/c)*sin(w0*dL/c)*-1;
M(d2,f1) = exp(i*O*L/c)*sin(w0*dL/c);
M(d2,f2) = exp(i*O*L/c)*cos(w0*dL/c);

M(e1,c1) = exp(i*O*L/c)*cos(w0*dL/c);
M(e1,c2) = exp(i*O*L/c)*sin(w0*dL/c)*-1;
M(e2,c1) = exp(i*O*L/c)*sin(w0*dL/c);
M(e2,c2) = exp(i*O*L/c)*cos(w0*dL/c);

% Coupling of X to reflected field
mag = 2*sqrt(R2)*w0/c/sqrt(hbar*w0)*sqrt(2);


M(f1,X) = mag*imag(P(5));
M(f2,X) = -mag*real(P(5));




M(X,F) = S(z); % Mechanical susceptibility

mag = sqrt(hbar*w0/c^2); % Radiation pressure on end mirror
Pe = P(5);
Pf = P(6);
Pg = P(7);

M(F,e1) = sqrt(2)*real(Pe)*mag;
M(F,e2) = sqrt(2)*imag(Pe)*mag;
M(F,f1) = sqrt(2)*real(Pf)*mag;
```

```
M(F,f2) = sqrt(2)*imag(Pf)*mag;
M(F,g1) = sqrt(2)*real(Pg)*mag;
M(F,g2) = sqrt(2)*imag(Pg)*mag;


M(f1,e1) = -sqrt(R2); % f = tau1*h - rho1*e
M(f1,h1) = sqrt(T2);
M(f2,e2) = -sqrt(R2);
M(f2,h2) = sqrt(T2);

M(g1,e1) = sqrt(T2); % g = rho1*e + tau1*h
M(g1,h1) = sqrt(R2); %
M(g2,e2) = sqrt(T2);
M(g2,h2) = sqrt(R2);


% Derotate r1=amplitude and r2=phase
M(r1,b1) = cos(-phase(P(2)));
M(r1,b2) = -sin(-phase(P(2)));
M(r2,b1) = sin(-phase(P(2)));
M(r2,b2) = cos(-phase(P(2)));


% Derotate t1=amp, t2=phase
M(t1,g1) = cos(-phase(P(7))+readout_angle);
M(t1,g2) = -sin(-phase(P(7))+readout_angle);
M(t2,g1) = sin(-phase(P(7))+readout_angle);
M(t2,g2) = cos(-phase(P(7))+readout_angle);


% Invert the matrix M to solve for the output fields in terms of
    the input fields.
iM = inv(M);


% Some of the useful matrix elements

R_supp(z) = iM(X,F); % Susceptibility
R(z) = iM(t1,h1); % Transfer function for intensity fluctuations
    in reflection of the cavity with the input at h
RR(z) = iM(t1,X); % Transfer function for the displacement of the
     mirror to intensity fluctuations at t
RRzat(z) = iM(t1,X); % Same as above except for a function of
    readout angle
```

```
RRzar(z) = iM(r1,X); % Transfer function for the displacement of
    the mirror to intensity fluctuations at a for function of
    readout angle
RRR(z) = iM(t1,a1); % Transfer function for intensity
    fluctuations in transmission of the cavity with the input at a
RRRr(z) = iM(r1,h1);  % Transfer function for intensity
    fluctuations in transmission of the cavity with the input at h
RRRa2(z) = iM(t1,a2);  % Transfer function from phase
    fluctuations at a to transmitted intensity fluctuations
RRRR(z) = iM(X,X);
RTT(z) = iM(t1,X).*TT(z); % Includes viscous damping thermal
    noise
RTS(z) = iM(t1,X).*TS(z); % Includes structural damping thermal
    noise

%Adding radiation pressure in. Inputs are at a and h. Measuring
    in the t1
%quadrature. If this number = 1, then we have shot noise level.
%For losses at mirror 1, b and c become inputs as well. Scale
    with
%(Loss)/(1 - Loss)
% This can be calculated either as a function of frequency or
    readout angle. Comment or uncomment the appropriate lines
    depending on that choice.
RPN(z) = (abs(iM(t1,a1)))^2 + (abs(iM(t1,a2)))^2 + (abs(iM(t1,h1)
    ))^2 + (abs(iM(t1,h2)))^2 +...
    ((Loss)/(1 - Loss))*(abs(iM(t1,b1)))^2 + ((Loss)/(1 - Loss))*(
        abs(iM(t1,b2)))^2 +...
    ((Loss)/(1 - Loss))*(abs(iM(t1,c1)))^2 + ((Loss)/(1 - Loss))*(
        abs(iM(t1,c2)))^2;


% For function of frequency with a constant readout angle
 TNT(z) = sqrt((abs(RPN(z))) + (abs(RTT(z))).^2); %Total noise:
     Quantum and viscous damping thermal noise
 TNS(z) = sqrt((abs(RPN(z))) + (abs(RTS(z))).^2); %Total noise:
     Quantum and structural damping thermal noise


% Radiation pressure noise for a function of readout angle (za).
% RPN(za) = (abs(iM(t1,a1)))^2 + (abs(iM(t1,a2)))^2 + (abs(iM(t1,
    h1)))^2 + (abs(iM(t1,h2)))^2 +...
 %     ((Loss)/(1 - Loss))*(abs(iM(t1,b1)))^2 + ((Loss)/(1 - Loss)
     )*(abs(iM(t1,b2)))^2 +...
```

```
  %    ((Loss)/(1 - Loss))*(abs(iM(t1,c1)))^2 + ((Loss)/(1 - Loss)
     )*(abs(iM(t1,c2)))^2;


% Quantum noise plus thermal noise for function of readout angle
    with a constant frequency
 %TNT(za) = sqrt((abs(RPN(za))) + (abs(RTT(z))).^2);
 %TNS(za) = sqrt((abs(RPN(za))) + (abs(RTS(z))).^2);




% Make plots for whatever you would like to investigate. A few
    intersting examples are listed below.

loglog(f,1./abs(Rr));  % Shot noise (does not include QRPN)
loglog(f,RPN*1./abs(Rr)); % Quantum noise (shot noise plus QRPN)
loglog(f,TNT.*1./abs(RR),'r-.'); % Plot total noise using quantum
     noise and viscous damping
loglog(f,TNS.*1./abs(RR),'r.'); % Plot total noise using quantum
    noise and structural damping
loglog(f,xsql); % Plot the SQL



% For plotting the ponderomotive squeezing as a function of
    frequency with a constant readout angle
semilogx(f,TNS,'k');

%Adding the photodector quantum efficiency
semilogx(f,sqrt(DetEff)*TNS + sqrt(1-DetEff),'g');

% For plotting the optical spring and the cavity linewidth and
    detuning (only visible if using a sufficiently high frequency
    in the frequency space)
mbode(f,-RRRr/(max(abs(RRRr))),'k');

% Plots as a function of readout angle with a constant frequency

%plot(angles,TNT,'r'); % Total noise using quantum noise and
    viscous damping
%plot(angles,TNS,'b'); % Total noise using quantum noise and
    structural damping
```

Vita

Jonathan D. Cripe, a native of Belleville, Illinois, received his bachelor's degree from DePauw University in 2012. At DePauw University, Jonathan majored in Physics and Mathematics and was a member of the DePauw Cross Country and Track and Field teams and the University Jazz Band. After graduation, Jonathan received a Deutscher Akademischer Austauschdienst scholarship to study and conduct research as a visiting student at the Albert Einstein Institute in Hannover, Germany. Jonathan began his doctoral studies at Louisiana State University in Baton Rouge, Louisiana in 2013. At LSU, Jonathan joined the Laser Interferometer Gravitational Wave Observatory (LIGO) research group and was advised by Dr. Thomas Corbitt. Jonathan's recreational interests range from running and cycling to traveling, music, and enjoying the outdoors.